

DISSERTATION

Geometric Phase Properties in Neutron Optics Experiments

ausgeführt zum Zwecke der Erlangung des akademischen Grades eines
Doktors der technischen Wissenschaften unter der Leitung von

Privatdoz. Dr. Yuji Hasegawa
E 141
Atominstitut der Österreichischen Universitäten

eingereicht an der Technischen Universität Wien
Fakultät für Physik

von

Dipl. Ing. Jürgen Klepp
Matrikelnummer 9525165
Kasernstrasse 33/4, 3500 Krems
Österreich

Wien, am 25. März 2009

Abstract

The concept of geometric phases between quantum states has drawn much attention in the last three decades. Geometric phases depend, in contrast to their dynamic counterparts, only on the evolution path of quantum states in state space. The field was constantly extended and has undergone a series of generalizations: From their discovery for adiabatic and cyclic evolutions to the nonadiabatic, noncyclic and even the mixed-state case for unitary and nonunitary evolutions.

In the present work, special properties of mixed input phases are investigated experimentally with polarized neutrons. The first part describes a measurement of phases for mixed input states undergoing unitary evolutions. Phases of purely dynamical and purely geometric origin are measured as a function of the adjusted input purity of the neutron state. Measuring suitable combinations of both, it was demonstrated that the mixed-state geometric phase is not additive as it is the case for pure states. Nonadditivity is a natural consequence of the definition of the mixed-state phase as weighted average of the phase factors of all pure state components in the density matrix.

In the second part, the phase stability under particular noise influences during the evolution is tested (nonunitary evolutions). For very special and well-defined assumptions, it is confirmed that the nonadiabatic cyclic geometric phase is robust against noise only if the spin evolution path is such that the acquired dynamical phase is zero.

Kurzfassung

Das Konzept der geometrischen Phasen zwischen Quantenzuständen hat in den letzten drei Jahrzehnten viel Aufmerksamkeit auf sich gezogen. Geometrische Phasen sind, im Unterschied zu dynamischen Phasen, nur vom Entwicklungspfad von Quantenzuständen im Zustandsraum abhängig. Das Gebiet wurde ständig erweitert und hat eine Reihe von Verallgemeinerungen erfahren. Heute reicht sein Spektrum von der Entdeckung der geometrischen Phasen für adiabatische, zyklische Entwicklungen über nichtadiabatische, nichtzyklische Entwicklungen bis zum nichtdiagonalen und nichtunitären Fall. In der vorliegenden Arbeit werden einige der speziellen Eigenschaften von geometrischen Phasen mit der Technik der Neutronenpolarimetrie experimentell beleuchtet. Der erste Teil beschreibt eine Phasenmessung mit gemischten Eingangszuständen. Phasen rein dynamischen und rein geometrischen Ursprungs wurden als eine Funktion der Mischung des Eingangszustandes gemessen. Besonderes Augenmerk wird hierbei auf die Verletzung der Additivität der Phasen für gemischte Eingangszustände gelegt und diese bestätigt. Die Nichtadditivität entsteht aus der Definition der Phase als gewichtete Summe der Phasenfaktoren aller Eigenzustände der Dichtematrix. Der zweite Teil befasst sich mit geometrischen Phasen unter nichtunitären Entwicklungen. Es wurde unter bestimmten wohldefinierten Annahmen gezeigt, dass geometrische Phasen von speziellen Störungen nicht beeinflusst werden, wenn in der Zustandsentwicklung kein dynamischer Phasenanteil entsteht.

Contents

1	Introduction	1
2	Observation of Mixed-state Phases	5
2.1	The Pancharatnam Phase	5
2.2	Noncyclic Geometric Phase	8
2.3	Mixed-State Pancharatnam Phase	8
2.4	Pancharatnam Phase in Neutron Polarimetry	11
2.4.1	The Pure State Case	11
2.4.2	The Mixed State Case	16
2.5	Entanglement of Spin and Momentum	18
2.6	Experiment	22
2.6.1	Detectors	22
2.6.2	Time Of Flight measurements - TOF	23
2.6.3	Reducing Second-Order Intensity	27
2.6.4	Nonadiabatic Transitions between Guide Fields	29
2.6.5	DC Coils	31
2.6.6	Adjusting DC Coils	33
2.6.7	How to set Distance with polarized Neutrons	40
2.6.8	Creation of the Mixed State	41
2.6.9	Measuring the Purity	46
2.6.10	Normalization of Intensities	49
2.7	Experimental Results	50
2.7.1	Purity-Dependence of the Phase	50
2.7.2	Nonadditivity	54
2.8	Discussion	56
3	Nonunitary Phases	61
3.1	Theory	61
3.2	An Example	64
3.3	Nonunitary Phases and Neutron Polarimetry	68
3.4	Experiment	74

3.4.1	Measurement and Results	74
3.5	Discussion	83
4	Conclusion and Outlook	87

Chapter 1

Introduction

Although the beginnings of Quantum mechanics can be traced back more than 100 years, its case is far from being closed. With ongoing progress in experimental technologies, big obstacles on the way to understanding the basic principles are removed every day. Leaving aside optimistic hopes for ambitious goals like a quantum computer within the next few years, quantum mechanics is still as fascinating as it was in its early days. Its description and prediction of a wide range of phenomena, that are completely counterintuitive not only to the lay mind, keep attracting us.

Because of the great success of waves as a model for numerous problems in classical physics, the notion of phase is of great importance also in quantum mechanics. A good example is the concept of *geometric phase*. It was discovered by M. V. Berry [Berry 1984] and found to be closely related to the early findings of S. Pancharatnam [Pancharatnam 1956, Berry 1987]. Evolving quantum systems acquire two kinds of phase factors: (*i*) the dynamical phase which depends on the dynamical properties of the system - like energy - during a particular evolution, and (*ii*) the geometric phase which only depends on the path the system takes in state space on its way from the initial to the final state. Numerous related theoretical works as well as experimental demonstrations have been done so far. The concept was widely expanded and has undergone several generalizations (see [Shapere and Wilczek 1989] or [Anandan *et al.* 1997] for an overview). Nonadiabatic [Aharonov and Anandan 1987] and noncyclic [Samuel and Bhandari 1988] evolutions as well as the off-diagonal case, where initial and final state are mutually orthogonal [Manini and Pistolesi 2000], have been considered. Ever since, a great variety of experimental demonstrations has been accomplished [Tomita and Chao 1986, Suter *et al.* 1988] also in neutron optics [Bitter and Dubbers 1987, Wagh *et al.* 1997, Wagh *et al.* 1998, Hasegawa *et al.* 2001, Filipp *et al.* 2005]. Due to its potential robustness against noise [De Chiara and Palma 2003,

Zhu and Zanardi 2005], the geometric phase is an excellent candidate to be utilized for logic gate operations in quantum information technology [Nielsen and Chuang 2000]. Thus, a rigorous investigation of all its properties is of great importance.

In addition to an approach by Uhlmann [Uhlmann 1991] a new concept of phase for mixed input states based on an operational approach was developed [Wagh *et al.* 1998, Sjöqvist *et al.* 2000]. Here, each eigenvector of the initial density matrix independently acquires a phase. The total mixed state phase is a weighted average of the individual phase factors. This concept is of great significance for such experimental situations or technical applications where pure state theories may imply strong idealizations. Theoretical predictions have been tested by Du *et al.* [Du *et al.* 2003] and Ericsson *et al.* [Ericsson *et al.* 2003a] using NMR and single-photon interferometry, respectively.

Within the scope of the first part of this thesis, measurements of nonadiabatic geometric, dynamical and combined phases with polarized neutrons for noncyclic evolutions are described. These phases depend on noise strength in state preparation, providing the degree of polarization – the *purity* – of the neutron input state. In particular, the experiment demonstrates that the geometric and dynamical mixed state phases Φ_g and Φ_d , resulting from separate measurements, are not additive [Sjöqvist 2002, Singh *et al.* 2003]. The phase resulting from a single – cumulative – measurement differs from $\Phi_g + \Phi_d$. This nonadditivity might be of practical importance for possible applications of geometric phases. The results are published in [Klepp *et al.* 2008].

The developments leading to consistent and testable theories for mixed-state quantum phases naturally set off also the next step: A treatment of phases under nonunitary evolutions. The nonunitarity mostly comes into play by interactions of the system with an environment (*open quantum systems*), leading to vanishing off-diagonal elements of the states' density matrix. This process is usually referred to as *decoherence* [Zurek 2002, Joos *et al.* 2003]. A first approach to nonunitary phases for pure states under non-hermitian Hamiltonians was given in [Garrison and Wright 1988]. In [DeChiara and Palma 2003], it was shown that for adiabatic evolutions under classical adiabatic noise, dephasing is mainly due to the fluctuations of the dynamical phase. Furthermore, it was demonstrated there that the variance of the Berry phase is inverse proportional to the evolution time, an aspect which was also confirmed recently in a dedicated experiment with ultra-cold neutrons [Filipp *et al.* 2009]. Closely related to this result is an experiment with superconducting qubits by [Leek *et al.* 2007] that demonstrates the geometric dependence of the variance of the geometric phase under slow noise. Us-

ing a *quantum jump* approach, it was found in [Carollo *et al.* 2003], that the geometric phase is independent of noise. A quantum jump is – within this context – a fluctuation leading to an instantaneous sign inversion of the polar angle enclosed by the Bloch vector and the precession axis. After each jump, the Bloch vector finishes the precession through the azimuthal angle given by the evolution path, so that no change of the total solid angle occurs. In contrast, following the notion of mixed-state Pancharatnam phases in [Sjöqvist *et al.* 2000] and in particular its kinetic version put forward by [Singh *et al.* 2003], [Tong *et al.* 2004] found that only in the special case where the induced phase is of purely geometric origin, it is independent of fluctuations in direction parallel to the precession axis. Their geometric phase is gauge invariant, i. e. only depends on the path traced out in state space. Furthermore, their results reduce to the ones of [Sjöqvist *et al.* 2000] and [Singh *et al.* 2003] in the limit of unitary evolutions. The latter is unclear for the approach of [Peixoto de Faria *et al.* 2003], which employs the concept of completely positive maps. Although operationally well defined, the ideas developed in [Ericsson *et al.* 2003b] yield different values of geometric phases for different Kraus representations. The case in which the system undergoes an adiabatic evolution driven by a slowly varying magnetic field and is weakly coupled to a dissipative environment is studied in [Whitney *et al.* 2005]. Here, the acquired Berry phase suffers a purely geometric modification. The problem is tackled in more general frameworks in [Lombardo and Villar 2006], [Yi *et al.* 2006] and [Zhu and Zanardi 2005], the latter putting much emphasis on the aspect of robustness of the non-adiabatic geometric phase from the point of view of quantum computation. There, maximum phase gate fidelities in the presence of stochastic control errors are found for vanishing dynamical phase.

Motivated by the above developments and a clear lack of experimental work in this field, the second part of this thesis describes neutron polarimeter measurements dedicated to testing the robustness of geometric phases under noisy evolutions. It is shown that the measured shifts of intensity oscillations are independent of the noise level in the experiment, for an evolution with vanishing dynamical phase. The experiment partly follows the proposal given in [Tong *et al.* 2004]. The qualitative demonstration of the robustness of the geometric phase may only be stated to be achieved if some assumptions about the nature of the spin evolution under noise are accepted. A clear and also quantitative experimental proof of the results in [Tong *et al.* 2004], however, is still to be accomplished in the future.

Chapter 2

Observation of Mixed-state Phases

In this chapter, a measurement of mixed-state phases with polarized neutrons is described. First, the theoretical prerequisites are briefly explained. Second, a detailed description of the experimental setup and its adjustment is given. Subsequent, measurement and data analysis are explained and the results are shown. The chapter closes with a discussion of these results, open questions and some ideas concerning potential applications of mixed-state phases.

2.1 The Pancharatnam Phase

In 1984, Berry explicitly calculated the phase accumulated by a quantum state under adiabatic and cyclic evolutions [Berry 1984]. Besides the usual dynamical phase, he found an additional geometric contribution of minus half the solid angle Ω enclosed by the evolution path, as seen from the point of degeneracy in parameter space, which is the origin of the so-called Poincaré (for photon polarization states) or Bloch sphere (for other two-level quantum systems). As an example consider polarized neutrons within a magnetic field whose direction (the parameter) is changed adiabatically – slow enough for the system to remain in an eigenstate of the instantaneous Hamiltonian at all times of the evolution. Following [Sjöqvist 2002], Pancharatnam's phase is explained and its connection to the noncyclic and nonadiabatic geometric phase is established in the next Sections.

We consider two nonorthogonal state vectors $|A\rangle$ and $|B\rangle$. What is the phase between the two? If they are collinear, so $|A\rangle = e^{i\phi}|B\rangle$, the answer is ϕ . If not, the answer is not trivial. Pancharatnam stated that one could set up some experiment in which $|A\rangle$ and $|B\rangle$ are interfering. The intensity is

measured as:

$$\begin{aligned}
I &= |e^{i\chi}|A\rangle + |B\rangle|^2 \\
&= 2 + \langle B|A\rangle e^{i\chi} + (\langle B|A\rangle e^{i\chi})^* \\
&= 2 + 2\text{Re}(\langle B|A\rangle e^{i\chi}) \\
&= 2 + 2|\langle A|B\rangle| \cos(\chi - \arg\langle A|B\rangle), \tag{2.1}
\end{aligned}$$

where we have used that, in general, $\langle B|A\rangle$ is a complex number. The important point is that the oscillations, obtained by varying χ for $|A\rangle = |B\rangle$ are shifted if we change either $|A\rangle$ or $|B\rangle$ so that $|A\rangle \neq |B\rangle$. This is the Pancharatnam relative phase shift between $|A\rangle$ and $|B\rangle$. Equation (2.1) is at maximum when $\chi = \arg\langle A|B\rangle$ or, for fixed $\chi = 0$ and varied $\arg\langle A|B\rangle$, when the Pancharatnam phase $\phi \equiv \arg\langle A|B\rangle = 0$. Then the two states are considered to be "in-phase". This is the case if $\langle A|B\rangle$ is real and positive, which is called *Pancharatnam's connection*. For example, the states $|A\rangle = |+\rangle$ and $|B\rangle = 1/\sqrt{2}(|+\rangle - i|-\rangle)$ are in-phase states. An important property of this phase is found when projecting two in-phase states $|A\rangle, |B\rangle$ on a third state $|C\rangle$:

$$\begin{aligned}
|C'\rangle &= |C\rangle\langle C|A\rangle \\
|C''\rangle &= |C\rangle\langle C|B\rangle.
\end{aligned}$$

The relative phase between $|C'\rangle$ and $|C''\rangle$ becomes:

$$\begin{aligned}
\arg\langle C'|C''\rangle &= \arg\langle A|C\rangle\langle C|B\rangle = \arg\langle A|C\rangle\langle C|B\rangle\langle B|A\rangle \\
&\equiv \Delta(A, B, C), \tag{2.2}
\end{aligned}$$

where the in-phase condition $\arg\langle A|B\rangle = 0$ was used. Note that the sequence of states on the right hand side of the first line of Eq. (2.2) plays an important role here. $|A\rangle$ is projected to $|B\rangle$ and the result is projected to $|C\rangle$, which is then compared to $|A\rangle$. $\Delta(A, B, C)$ is related to oriented areas because it is additive and depends on orientation, which can be expressed as:

$$\begin{aligned}
\Delta(A, B, C, D) &= \Delta(A, B, C) + \Delta(A, C, D) \\
\Delta(A, C, B) &= -\Delta(A, B, C). \tag{2.3}
\end{aligned}$$

Suppose we start with the state $|A\rangle$ at the north pole of the Bloch sphere, i. e. $|A\rangle = |+\rangle$. Let (θ, φ) be the polar and azimuthal angles for the Bloch sphere representation of the state $|B\rangle$ and $(\theta + d\theta, \varphi + d\varphi)$ for $|B + dB\rangle$, respectively. $d\theta$ and $d\varphi$ are infinitely small. $|B\rangle$ and $|B + dB\rangle$ can be written

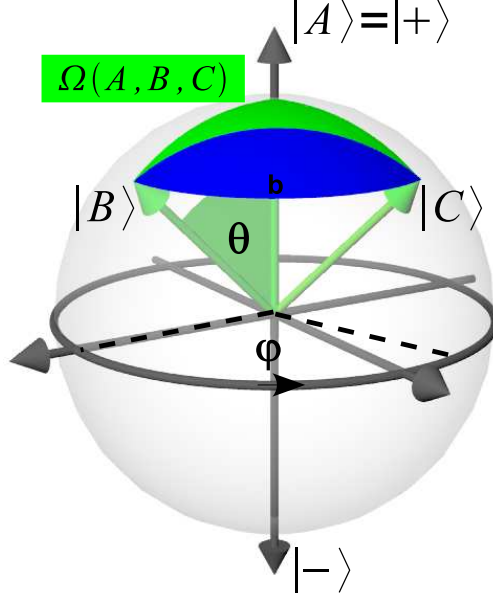


Figure 2.1: Bloch sphere description with the spherical triangle defined by the states $|A\rangle$, $|B\rangle$ and $|C\rangle$, enclosing the solid angle $\Omega(A, B, C)$ by geodesics (green). Note that the path \mathbf{a} is a geodesic while \mathbf{b} is a circle of latitude.

as

$$\begin{aligned}
 |B\rangle &= \cos\frac{\theta}{2}|+\rangle + e^{i\varphi}\sin\frac{\theta}{2}|-\rangle \\
 |B + dB\rangle &= \cos\left(\frac{\theta}{2} + \frac{d\theta}{2}\right)|+\rangle + e^{i(\varphi+d\varphi)}\sin\left(\frac{\theta}{2} + \frac{d\theta}{2}\right)|-\rangle.
 \end{aligned} \tag{2.4}$$

We can then calculate

$$\begin{aligned}
 \Delta(A, B, B + dB) &= \arg\langle A|B + dB\rangle\langle B + dB|B\rangle \\
 &= \arg\left(\cos^2\frac{\theta}{2} + \sin^2\frac{\theta}{2}\underbrace{\cos(d\varphi)}_{\simeq 1} - i\sin^2\frac{\theta}{2}\underbrace{\sin(d\varphi)}_{\simeq d\varphi}\right) \\
 &= \arctan\left(\frac{-\sin^2\frac{\theta}{2}d\varphi}{1}\right) \simeq -\sin^2\frac{\theta}{2}d\varphi \\
 &= -\frac{1}{2}(1 - \cos\theta)d\varphi,
 \end{aligned} \tag{2.5}$$

where we have used that $\cos\left(\frac{\theta}{2} + \frac{d\theta}{2}\right) \simeq \cos\frac{\theta}{2}$. On the Bloch sphere, Eq. (2.5) equals $-\frac{\Delta\Omega}{2}$, where $\Delta\Omega$ is the solid angle enclosed by the infinitesimal spherical triangle defined by the states $|A\rangle, |B\rangle$ and $|B + dB\rangle$. Thus, for the triangle

defined by $|A\rangle, |B\rangle$ and $|C\rangle$, as shown in Fig. (2.1), we can use the properties (2.3) to obtain

$$\Delta(A, B, C) = -\frac{\varphi}{2}(1 - \cos \theta) = -\frac{\Omega(A, B, C)}{2}. \quad (2.6)$$

This phase depends only on the geodesic path (on great circles) defined by the positions of the three states on the Bloch sphere. Therefore it is a so-called *geometric phase*. If the path taken from $|B\rangle$ to $|C\rangle$ is not the geodesic marked by **a** in Fig. 2.1, but the circle of latitude marked by **b**, the relative Pancharatnam phase contains also a dynamical part that is calculated as $\phi_d = -\frac{\varphi}{2} \cos \theta$. This occurs in typical neutron polarimetry experiments, where the neutron spin state $|B\rangle$ is rotated around a magnetic field axis that is parallel to the z axis of the Bloch sphere. In contrast, the field axis to achieve a rotation along **a** must be perpendicular to $|B\rangle$. The paths **a** and **b** coincide for $\theta = \pi/2$ so that $\phi_d = 0$. It is important to note, that the Pancharatnam relative phase is independent of the adiabatic approximation.

2.2 Noncyclic Geometric Phase

Employing the above concept it has been shown in [Samuel and Bhandari 1988] that the sequence of states does not need to be closed as in Eq. (2.2). All results hold for noncyclic evolutions as well. The geometric phase is in this case, as before, equal to minus half the solid angle enclosed by the geodesics on the Bloch sphere, as drawn from $|A\rangle$ to $|B\rangle$ to $|C\rangle$ and back to $|A\rangle$. However, one does not need to explicitly carry out the evolution $|C\rangle \rightarrow |A\rangle$. We say that Ω is enclosed by the path its shortest geodesic closure on the Bloch sphere. An example is shown in Fig. 2.2. Measurements of this effect by neutron optical methods has been proposed in [Wagh and Rakhecha 1995a, Wagh and Rakhecha 1995b] and experimentally demonstrated for neutron interferometry and polarimetry in [Wagh *et al.* 1998] and [Klepp *et al.* 2005], respectively.

2.3 Mixed-State Pancharatnam Phase

Trying to find an equivalent to the Pancharatnam phase concept for the more general mixed-states evolving under unitary transformations – so $\rho_A \rightarrow \rho_B = U\rho_A U^\dagger$ – or

$$\rho_A = \sum_k w_k |A_k\rangle\langle A_k| \rightarrow \rho_B = \sum_k w_k |B_k\rangle\langle B_k|,$$

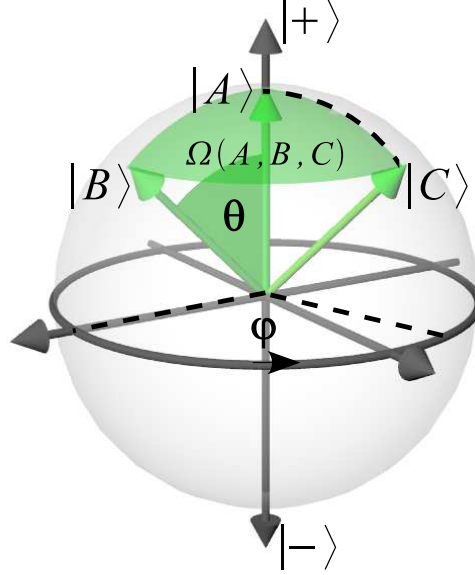


Figure 2.2: The evolution on the geodesic from $|C\rangle$ to $|A\rangle$ does not need to be carried out to obtain $-\Omega(A, B, C)/2$. The result is the same for an evolution that only goes from $|A\rangle$ to $|C\rangle$.

where w_k are the eigenvalues of the density matrices and $|B_k\rangle = U|A_k\rangle$. Each orthonormal pure state component of the input density matrix contributes with their "own" oscillation as predicted by Eq. (2.1) to the overall interference pattern. The total intensity is then proportional to

$$\begin{aligned} I &\propto \sum_k w_k |e^{i\chi}|A_k\rangle + |B_k\rangle|^2 \\ &= 2 + 2 \sum_k w_k |\langle A_k|B_k\rangle| \cos(\chi - \arg\langle A_k|B_k\rangle), \end{aligned} \quad (2.7)$$

which is calculated in the same manner as Eq. (2.1), including the fact that $\sum_k w_k = 1$. Noting that

$$\begin{aligned} \text{Tr}(U\rho_A) &= \text{Tr}\left(\sum_k w_k U|A_k\rangle\langle A_k|\right) = \sum_i \sum_k w_k \langle i|U|A_k\rangle\langle A_k|i\rangle \\ &= \sum_i \sum_k w_k \underbrace{\langle A_k|i\rangle\langle i|U|A_k\rangle}_{\in\mathbb{C}} = \sum_k w_k |\langle A_k|U|A_k\rangle| e^{i\arg\langle A_k|U|A_k\rangle}, \end{aligned}$$

one may rewrite Eq. (2.7) to

$$I \propto 2 + 2|\text{Tr}(U\rho_A)| \cos(\chi - \arg\text{Tr}(U\rho_A)). \quad (2.8)$$

In analogy to Eq. (2.1), the interference pattern is shifted when $U \neq \mathbb{1}$. If we use pure states in Eq. (2.8), the phase shift and the visibility reduce to Pancharatnam's original formulas. The sequence of states that leads to the pure state phase $\Delta(A, B, C)$ can be adopted for a sequence of density operators. All pure state components undergo the same unitary U (in the following U takes the system through $\rho_A \rightarrow \rho_B \rightarrow \rho_C$), so that we can write down the quantities $\Delta(A_k, B_k, C_k) = \arg \langle A_k | U | A_k \rangle$ for each of them. The generalization of Eq. (2.2) for mixed states is then

$$\Delta(A, B, C) = \arg \left(\sum_k w_k |\langle A_k | U | A_k \rangle| e^{i \arg \langle A_k | U | A_k \rangle} \right). \quad (2.9)$$

Equation (2.9) depends exponentially on the Pancharatnam phases of all pure state components and therefore $\Delta(A, B, C)$ is nonadditive, in contrast to Eq. (2.2). Δ still depends on the orientation of U :

$$\Delta(A, B, C) = -\Delta(A, C, B). \quad (2.10)$$

For example, a mixed input state of qubits with the two components $|+\rangle$ and $|-\rangle$ can be described by $\rho_A = \frac{1}{2}(\mathbb{1} + r\sigma_z)$. One can consider a spin-polarized neutron beam, for instance. r is the degree of polarization (the purity), which can be interpreted as the length of the polarization vector $\vec{r} = \text{Tr}(\rho_A \vec{\sigma})$ with $0 < r \leq 1$. The visibilities are equal for $|+\rangle$ and $|-\rangle$, the phases related as $\Delta(A_+, B_+, C_+) = -\Delta(A_-, B_-, C_-) = -\Omega/2$. The states pointing to the positions A_+, B_+ and C_+ on the Bloch sphere are orthogonal to the states pointing to the positions A_-, B_- and C_- , respectively. We obtain

$$\begin{aligned} \Delta(A, B, C) &= \arg \left(\frac{1}{2}(1+r)e^{-i\Omega/2} + \frac{1}{2}(1-r)e^{i\Omega/2} \right) \\ &= \arg \left(\cos \frac{\Omega}{2} - ir \sin \frac{\Omega}{2} \right) \\ &= -\arctan \left(r \tan \frac{\Omega}{2} \right). \end{aligned} \quad (2.11)$$

The same can be done for the visibility, which results in:

$$\begin{aligned} \mathcal{V} &= |\text{Tr}(U\rho_A)| = \left| \sum_k w_k |\langle A_k | U | A_k \rangle| e^{i \arg \langle A_k | U | A_k \rangle} \right| \\ &= \nu \sqrt{\cos^2 \frac{\Omega}{2} + r^2 \sin^2 \frac{\Omega}{2}}. \end{aligned} \quad (2.12)$$

2.4 Pancharatnam Phase in Neutron Polarimetry

How can the obtained formulas be tested in an experiment? As already mentioned, a demonstration of Eq. (2.11) has been accomplished in [Du *et al.* 2003] [Du *et al.* 2003], while in [Ericsson *et al.* 2003a] also the validity of Eq. (2.12) has been demonstrated. The proposal for a neutron polarimetry measurement of the Pancharatnam phase [Wagh and Rakhecha 1995b] has been adopted for mixed input states in [Larsson and Sjöqvist 2003] and implemented in [Klepp *et al.* 2005] and, with a changed experimental setup, in [Sponar *et al.* 2006]. [Sponar *et al.* 2006]. However, in the latter two references, the mixed input state was produced by doing the measurement with almost 100% polarization. The data was recorded one time with an upstream DC-flipper turned off and a second time with this device turned on, which resulted in the incident states $|+\rangle$ and $|-\rangle$, respectively. Two intensity oscillations, mutually shifted by π , were obtained. Calculating a weighted average of the data of the two curves was assumed to give the curve one *would have* obtained for a particular input purity. Corresponding to the chosen weights, the result for a specific "mixed input state" was obtained. While those results already confirmed the theoretical predictions for the Sjöqvist mixed-state phase, a demonstration for real mixtures was needed. In the following, a formal treatment of the experimental setup and a calculation of expected results is shown.

2.4.1 The Pure State Case

A neutron beam propagating in y direction interacting with static magnetic fields $\vec{B}(y)$ is described by the Hamiltonian

$$H = -\hbar^2/2m\vec{\nabla}^2 - \mu\vec{\sigma}\vec{B}(y).$$

m and μ are the mass and the magnetic moment of the neutron, respectively. $\vec{\sigma}$ is the Pauli vector operator. Zeeman splitting within $\vec{B}(y)$ leads to solutions of the Schrödinger equation

$$\cos(\vartheta/2)|k_+\rangle|+\rangle + e^{i\alpha}\sin(\vartheta/2)|k_-\rangle|-\rangle, \quad (2.13)$$

where $|k_{\pm}\rangle$ are the momentum and $|\pm\rangle$ the spin eigenstates within the field $\vec{B}(y)$. ϑ and α denote the polar and azimuthal angles determining the direction of the polarization with respect to $\vec{B}(y)$. $k_{\pm} \simeq k \mp \Delta k$, where k is the momentum of the free particle and $\Delta k = m\mu|\vec{B}(y)|/\hbar^2 k$ is the field-induced

momentum shift. Δk can be detected from Larmor precession. Omitting the coupling of momentum and spin for the moment, we focus on the evolution of superposed spin eigenstates resulting in Larmor precession of the polarization vector \vec{r} . Consider the unitary, unimodular operator

$$U(\xi', \delta', \zeta') = e^{-i\delta'} \cos \xi' |+\rangle \langle +| - e^{-i\zeta'} \sin \xi' |+\rangle \langle -| + e^{i\zeta'} \sin \xi' |-\rangle \langle +| + e^{i\delta'} \cos \xi' |-\rangle \langle -|. \quad (2.14)$$

It is capable of describing the evolution of the system within static magnetic fields. The set of SU(2) parameters (ξ', δ', ζ') is related to the so-called Cayley-Klein parameters a, b via $a = e^{-i\delta'} \cos \xi'$ and $b = -e^{-i\zeta'} \sin \xi'$ (see e.g. [Sakurai 1994]). As already stated, the Pancharatnam relative phase ϕ for pure input states accumulated during such a particular evolution U_ϕ , say, can be written as

$$\phi = \arg \langle + | U_\phi | + \rangle, \quad (2.15)$$

with the assumed initial state $|+\rangle$. The visibility for pure input states is given by

$$\nu = |\langle + | U_\phi | + \rangle|. \quad (2.16)$$

The effects of an evolution written in the form Eq. (2.14) on the orthogonal states $|+\rangle$ and $|-\rangle$ are

$$\begin{aligned} U_\phi |+\rangle &= \cos \xi' e^{-i\delta'} |+\rangle + \sin \xi' e^{i\zeta'} |-\rangle \\ U_\phi |-\rangle &= -\sin \xi' e^{-i\zeta'} |+\rangle + \cos \xi' e^{i\delta'} |-\rangle. \end{aligned} \quad (2.17)$$

One finds that the Pancharatnam phase is given by

$$\begin{aligned} \phi &= \arg \left(\langle + | \left[\cos \xi' \cdot e^{-i\delta'} |+\rangle + \sin \xi' \cdot e^{i\zeta'} |-\rangle \right] \right) \\ &= -\delta' + \arg(\cos \xi') \end{aligned} \quad (2.18)$$

and the associated pure state visibility is

$$\nu = |\cos \xi'|. \quad (2.19)$$

Note that both the Pancharatnam phase and the visibility depend only on the SU(2) parameters δ' and ξ' , respectively.

The neutron polarimeter experiment proposed in [Wagh and Rakhecha 1995b] is sketched in Fig. 2.3. The following calculations should make clear how ϕ and ν can be measured using this apparatus.

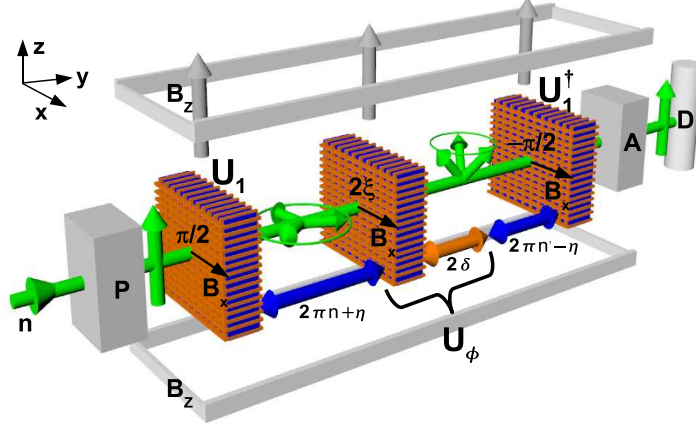


Figure 2.3: Sketch of neutron polarimetry setup for phase measurement with overall guide field B_z , polarizer P , three DC-coils to implement unitary operations U_1 , U_1^\dagger , U_ϕ , analyzer A and detector D . Greek letters denote polarization rotation angles. Shifting the second coil induces an additional dynamical phase $\eta/2$ resulting in intensity oscillations.

A monochromatic neutron beam passes the polarizer P preparing it in the up state $|+\rangle$ with respect to a magnetic guide field in z direction that we call B_z . Next, the beam approaches a DC coil with its field B_x pointing to the x direction. B_x is chosen such that it carries out the transformation $U_1 \equiv U(\pi/4, 0, -\pi/2)$, corresponding to a $+\pi/2$ rotation around the $+x$ axis. This can also be denoted as

$$U_1 = \frac{1}{\sqrt{2}} (|+\rangle\langle+| - i|+\rangle\langle-| - i|-\rangle\langle+| + |-\rangle\langle-|),$$

or in matrix form:

$$U_1 = \frac{1}{\sqrt{2}} \begin{pmatrix} 1 & -i \\ -i & 1 \end{pmatrix}. \quad (2.20)$$

Instead of Eq. (2.14), to receive Eq. (2.20), one usually employs the well-known spin state rotation formalism, in which the direction of the rotation axis $\vec{\beta}/|\vec{\beta}|$ ($+x$ in this case) and the rotation angle β ($\pi/2$ in this case) must be given. The unitary rotation operator is then:

$$U(\vec{\beta}) = \mathbb{1} \cos \frac{\beta}{2} - i\vec{\sigma} \frac{\vec{\beta}}{|\vec{\beta}|} \sin \frac{\beta}{2}. \quad (2.21)$$

By comparison of the matrix elements of Eqs. (2.14) and (2.21) one easily finds the parameter set for a given coil operation.

After U_1 the resulting state of the system is a coherent superposition of the two orthogonal spin eigenstates:

$$|\psi_0\rangle = 1/\sqrt{2}(|+\rangle - i|-\rangle). \quad (2.22)$$

A subsequent coil, represented by $U(\xi, 0, -\pi/2)$, is set to cause a rotation around the $+x$ axis by an angle 2ξ . This second coil and the following propagation distance within B_z – corresponding to a rotation angle 2δ around the $+z$ axis – define an evolution $U_\phi \equiv U(\xi, \delta, \zeta)$. Undergoing the transformation U_ϕ , the two spin eigenstates $|\pm\rangle$ acquire opposite Pancharatnam phase $\phi = \arg\langle\pm|U_\phi|\pm\rangle = \mp\delta$. A third coil, that we refer to as U_1^\dagger , exactly reverses the action of the first one and would therefore transform a state $|\psi_0\rangle$ back to $|+\rangle$. Clearly, the state of the system entering the third coil equals $|\psi_0\rangle$ only if $U_\phi = \mathbb{1}$. ϕ can be extracted by applying an extra dynamical phase shift $\mp\frac{1}{2}\eta$ to $|\pm\rangle$. It is implemented by adjusting both inter-coil distances from first to second and second to third coil to polarization rotation angle equivalents of $2\pi n + \eta$ and $2\pi n' + 2\delta - \eta$, respectively (n, n' are integer). By variation of the position of the second coil, these rotation angles are varied stepwise to yield intensity oscillations from which ϕ can then be calculated. We refer to the transformations carried out along these distances within the guide field as $U_\eta \equiv U(0, \eta/2)$ and U_η^\dagger . Note that, because of $\xi = 0$, the parameter ζ is undetermined and, therefore, omitted in U_η . After projection on the state $|+\rangle$ by the analyzer A , the phase $\phi = -\delta$ and its visibility $\nu = |\cos\xi|$ can be computed as functions of the maxima and minima of the expected intensity, I_{max} and I_{min} , in the following way:

$$I \propto |\langle+|U_1^\dagger U_\eta^\dagger U_\phi U_\eta U_1|+\rangle|^2$$

leads, by extensive use of Eq. (2.14), to:

$$I \propto \cos^2 \xi \cos^2 \delta + \sin^2 \xi \cos^2(\zeta - \eta). \quad (2.23)$$

In the second term of this expression, depending on the direction of the axis of rotation for U_1 (either x or y), one finds $\cos^2(\zeta - \eta)$ or $\sin^2(\zeta - \eta)$. The intensity is completely determined by the three SU(2) parameters ξ, δ, ζ and the angle η . It oscillates sinusoidally with a period π in η between its maxima and minima

$$I_{min} = \cos^2 \xi \cos^2 \delta \quad (2.24)$$

and

$$I_{max} = \cos^2 \xi \cos^2 \delta + \sin^2 \xi. \quad (2.25)$$

Note that $I = I'/I_n$, $I_{min} = I'_{min}/I_n$ and $I_{max} = I'_{max}/I_n$, where I', I'_{min} and I'_{max} are the measured intensities and I_n is a measured normalization

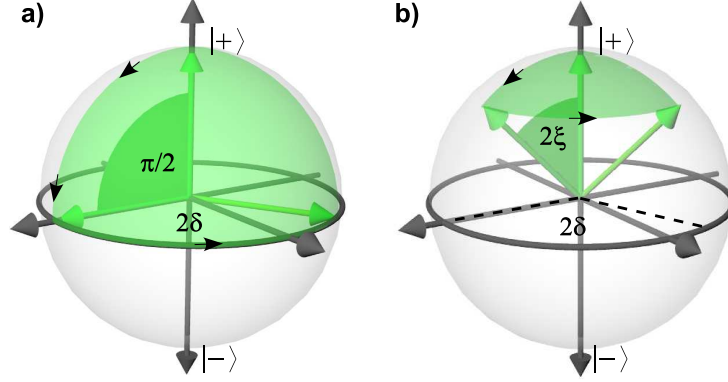


Figure 2.4: Evolution of the $|+\rangle$ state induced by U_ϕ , associated to:
a) Purely (noncyclic) geometric phase ($2\xi = \pi/2$). b) Combinations of dynamical and geometric phase on the Bloch sphere ($0 < 2\xi < \pi/2$).

constant to be discussed in Section 2.6.10 in more detail. The Pancharatnam phase $\phi = -\delta$ in terms of these can be calculated from (2.24):

$$\begin{aligned}
\cos^2 \delta &= \frac{I_{min}}{\cos^2 \xi} \\
&= \frac{I_{min}}{1 - \sin^2 \xi - \cos^2 \xi \cos^2 \delta + \cos^2 \xi \cos^2 \delta} \\
\Rightarrow \phi &= \arccos \sqrt{\frac{I_{min}}{1 - I_{max} + I_{min}}}. \tag{2.26}
\end{aligned}$$

The visibility ν becomes

$$\begin{aligned}
\nu &= |\cos \xi| \\
&= \sqrt{\cos^2 \xi} \\
&= \sqrt{1 - \sin^2 \xi - \cos^2 \xi \cos^2 \delta + \cos^2 \xi \cos^2 \delta} \\
&= \sqrt{1 - I_{max} + I_{min}}. \tag{2.27}
\end{aligned}$$

As before in Eq. (2.6), ϕ_g and the total Pancharatnam phase ϕ are related to the path by the polar and azimuthal angles 2ξ and 2δ , so that the pure state geometric phase becomes

$$\phi_g = \phi - \phi_d = -\delta[1 - \cos(2\xi)], \tag{2.28}$$

while its dynamical counterpart is

$$\phi_d = -\delta \cos(2\xi). \tag{2.29}$$

By proper choice of 2ξ and 2δ , U_ϕ can be set to generate purely geometric, purely dynamical, or arbitrary combinations of both phases as shown in Fig. 2.4.1. For instance, consider an evolution that takes $|+\rangle$ to the equator (carried out by the second DC coil) and along the latter for an angle of 2δ (carried out by the guide field B_z). The evolution can be divided into two parts, $U_\phi^{(1)}$ and $U_\phi^{(2)}$, that can be written as:

$$U_\phi^{(1)} = \frac{1}{\sqrt{2}}(|+\rangle\langle+| - i|+\rangle\langle-| - i|- \rangle\langle+| + |- \rangle\langle-|)$$

and

$$U_\phi^{(2)} = e^{-i\delta}|+\rangle\langle+| + e^{i\delta}|- \rangle\langle-|, \quad (2.30)$$

so that

$$\begin{aligned} U_\phi &= U_\phi^{(2)}U_\phi^{(1)} \\ &= \frac{1}{\sqrt{2}}(e^{-i\delta}|+\rangle\langle+| - ie^{-i\delta}|+\rangle\langle-| - ie^{i\delta}|- \rangle\langle+| + e^{i\delta}|- \rangle\langle-|). \end{aligned}$$

Comparing this to Eq. (2.14), one sees that the particular set of SU(2) parameters for U_ϕ is $(\xi = \pi/4, \delta, \zeta = \delta - \pi/2)$. By choosing $2\xi = \pi/2$ one sets the accumulated Pancharatnam phase to be purely geometric.

For $2\xi = \pi$, using Eqs. (2.24) and (2.25), one can see that the intensity oscillates between the values 0 and 1. Consequently, the contrast (or "visibility") of interference fringes

$$C = \frac{I_{max} - I_{min}}{I_{max} + I_{min}} \quad (2.31)$$

is at maximum while $\nu = 0$. This is correct, because the measured pattern shows interference between the $|+\rangle$ and $|- \rangle$ states, while ν denotes the visibility of the interference between the initial state $|+\rangle$ and the evolved state $U_\phi|+\rangle$.

2.4.2 The Mixed State Case

A neutron beam with incident purity r'_0 along the $+z$ axis ($\vec{r}'_0 = (0, 0, r'_0)$) is described by the density operator

$$\rho_{in}(r'_0) = 1/2(\mathbb{1} + r'_0\sigma_z).$$

Calculating

$$\begin{aligned}\rho_{out} &= \underbrace{U_1^\dagger U_\eta^\dagger U_\phi U_\eta U_1}_{\bar{U}} \rho_{in} \underbrace{U_1^\dagger U_\eta^\dagger U_\phi^\dagger U_\eta U_1}_{\bar{U}^\dagger} \\ &= \frac{1}{2} \left(\mathbb{1} + r'_0 (|\bar{U}|+\rangle\langle+|\bar{U}^\dagger - |\bar{U}|-\rangle\langle-|\bar{U}^\dagger) \right),\end{aligned}$$

the state of the outgoing beam after undergoing the transformations as described in the previous Sections, one finds the intensity

$$\begin{aligned}I^\rho &\propto Tr(|+\rangle\langle+|\rho_{out}) \\ &= \frac{1}{2} + \frac{1}{2} r'_0 \underbrace{Tr(|+\rangle\langle+|\bar{U}|+\rangle\langle+|\bar{U}^\dagger)}_{=I} - \frac{1}{2} r'_0 \underbrace{Tr(|+\rangle\langle+|\bar{U}|-\rangle\langle-|\bar{U}^\dagger)}_{=1-I} \\ &= \frac{1-r'_0}{2} + r'_0 (\cos^2 \xi \cos^2 \delta + \sin^2 \xi \cos^2(\zeta - \eta))\end{aligned}\quad (2.32)$$

after the analyzer A , with I as defined in Eq. (2.23). Considering the maxima and minima $I_{max}^\rho = \tilde{I}_{max}^\rho / I_n^\rho$, $I_{min}^\rho = \tilde{I}_{min}^\rho / I_n^\rho$ of η -induced oscillations of $I^\rho = \tilde{I}^\rho / I_n^\rho$ one obtains the mixed state phase and visibility [Larsson and Sjöqvist 2003]

$$\Phi(r'_0) = \arccos \sqrt{\frac{[I_{min}^\rho - 1/2(1-r'_0)]/r'_0}{r'_0[1/2(1+r'_0) - I_{max}^\rho] + [I_{min}^\rho - 1/2(1-r'_0)]/r'_0}} \quad (2.33)$$

$$\mathcal{V}(r'_0) = |Tr(U_\phi \rho_{in})| = \sqrt{r'_0[1/2(1+r'_0) - I_{max}^\rho] + [I_{min}^\rho - 1/2(1-r'_0)]} / \mathcal{E}_0 \quad (2.34)$$

with the measured intensities $I^\rho, I_{max}^\rho, I_{min}^\rho$ and a normalization factor I_n^ρ (see also Section 2.6.10). I_0^ρ is the intensity measured at $U_\phi = \mathbb{1}$.

Note that Eqs. (2.33) and (2.34) reduce to the pure state formulas for the phase and visibility – Eq.(2.18) and Eq.(2.19) – for $r'_0 = 1$.

The theoretical predictions for the specific notation for the mixed state phase and visibility in terms of SU(2) parameters are

$$\Phi(r'_0) = -\arctan(r'_0 \tan \delta) \quad (2.35)$$

$$\mathcal{V}(r'_0) = \nu \sqrt{\cos^2 \delta + r_0'^2 \sin^2 \delta}, \quad (2.36)$$

a result already obtained in Section 2.3.

2.5 Entanglement of Spin and Momentum

The description of the mixed-state phase and the measurement concept using polarized neutrons given above is satisfactorily described by the formalism used in the previous Sections. There are no open questions with respect to the experiment that is discussed. Nevertheless, it is interesting to tackle the problem with a more rigorous mathematical description that is *not* necessary and, moreover, *more* complicated. Personally, I hope that this could help to give a better understanding of the subject.

The measurable effect of rotation of the polarization vector within a static magnetic field originates from the Zeeman splitting of the up and down spin components of the neutron state vector with respect to the quantization axis defined by the field. The up component loses, while the down component gains kinetic energy (see, for instance [Suda 2006]) when entering the static magnetic field. In the following, the situation is shortly summarized.

The one-dimensional Schrödinger equation for the free particle moving in y direction

$$H\psi(y, t) = -\frac{\hbar^2}{2m} \frac{\partial^2}{\partial y^2} \psi(y, t) = i\hbar \frac{\partial}{\partial t} \psi(y, t)$$

can be solved by making the *Ansatz* $\psi(y, t) = Ae^{i(ky - \omega t)}$. This yields the dispersion relation

$$E = \hbar\omega = \frac{\hbar^2 k^2}{2m}.$$

For neutrons in a static magnetic field the total energy is conserved and therefore kinetic energy must increase/decrease when the potential energy decreases/increases for neutrons with spin down/up. One can write

$$E = \frac{\hbar^2 k^2}{2m} = \frac{\hbar^2 k_{\pm}^2}{2m} \pm \mu B,$$

from which follows that $k^2 = k_{\pm}^2 \pm \frac{2m\mu B}{\hbar^2}$. The modified kinetic energies associated with the two spin eigenstates become

$$\begin{aligned} k_{\pm} &= k \sqrt{1 \mp \frac{2m\mu B}{\hbar^2 k^2}} = k \left(1 \mp \frac{1}{2} \frac{2m\mu B}{\hbar^2 k^2} - \frac{1}{8} \left(\frac{2m\mu B}{\hbar^2 k^2} \right)^2 \mp \dots \right) \\ &\simeq k \mp \frac{m\mu B}{\hbar^2 k} = k \mp \Delta k. \end{aligned}$$

The approximation is well-justified as long as E and therefore k is much larger than μB . This is definitely the case for all experiments described in

this thesis. Typically, $E \sim 20$ meV for thermal neutrons and $\mu B \sim 60$ neV for a magnetic field of 1 T.

Next, the Schrödinger equation for neutrons with a magnetic potential (also called Pauli equation) induced by a magnetic field in z direction

$$\left(-\frac{\hbar^2}{2m} \frac{\partial^2}{\partial y^2} - \mu \sigma_z B_z(y, t) \right) \psi(y, t) = i\hbar \frac{\partial \psi(y, t)}{\partial t} \quad (2.37)$$

has the solutions

$$\psi = a|+\rangle + b|-\rangle = f_+(y, t) \cos \frac{\vartheta}{2} |+\rangle + f_-(y, t) e^{i\alpha} \sin \frac{\vartheta}{2} \quad (2.38)$$

(see, for instance, [Rauch and Werner 2000]), where

$$f_{\pm}(y, t) = \frac{1}{\sqrt{2\pi}} \int a_{\pm}(k_{\pm}) e^{i(ky \mp \Delta ky - \omega(k)t)}.$$

The functions f_{\pm} describe the wave packets of the up and down spin components. As long as δk , the width of the momentum distribution function $g_{\pm}(k) = |a_{\pm}(k)|^2$, is much larger than Δk , one can write $|a_{\pm}(k_{\pm})| \simeq |a_{\pm}(k)|$. One can take the problem as a semiclassical one – the neutron as a pointlike particle with a 3D vector ”piercing through it”. One can then calculate the components of the polarization vector $\vec{r} = \langle \psi | \vec{\sigma} | \psi \rangle$ as shown in [Mezei 1988]. The polar angle ϑ is determined by $g_+(k)$ and $g_-(k)$. The azimuthal angle α – the relative phase between $|+\rangle$ and $|-\rangle$ – is equal to $2y\Delta k$. If Δk gets large enough and the corresponding spatial separation exceeds the coherence length $l_c \simeq \lambda^2 / \Delta \lambda$ (the separation distance at which the contrast is, for instance, $1/e$ or $1/2$ of its maximum value), interference vanishes [Badurek *et al.* 1993]. The contrast of the measured oscillations, resulting from Larmor precession of the polarization vector, decreases and is finally lost. In past experiments the Zeeman effect and the related so-called *longitudinal* Stern-Gerlach effect were investigated for neutrons [Zeilinger and Shull 1979, Alefeld *et al.* 1981]. From the above, we can conclude that it is only in momentum-space where the relative phase shifts between $|+\rangle$ and $|-\rangle$ are induced. Taking a look at Eq. (2.38), we can say that the neutron state vector evolves within a Hilbert space that is formed by two subspaces: Spin space and momentum or k -space. This product space is denoted as $\mathcal{H} = \mathcal{H}_k \otimes \mathcal{H}_s$. Therefore, in addition to spin, we have a second ”two-level system” (accelerated and decelerated part) with the basis states $|k_+\rangle$, associated with $|+\rangle$ and $|k_-\rangle$, associated with $|-\rangle$. The coupling of momentum and spin can be seen as a form of entanglement of degrees of freedom. As in many up-to-date perfect crystal interferometer experiments, the entanglement is manifest between degrees of freedom of *one* particle instead of separate particles (see,

for instance, [Hasegawa *et al.* 2003]). The same occurs in descriptions of the Stern-Gerlach apparatus (for example, in [Zurek 2002]), where the state of the moving particles and the detector state form an entangled state. The notation is also equivalent to the usual way of describing the electron states of hydrogen atoms in basic quantum mechanics. For instance one writes $|l, m\rangle \otimes |s, m_s\rangle$, where l, m, s and m_s are usually the quantum numbers for orbital momentum, its projection to the z axis, the spin and its projection to the z axis, respectively.

As already mentioned above, while traveling within the static B field, wave packets associated with two different values of momentum get separated also in position space. The question what the requirements are for a physical property to be considered as separate degree of freedom that can be entangled with a second one and the usefulness of this idea, is still under discussions. It is conceivable that the state vector for polarized neutrons in a static magnetic field can, due to the spatial separation, be extended to

$$|y_+\rangle \otimes |k_+\rangle \otimes |+\rangle + |y_-\rangle \otimes |k_-\rangle \otimes |-\rangle.$$

$|y_\pm\rangle$ could be associated with the position of either one of the wavepackets with respect to the center of both in flight direction y . In the following, we will restrict ourselves to the case denoted in Eqs. (2.13) or (2.38), with only two entangled degrees of freedom.

Including the coupling of momentum and spin - responsible for the spin evolution in our treatment - we write the input state before the first coil as $|k_++\rangle$. The operator (2.14) must then be rewritten:

$$\begin{aligned} U'_\phi &= \cos \xi \cos \delta \cdot \mathbb{1}^{(k)} \otimes \mathbb{1}^{(s)} - i \sin \xi \cos \zeta \cdot \sigma_y^{(k)} \otimes \sigma_x^{(s)} \\ &\quad - i \sin \xi \sin \zeta \cdot \sigma_y^{(k)} \otimes \sigma_y^{(s)} - i \cos \xi \sin \delta \cdot \mathbb{1}^{(k)} \otimes \sigma_z^{(s)} \\ &= \begin{pmatrix} e^{-i\delta} \cos \xi & 0 & 0 & -e^{-i\zeta} \sin \xi \\ 0 & e^{i\delta} \cos \xi & -e^{i\zeta} \sin \xi & 0 \\ 0 & e^{-i\zeta} \sin \xi & e^{-i\delta} \cos \xi & 0 \\ e^{i\zeta} \sin \xi & 0 & 0 & e^{i\delta} \cos \xi \end{pmatrix}, \end{aligned} \quad (2.39)$$

where we have used the basis formed by the four vectors $|k_\pm\pm\rangle, |k_\pm\mp\rangle$. (k) and (s) refer to the momentum and spin degrees of freedom, respectively. This operator is a combination of a general unitary, unimodular operator in two dimensions and what is referred to as controlled gate in quantum information technology [Nielsen and Chuang 2000]. The conditional dynamics expressed by U'_ϕ implies that the coherent evolution of one subsystem depends on the state of the other subsystem, as it is known from NMR experiments [Du *et al.* 2003, Jones *et al.* 2000], for instance.

To become more familiar with the concept, we write down the explicit calculation of Eq. (2.23) with the help of Eq. (2.39). The input state is

$$|\psi_0\rangle = |k_{++}\rangle = \begin{pmatrix} 1 \\ 0 \\ 0 \\ 0 \end{pmatrix}.$$

The first coil affects this state as

$$\begin{aligned} |\psi_1\rangle &= U'_1 |\psi_0\rangle = \frac{1}{\sqrt{2}} \begin{pmatrix} 1 & 0 & 0 & -i \\ 0 & 1 & i & 0 \\ 0 & i & 1 & 0 \\ -i & 0 & 0 & 1 \end{pmatrix} \begin{pmatrix} 1 \\ 0 \\ 0 \\ 0 \end{pmatrix} \\ &= \frac{1}{\sqrt{2}} (|k_{++}\rangle - i|k_{--}\rangle). \end{aligned}$$

The distance between the first and the second coil is equivalent to a phase shifting operation:

$$\begin{aligned} |\psi_2\rangle &= U'_\eta |\psi_1\rangle = \begin{pmatrix} e^{-i\frac{\eta}{2}} & 0 & 0 & 0 \\ 0 & e^{i\frac{\eta}{2}} & 0 & 0 \\ 0 & 0 & e^{-i\frac{\eta}{2}} & 0 \\ 0 & 0 & 0 & e^{i\frac{\eta}{2}} \end{pmatrix} \begin{pmatrix} 1 \\ 0 \\ 0 \\ -i \end{pmatrix} \\ &= \frac{1}{\sqrt{2}} (e^{-i\frac{\eta}{2}} |k_{++}\rangle - ie^{i\frac{\eta}{2}} |k_{--}\rangle). \end{aligned}$$

In the same manner we can calculate the effect of the SU(2) transformation (the second coil together with the specific flight distance within the guide field):

$$\begin{aligned} |\psi_3\rangle &= U'_\phi |\psi_2\rangle \\ &= \frac{1}{\sqrt{2}} \left(e^{i(\delta-\frac{\eta}{2})} \cos \xi + ie^{-i(\zeta-\frac{\eta}{2})} \sin \xi \right. \\ &\quad \left. + e^{i(\zeta-\frac{\eta}{2})} \sin \xi - ie^{-i(\zeta-\frac{\eta}{2})} \cos \xi \right). \end{aligned}$$

After the second inter-coil distance and the third coil, the state becomes

$$\begin{aligned} |\psi_4\rangle &= U_1^\dagger U_\eta^\dagger |\psi_3\rangle \\ &= \frac{1}{2} \left([(e^{i\delta} + e^{-i\delta}) \cos \xi + (e^{-i(\zeta-\eta)} + e^{i(\zeta-\eta)}) i \sin \xi] |k_{++}\rangle \right. \\ &\quad \left. + [(e^{i\delta} - e^{-i\delta}) i \cos \xi + (e^{i(\zeta-\eta)} - e^{-i(\zeta-\eta)}) \sin \xi] |k_{--}\rangle \right). \end{aligned}$$

The corresponding density operator can be written as

$$\begin{aligned}\rho &= |\psi_4\rangle\langle\psi_4| \\ &= |k_{++}\rangle\langle k_{++}| [\cos^2 \xi \cos^2 \delta + \sin^2 \xi \cos^2(\zeta - \eta)] + \dots\end{aligned}$$

All other terms drop out after the final projection measurement by the analyzer so that we end up with

$$I \propto \text{Tr}[\mathbb{1} \otimes |+\rangle\langle +| \rho] = \cos^2 \xi \cos^2 \delta + \sin^2 \xi \cos^2(\zeta - \eta),$$

which is the same as Eq. (2.23). For mixed states we denote the input state as the density operator

$$\rho_{in}(r'_0) = \frac{(1+r'_0)}{2} |k_{++}\rangle\langle k_{++}| + \frac{(1-r'_0)}{2} |k_{--}\rangle\langle k_{--}|.$$

The result for mixed states is equivalent to Eq. (2.32). It might be important to note that the operator Eq. (2.39) was found by careful construction. It was not found in literature in this form. It is possible, that some inconsistency or other problem exists that prevents its use for the given task. So far, it provides for the correct results. There is hope that it can also be used for the formal treatment of related problems in neutron optics [Sponar *et al.* 2008a].

2.6 Experiment

For the measurements of the mixed-state phase one of the beam ports of the polarized neutron facility at the 250 kW TRIGA reactor at the Atominstitut, Vienna (see Fig. 2.5) was employed. The experimental methods used in the mixed-state phase measurements are described in details. For the remaining Sections of this thesis, directions are defined as in Fig. 2.3. In the meanwhile, the radiation shielding and monochromator angles have been changed, so that the parameters given in the following Sections are not valid any more. For a detailed description of the new setup see [Schmitzer 2009].

2.6.1 Detectors

As detector recording intensity oscillations and as monitor that gives additional information about the reactor power fluctuations, the usual ^3He tubes of small diameter (~ 1 cm) were used. The signal detector ("coffee box") contained two of them next to each other (aligned perpendicular to the flight direction), to completely cover the beam cross-section. Its background counting rate when wrapped up in Cd sheets within a layer of borated plastic bricks



Figure 2.5: The TRIGA reactor at the Atominstitut, Vienna.

(NEUTRO STOP) was finally ~ 0.3 cts/s which is one to three orders of magnitude less than the measured signal. The single monitor tube was mounted within a small (insufficient) shielding to reduce the background counting rate that was finally as high as ~ 4 cts/s. For the monitor, such a high background does not pose a problem, because its count rate was ~ 1500 cts/s. The background was subtracted by the software for both detectors. In the plots of measured data that will follow, either intensities (counts per unit time) or normalized intensities (detector counts per unit time divided by monitor counts per unit time) are given.

2.6.2 Time Of Flight measurements - TOF

To start with setting up the experiment, the mean wavelength λ and the spectral width $\Delta\lambda/\lambda$ at our beam port was measured by the *Time Of Flight* (TOF) method. An example of obtained data is shown in Fig. 2.6. The spectrum emitted by the reactor core approaches a pyrolytic graphite mosaic crystal. Bragg reflection from this mosaic monochromator provides for broader wavelength distribution and therefore higher intensities than it is the case with perfect crystal monochromators. Since, at that time, the po-

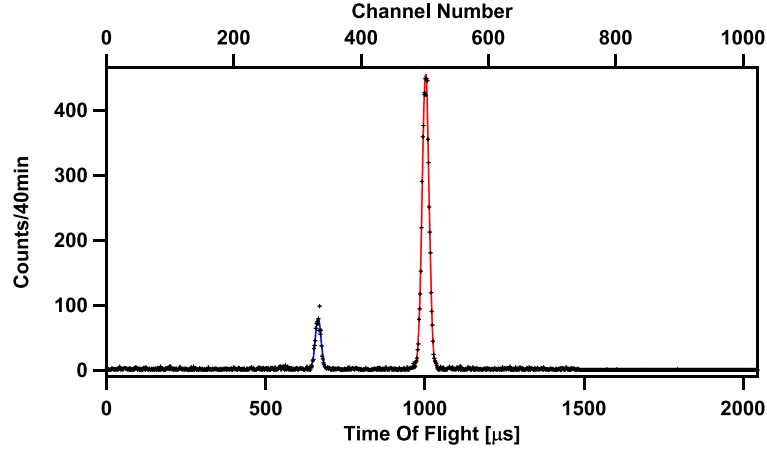


Figure 2.6: Typical data obtained from a TOF measurement. The peaks arising from first (right) and second order (left) intensity are clearly visible. Here, the distance from the center of the chopper housing to the center of the detector was about 135 cm. Note that the intensity is low: The detector was placed behind polarizer and analyzer supermirrors. The region starting from about 1.5 ms is "dead time". Also there, channel numbers are shown by the measurement software, but the time for half a chopper rotation is shorter.

larizing supermirror was installed at its fixed position within the shielding [Buchelt 1997], we put a chopper into the polarized beam trajectory (~ 20000 rpm, as calculated from Fig. 2.6). A photo-electric relay is opened and closed twice per rotation and the resulting TTL pulse is passed on to a Multi-Channel-Analyzer. The pulse is the start signal for the measurement in which each channel number is assigned to the arriving neutrons counted within the channel width that was typically $2 \mu\text{s}$. Each channel number can be related to a particular time of flight, because the distance between the chopper and the detector is known. Here, it is essential to use ^3He detectors. The interaction cross-section of neutrons for ^3He is larger than for ^{10}B . For that reason the ^3He detectors can be built with much smaller volumes at comparable detection efficiencies. This increases the time resolution of the TOF measurement, that is in our case of the order of $20 \mu\text{s}$ (see FWHM in Fig. 2.6), while the detector resolution is of the order of $5 \mu\text{s}$.

One knows that the momentum of particles is related to their wavelength λ by $p = \hbar k = mv = h/\lambda$ and therefore $\lambda = h/mv = ht/mL$. L and t are the length of the flight path from the chopper to the detector and the time of flight, respectively. $t' = t + t_0 = c \cdot w$ is the *measured* time of flight, where t_0 , c and w are an intrinsic time offset, the channel number to

which a counted neutron is assigned to and the channel width (time/channel), respectively. t_0 is due to the unknown relation between the exact departure time of the neutron pulse and the starting time of the channel sequence. The monochromatization process is described by the Bragg condition $2d \sin \theta_B = n\lambda$. For the n -th order we write $v_n = L/t_n$ and so

$$v_1 = \frac{L}{t'_1 - t_0}, \quad v_2 = \frac{L}{t'_2 - t_0}$$

for $n = 1$ and $n = 2$. Moreover, for the first and second order (higher orders are negligible in this case, as can also be seen from the measured data) one knows that $\lambda_2 = \lambda_1/2$ and therefore $v_1 = v_2/2$. Taking advantage of this, one can get rid of the intrinsic time shift:

$$t_0 = 2t'_2 - t'_1$$

and can also calculate the real time of flight of a neutron pulse:

$$t = t' - t_0 = t' - 2t'_2 + t'_1.$$

The wavelength as a function of the measured time of flight and the wavelength as a function of the channel number c are then given by

$$\begin{aligned} \lambda(t') &= \frac{h}{m} \cdot \frac{t' - 2t'_2 + t'_1}{L} \\ \lambda(c) &= \frac{hw}{mL} (c - 2c_2 + c_1), \end{aligned}$$

with $c_{1,2}$, the channel numbers of the first and second order intensity peaks, respectively.

To calculate the spectral width or wavelength distribution $\Delta\lambda/\lambda$ one notes that in a TOF measurement the measured time uncertainty is, following the law of propagation of errors,

$$\Delta t'^2 = \Delta t_{CD}^2 + \Delta t^2.$$

It has two main contributions: First, the desired Δt that stems from the properties of the monochromator and second, Δt_{CD} which arises from the finite opening time or unstable rotation frequency of the chopper and the uncertainty of the exact position of detection within the detector. In the present measurements, the geometry and so the opening time of the chopper window is not known with high accuracy. Pencil-shaped ^3He detectors with a diameter of about 1 cm were used (see Section 2.6.1), so the uncertainty in the measurement of the distance between chopper and detector is more stringent

than the exact detection position. For two peaks of the *same* reflection order, obtained from two measurements at two different distances one can write:

$$\begin{aligned}\Delta t_1'^2 &= \Delta t_{CD}^2 + \Delta t_1^2 \\ \Delta t_2'^2 &= \Delta t_{CD}^2 + \Delta t_2^2\end{aligned}$$

and again, the unwanted part drops out if one assumes that it does not depend on the chopper-detector distance:

$$\Delta t_1'^2 - \Delta t_2'^2 = \Delta t_1^2 - \Delta t_2^2.$$

One can make the *Ansatz*

$$t = \text{const} \cdot \lambda.$$

and also gets $\Delta t = \text{const} \cdot \Delta \lambda$, which one can divide by the *Ansatz* to obtain $\Delta t/t = \Delta \lambda/\lambda$. This equation can be squared to be able to plug in $\Delta t_1'^2 - \Delta t_2'^2$. One finally yields

$$\frac{\Delta \lambda}{\lambda} = \sqrt{\frac{\Delta t_1'^2 - \Delta t_2'^2}{t_1^2 - t_2^2}}.$$

With $t = w \cdot c$ it follows that

$$\frac{\Delta \lambda}{\lambda} = \sqrt{\frac{\Delta c_1^2 - \Delta c_2^2}{c_1^2 - c_2^2}}.$$

One defines $\Delta c_{1,2}$ as the FWHM of the Gaussian peaks obtained in the first and second measurement at the positions marked by channel numbers c_1 and c_2 . They were determined from Gauss fits of measured data, applying the following fit function from the IGOR data analysis software:

$$f(x) = y_0 + A \exp \left[- \left(\frac{x - x_0}{\text{width}} \right)^2 \right].$$

It is related to the common form of the Gaussian distribution function

$$\bar{f}(x) = \frac{1}{\sigma \sqrt{2\pi}} \exp \left[- \frac{(x - x_0)^2}{2\sigma^2} \right]$$

by the equations $\sigma = \text{width}/\sqrt{2}$ and $\text{FWHM} = 2\sqrt{\ln 2} \cdot \text{width}$. The result of the TOF measurement at the beamline used for the subsequent experiments was:

$$\begin{aligned}\lambda &= 1.988(6)\text{\AA} \\ \frac{\Delta \lambda}{\lambda} &= 1.48(9)\%,\end{aligned}$$

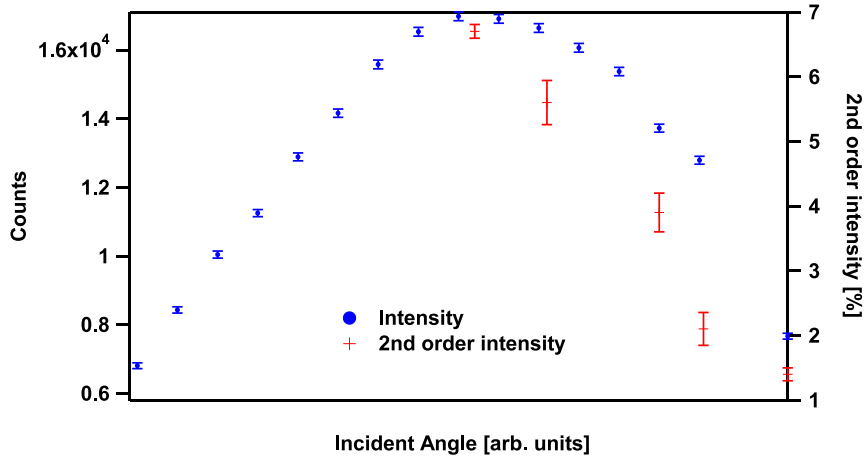


Figure 2.7: Blue markers: Intensity versus micrometer screw position. Red markers: Fractions of areas below second and first order Gaussian peaks versus incident angle.

which corresponds to a velocity of about 1989(5) m/s. It is not fully clarified, whether one should measure the chopper-detector distance from the center, the upstream or the downstream end of the chopper. Here, it was measured from the center, but additionally the systematic error arising from this potential mistake was taken into account. The percentage of second order neutrons in the beam was determined to 13.9(8)%, with only the polarizer in the beam.

2.6.3 Reducing Second-Order Intensity

In [Klepp 2004, Klepp *et al.* 2005] it is stated that the attempts to measure the Pancharatnam phase for mixed input states met its major difficulties in the second order neutrons reflected from the monochromator. When intensity oscillations were measured over more than one period, mutually different values were found for the two minima and the two maxima, which are expected to have roughly the same intensity. This poses a serious problem for the calculation of phases from minimum and maximum intensities. Because their interaction time with the magnetic fields along the beam path is only half of that for first order neutrons, their polarization is only rotated by half the angle that was adjusted for spin rotation devices.

The method to reduce the percentage of second order contributions is contained in the specifications of typical polarizing supermirrors: The critical

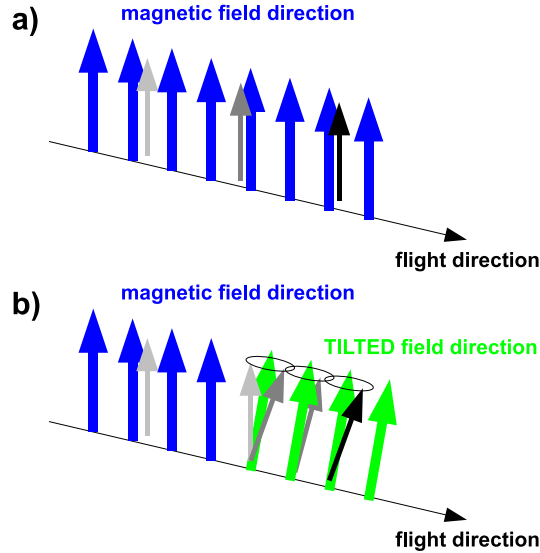


Figure 2.8: Neutrons with spin up move along the beam trajectory: a) All magnetic guide fields are perfectly aligned. The spin is kept parallel to the field direction. b) The second guide field is slightly tilted relative to the first one. The neutron spin starts a precession around the tilted direction.

angle θ_c between a neutron beam and a surface, under which the neutrons are total reflected by a material (see [Rauch and Werner 2000]), is larger for wavelength λ than for $\lambda/2$. This means that for given wavelength we can increase the angle of incidence slightly and certainly lose a certain amount of the first order neutrons, but the intensity of the second order neutrons decreases more rapidly.

In order to show this effect, several TOF measurements were carried out for varying analyzing supermirror angles. The adjustment of the micrometer screw that controls the relative position of the analyzer exit diaphragm with respect to the maximum intensity position was varied. The results are shown in Fig. 2.7. One could trade off measurement times longer by a factor of 2 or 3 for second order reduction down to about 1%. The maximum intensity of the complete setup and a 0.75 cm^2 Cd diaphragm in place was about 150 cts/s, which was good enough for the planned experiment. Second order intensity turned out to be not the only reason for unbalanced oscillations as will be explained in the next Sections.

2.6.4 Nonadiabatic Transitions between Guide Fields

During the adjustments for the mixed-state phase measurement it was conceived that even small tilting of the incident polarization vector relative to the magnetic guide field axis can also lead to asymmetric behavior of measured intensity oscillations. So, further effort was made to avoid such unwanted tilting of some degrees that can, in our setup, only be created by *nonadiabatic* evolutions. Without all rotation devices switched off, this means "unsmooth" transitions from some magnetic guide field to the next. Adiabatic evolution means, roughly speaking, that the spin state remains in an eigenstate of the Hamiltonian describing the magnetic interactions of the neutron beam along its trajectory. In such a case, the polarization vector remains pinned to the direction of the guide field (see Fig. 2.8a)). A quantitative criteria for adiabaticity, the adiabaticity parameter as given in [Kraan *et al.* 2003], can be written as:

$$k = \frac{\omega_L}{\omega_{geo}} = \frac{\frac{2\mu B}{\hbar}}{v \left| \frac{d\alpha}{dy} \right|},$$

where α is the angle between the intended guide field direction and the actual field direction at any position y along the beam trajectory. Adiabaticity is provided if k is large. If the field component in some other direction than $+z$ (remember that directions are defined as in Fig. 2.3) abruptly increases from zero, the polarization is not any more aligned to the guide field B_z , but precesses on a cone with an opening (tilting) angle around the new quantization axis (see Fig. 2.8b)). A simple experiment to resolve such a tilting is carried out: With polarizer and analyzer in place, one puts a DC coil with its magnetic field axis pointing to the x direction to a chosen position and varies its current. Say, we set currents in such a way that we achieve more than a $-\pi$ rotation up to more than a $+\pi$ rotation. $-\pi$ and π rotations are identified by the corresponding intensity minima. We obtain an intensity oscillation.

When doing a sine fit of the oscillation, its phase fit parameter "phi" in the IGOR fit function

$$f(x) = y0 + A \sin(fx + \text{phi}) \quad (2.40)$$

is equal to $\pi/2$ if the oscillation is perfectly symmetric. In practice, the oscillation can be shifted by several degrees. The approach was, to use phi as a quantitative measure of the tilting of the polarization vector incident to the coil the coil (or of the coil itself, see the next Sections). One moves the coil further along the beam by several mm (an increment small enough

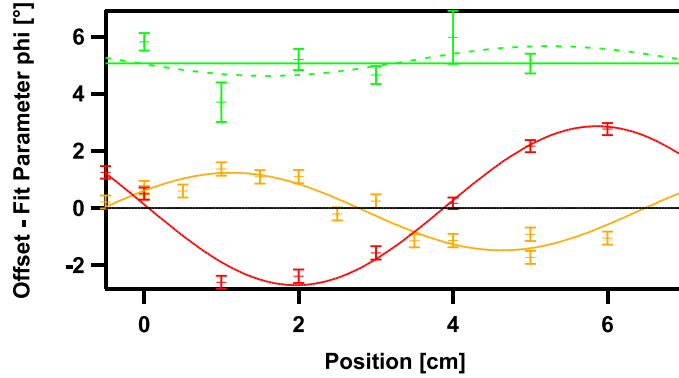


Figure 2.9: Three examples for measuring the tilting angle of the incident polarization.

to resolve one Larmor period within the guide field) and measures another oscillation by variation of the coil current. Repeating this procedure several times we can plot the fit parameter ϕ of each oscillation versus the coil position and obtain an oscillation whose amplitude is proportional to the angle between the guide field axis and the tilted incident polarization. A cross check for the obtained modulation is, that its period should roughly be equal to the Larmor period for the particular guide field strength. In the present case, it was about 10 G, corresponding to a Larmor period of about 6.8 cm. Deviations of the Larmor period in the experiments were explained as arising from stray fields from the neighboring beamline, situated at 5 - 50 cm distance, and the inaccurate positioning system: With a pen, positions were marked on the rails that carry the coils. Three examples of data obtained by the explained procedure are shown in Fig. 2.9. For the red curve the calculated tilting angle is about 3° , the Larmor period calculated from the fit parameter f is approximately 7 cm. For the orange curve the tilting angle is about 1.4° , the Larmor period calculated from the fit is roughly 7.8 cm. Both oscillations are offset from 0 by approximately 0.1° , where 0 means that $\phi = \pi/2$. They are obtained from measurements done at different relative distances of an auxiliary permanent magnet guide field to the guide field coils in which the used DC coil was placed. The green curve is data obtained for almost ideal incident polarization at the best position of the magnet. Here, a sine fitting model is not appropriate (green dashed line). A horizontal line fit with zero slope gives an offset of about 5° .

Very small tilting angles could be achieved with the guide field that is shown in Fig. 2.10. The "crocodile mouths" at the entrance and the exit provide for

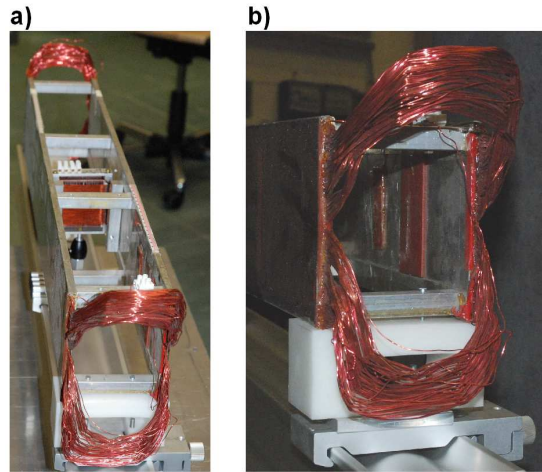


Figure 2.10: Guide field with "Crocodile mouths" at entrance and exit.

a good adiabatic transition of the polarization between the guide field and the surrounding auxiliary magnets. While most guide fields are designed to fulfill the conditions of Helmholtz geometry (the radius of the *two* coils equals their distance in field direction, see [Klepp *et al.* 2005], [Sponar *et al.* 2008a] and [Filipp *et al.* 2009] for examples), this guide field consists of only one coil.

The offset of the parameter ϕ , that does not depend on the coil position was interpreted as arising from a tilting of the used coil itself. Once the adjustment was accomplished such that there was no visible oscillation of the incident spin, one could compensate the tilting of a particular coil as will be described in Section 2.6.6.

2.6.5 DC Coils

For the experiments described in [Klepp 2004] and [Klepp *et al.* 2005], mainly the coils shown in Fig. 2.11 were used. Their dimensions are $h = w \sim 5$ cm in height and width and $l \sim 2.5$ cm in length. They were suspected to cause a very small homogeneous field region in their center, where the beam of circularly shaped cross-section of about 0.5 cm radius is transmitted.

Therefore, new coils were constructed that still fit into most available guide fields, but have bigger homogeneous field region in their center (see Fig. 2.12). In particular, the goal was to reduce the ratio of length to height and length to width. The dimensions are $h = w \sim 6$ cm and $l \sim 1.7$ cm. The preferred wire material was anodized Al, as it was used for the old coils. The absorption

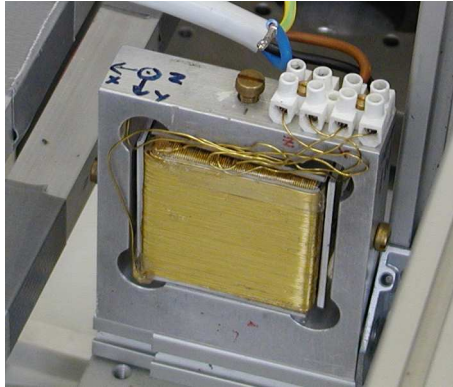


Figure 2.11: Coils used in earlier experiments. The wire material is anodized Al.

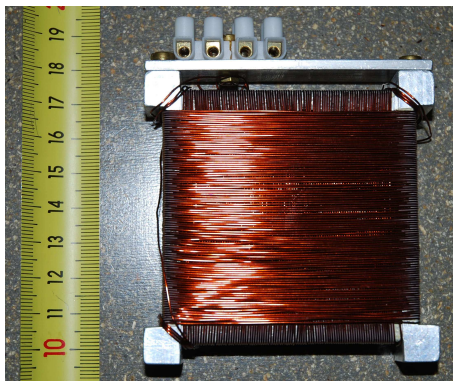


Figure 2.12: Coil designed to provide for better homogeneity in the coil center.

of neutrons by Al is very small. The thin insulating layer contains hydrogen that causes scattering. Within the course of coil design it was found that purchasing *a few* meters of anodized Al wire of about 0.6 mm diameter is not a trivial mission at all, since it is hard to find and most companies do not sell small entities.

Available Al-wire samples were tested in USANS measurements at the TRIGA reactor facility of the Atominstitut. The results were promising also with respect to an implementation of DC coils in interferometers, where the material in the beam path must not cause small angle scattering: The rocking curves with and without sample were identical (see Fig. 2.13). Unfortunately, *after* the USANS test it was found that the insulating layer of the wire was

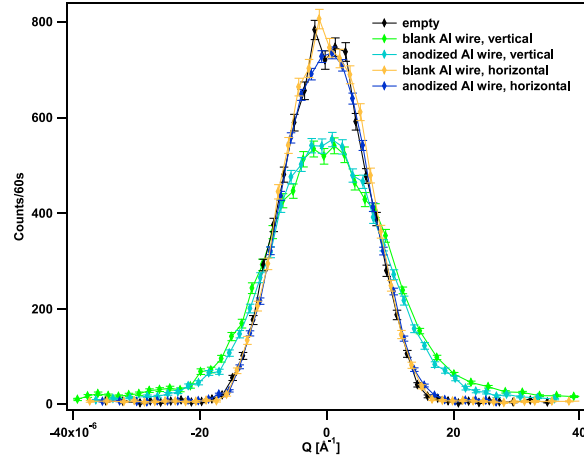


Figure 2.13: USANS measurements to test wire samples for DC coils. "horizontal" means that in the sample roughly parallel wire pieces are aligned perpendicular to the analyzing direction. Note that there is no difference between the blank and the anodized sample, which means that there is no small angle scattering involved. The material could in principle be used in interferometry experiments.

partly too thin to prevent shortcuts and so the samples were not suitable for DC coils. As a consequence of the anodized Al wire scarcity, we changed to coated Cu as wire material. The reduction of intensity for one coil with winding in x and z direction is about 18%.

2.6.6 Adjusting DC Coils

In this Section, it is explained how the fit parameter ϕ (see Eq. (2.40)) of a fit to an oscillation, measured by varying the x current of a DC coil, can be used to adjust the relative angle between the z axis of the coil and the incident polarization in case of unwanted tilting. We assume that the polarization is already adjusted to be parallel to the guide field. A behavior as exhibited by the green curve in Fig. 2.9 has already been shown. The only problem we are left with is the constant offset seen in this curve.

So, sweeping carelessly aside for the moment any other possible interpretation, position-independent shifting of the oscillation is solely attributed to tilting of the coil. Tilting around the x axis has been shown not to lead to crucial effects. One can neglect it as long as it is not visible to the naked eye. An oscillation measured using a coil tilted around an axis parallel to the

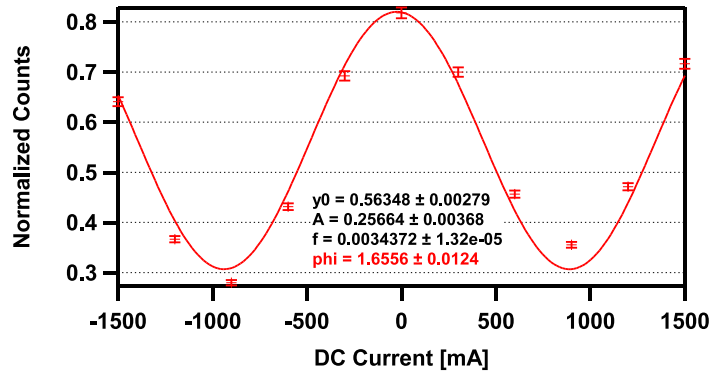


Figure 2.14: One obtains a shifted ($\sim 5^\circ$) and asymmetric curve when the x field current of a tilted DC coil is varied. Here, no guide field compensation was applied.

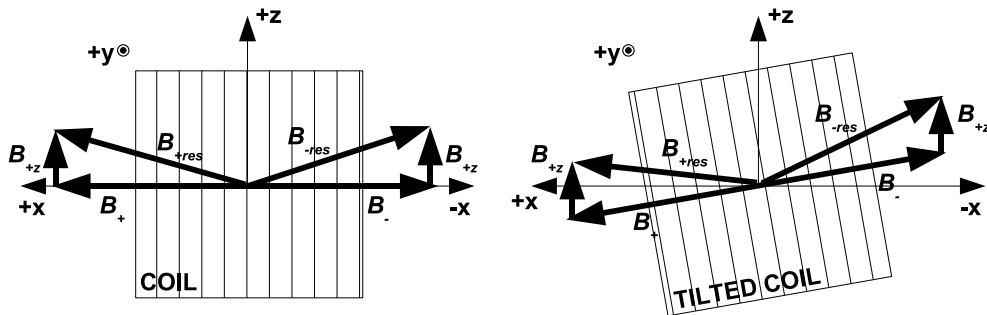


Figure 2.15: Visualization of coil tilting: The coil fields and the guide field are added and result in effective magnetic fields. The effective fields differ in magnitude and in angle enclosed with the z axis if the coil is tilted.

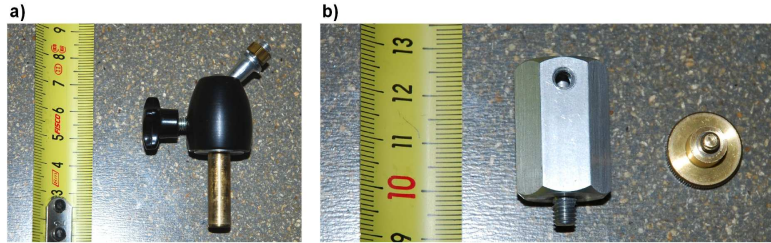


Figure 2.16: a) Camera joint for adjusting angles of mounted coils around the x and y axes. b) Al piece for the base rod of the joint to be inserted and fixed in a certain height by friction of the brass screw on the base rod.

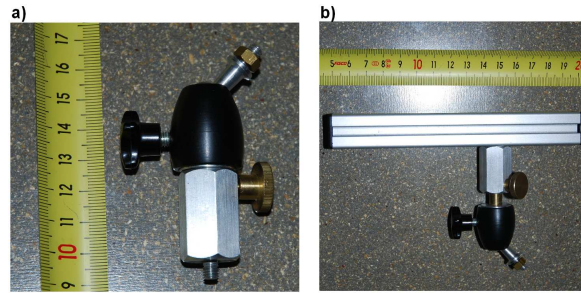


Figure 2.17: a) Joint with Al piece and fixation screw. b) Mounted on piece of ITEM rod.

flight direction (y in our case) typically looks like the one shown in Fig. 2.14. Note that the two minima do not exhibit the same intensity. This can be interpreted as different angles of the magnetic field axes with respect to the z direction because of tilting of the coil as shown in Fig. 2.15. By mounting the coil on a device able to compensate this tilting angle, an oscillation with roughly equal minima and zero offset, i. e. $\phi = \pi/2$, can be achieved. Since more professional materials like angle compensators were not available for first tests, cheap joints usually used for adjusting photo cameras on tripods (see Fig. 2.16a) were suggested and implemented by P. Pataki.

They are small enough for the task and have two degrees of freedom, namely rotation around the x and the y axis. The adjustment in height and the angle around z could be accounted for by a hexagonally shaped Al piece in which the base rod of the joint was inserted (see Figs. 2.16b and 2.17a).

By fixing a brass screw that holds the base rod and therefore the coil in a certain height and a certain angle around z by friction, all needed adjustments could be done. The disadvantage of this devices was the bad reproducibility.

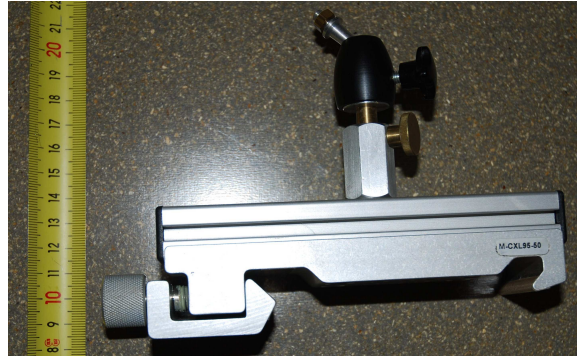


Figure 2.18: Complete adjustment device mounted on X 95 carrier.

The Al piece is mounted on an ITEM rod as shown in Fig. 2.17b. The rod

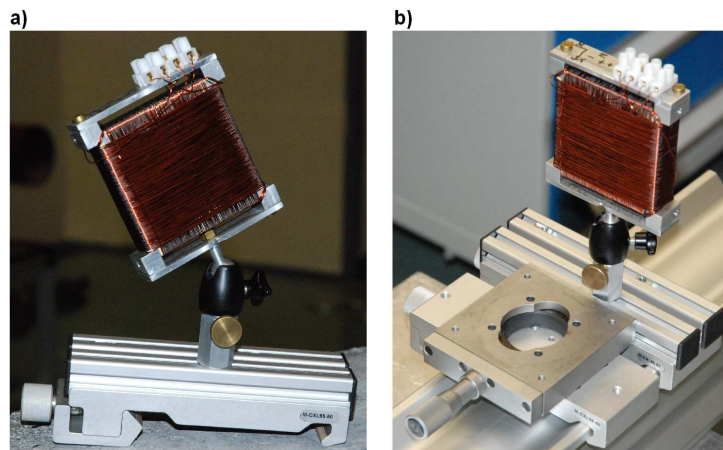


Figure 2.19: a) Coil on adjustment device. b) Adjusted coil and positioning system fixed to X 95 rail.

was fixed on a translation carrier (Fig. 2.18) for the used Newport X 95 rail profiles (see Fig. 2.19). The new version (2008) of the coil adjustment system is shown in Fig. 2.20 (see [Schmitzer 2009]).

On a second carrier, a manual linear translation table with a micrometer screw was mounted to be able to reproduce the position of the coil carrier: One fixes the coil carrier at a certain position and moves the translation table carrier so that the translation table touches firmly the coil carrier. After fixing the translation table carrier and loosening the coil carrier the micrometer screw can be adjusted to the desired relative distance and the

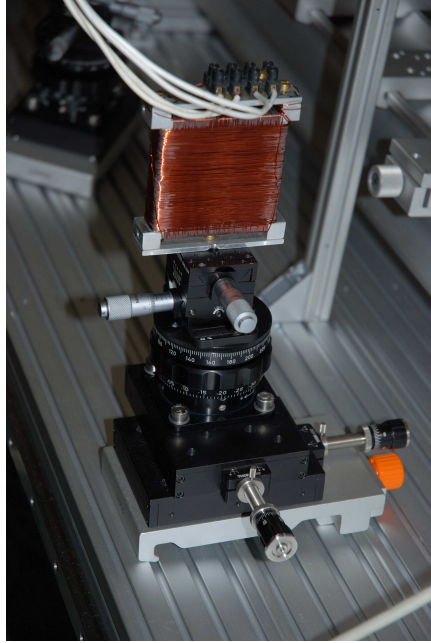


Figure 2.20: DC coil mounted on X 95 carrier with two translation stages for x and y direction, rotation table and angle compensators for both directions.

coil carrier is moved back to contact position. The coil carrier can then be fixed again and one knows the relative coil position with an accuracy of, in principle, $1 \mu\text{m}$. The carriers can, by mistake, be slightly tilted around the z direction (even when strongly fixed) and all mountings have small slackness which decreases the resolution of the positioning system. After some experience, the accuracy of this positioning method was estimated to be 0.5 mm , a value that also entered as systematic error in the data analysis. The blue curve in Fig. 2.21 shows a typical result of adjusting the tilting angle around the y axis of a DC coil. These curves were measured before the reconstruction of the polarimeter beamline in 2008.

In the photographs of the DC coils (for instance Fig. 2.12) one can see clearly that, apart from the winding causing the x field, there is a second layer of wire, wound around the z direction. This is already implemented in the old coils in Fig. 2.11 and is used to compensate the guide field at the position of the coil. Without compensation field, the guide field and the x component of the coil add up to a field that cannot become perpendicular to the z direction and therefore the incident up spin cannot be inverted to the down state in the coil (see Fig. 2.15). We found the correct values for the guide field compensation by choosing the current value that corresponds to one

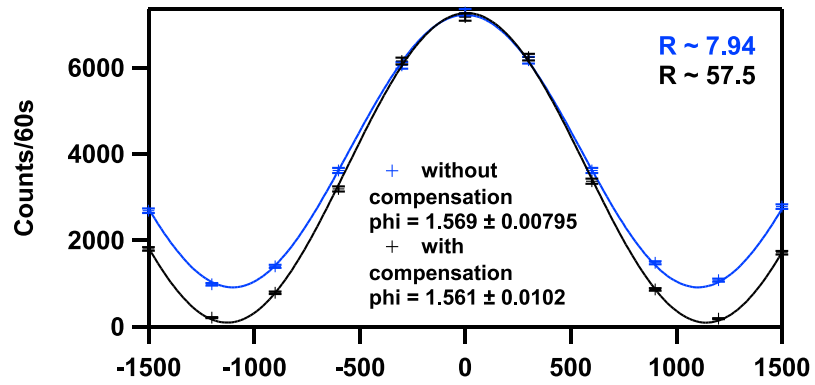


Figure 2.21: Blue curve: Oscillation measured after tilting adjustment, without compensation field at a guide field of about 10 G. Black curve: The same with compensation field. The flipping ratio (calculated from the fit) improves significantly on using a compensation field.

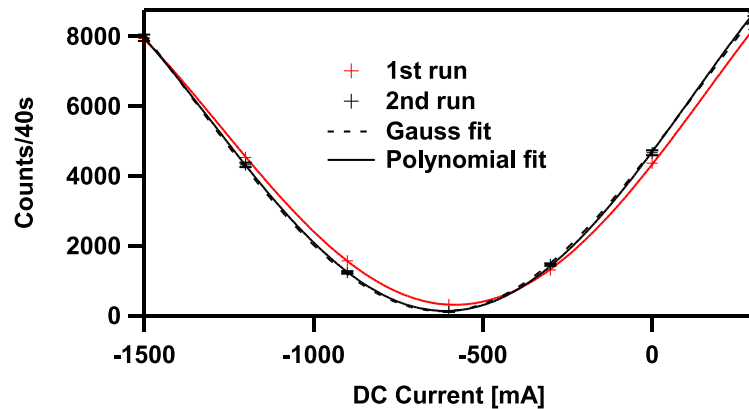


Figure 2.22: Red curve: First compensation field scan. Black curve: Second compensation field scan.

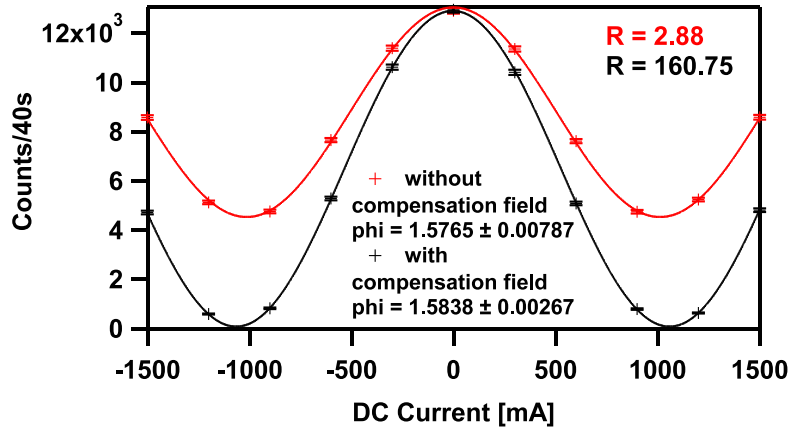


Figure 2.23: Red curve: After tilting adjustment, without compensation field at a guide field of about 12 G. Black curve: The same with compensation field. Note the huge difference in flipping ratio. The curves were measured at the refurbished polarimeter setup in autumn 2008.

of the minima in the blue fit curve of Fig. 2.21 for the x field. With this x -current set, the current for the z field is varied. The minimum intensity current of such a plot – the red curve shown in Fig. 2.22, for instance – is set and another x field variation is done. As a result, the flipping ratio $R = I_{max}/I_{min}$ increases significantly as well as the period of the measured oscillation. The latter is clearly seen from the black curves of Figs. 2.21 and 2.23. For the data associated to the black markers in Fig. 2.22 two fits were applied: One is a Gaussian (dashed line). The other is a polynomial of fifth degree (solid black line). The polynomial takes into account that the behavior of the compensation field scans is not symmetric around the minimum. However, if the current is varied only within a small range, no asymmetry can be observed.

Another effect that we found was, that after adding a compensation field to a coil whose tilting angle had been adjusted before, small tilting of 1°-2° is again observable. The coil with the compensation field switched on has to be adjusted once again. The origin of this effect could be that the pitch of the coil windings ($\leq 3^\circ$) in x and z direction prevent their fields to be mutually perpendicular. The whole procedure can be shortened by setting a good estimation for the compensation field from the beginning. The typical current values for a π rotation at a neutron velocity of about 2000 m/s and a guide field of 10 G were roughly 1.2 A and -0.3 A for x and z field, respectively.

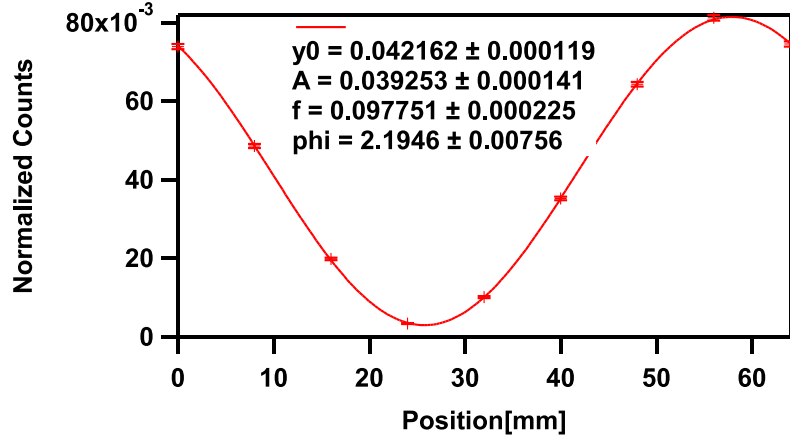


Figure 2.24: Varying the position of the second coil with both coils set to a $\pi/2$ rotation, we obtain an oscillation from which we can deduce and set the rotation angle of the polarization vector between the two coils.

2.6.7 How to set Distance with polarized Neutrons

In the experiment to measure mixed-state phases, it is required to set distances between different coils that correspond to the particular polarization rotation angles $2\pi n$, $2\pi n'$ and 2δ . This was done by the following method: The first of a pair of coils was set to a rotation of $\pi/2$ around the x axis. The incident up spin state evolves as it was described in Section 2.4.1 and becomes

$$|\psi\rangle = 1/\sqrt{2}(|+\rangle - i|-\rangle). \quad (2.41)$$

The polarization vector for this spin state is $\vec{r} = (0, -1, 0)^T$. The relative phase shift $\pm\Lambda/2$ between the spin eigenstates, induced within B_z , is described by the operator in Eq. (2.30). $\Lambda(y) = 2\mu B y / \hbar v$ depends upon the flight distance of the neutrons within B_z . The spin state becomes

$$|\psi\rangle = 1/\sqrt{2}(e^{-i\Lambda(y)/2}|+\rangle - ie^{i\Lambda(y)/2}|-\rangle). \quad (2.42)$$

The corresponding polarization vector is $\vec{r} = (\sin \Lambda(y), \cos \Lambda(y), 0)^T$. The polarization vector lies within the xy plane with its direction specified by Λ , depending on the distance from the first coil. After interaction with the x field of the second coil, also set to a $\pi/2$ rotation around the $+x$ axis, the final spin state is denoted as:

$$|\psi\rangle = \frac{1}{2}[e^{-i\Lambda/2}(|+\rangle - i|-\rangle) - ie^{i\Lambda/2}(-i|+\rangle + |-\rangle)]$$

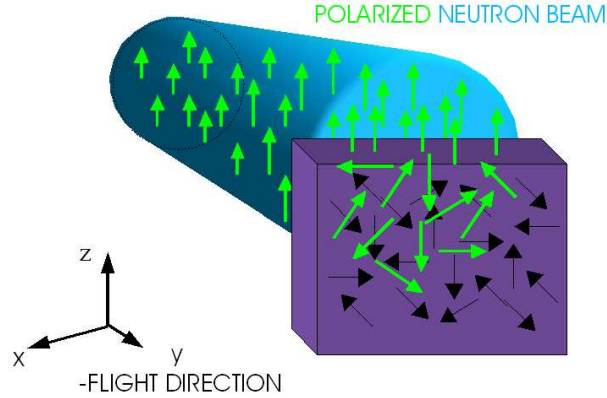


Figure 2.25: Adjusting the purity with a shim plate.

and the intensity after projection to the up state is

$$\begin{aligned}
 I &\propto |\langle +|\psi\rangle|^2 = \frac{1}{4}|e^{-i\Lambda/2} - e^{i\Lambda/2}|^2 \\
 &= \frac{1}{4}|-2i \sin \frac{\Lambda}{2}|^2 = \sin^2 \frac{\Lambda(y)}{2}.
 \end{aligned} \tag{2.43}$$

We know, for instance, that a minimum of intensity is found for $\Lambda/2 = 2\pi n$, so we can achieve any desired rotation angle or phase shift between two coils. An example for such a position measurement is shown in Fig. 2.24. As in Section 2.6.4, the period of the oscillation should roughly match the Larmor period of the guide field strength.

2.6.8 Creation of the Mixed State

To access Eq. (2.35) experimentally, r'_0 needs to be varied. Several ideas were developed and tested to achieve this in the experiment. In the following, a short explanation of all of them is given and the tests are summarized. First, a thin de-magnetized ferromagnetic material ("shim plate") of size $60 \times 30 \times 0.5 \text{ mm}^3$ was partly brought into the beam cross-section as shown in Fig. 2.6.8. Because of the randomly distributed magnetic domain directions, the part of the beam that is transmitted through the material is completely depolarized. It suffers from random polarization rotations. The part that passes the material on the side should stay completely polarized. The resulting beam should be a mixture of a polarized beam and a completely unpolarized beam. The first test measurement showed the desired loss of contrast, but the curve with inserted shim was also shifted by more than

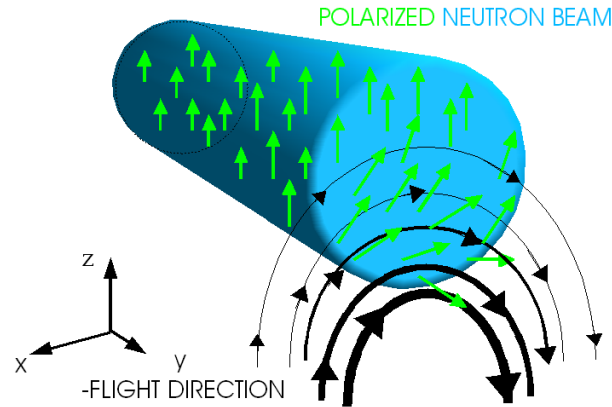


Figure 2.26: A particular purity can also be achieved by applying a magnetic field gradient parallel to the incident spin direction. For instance, a wire carrying high currents could be aligned parallel to the flight direction to create the indicated field gradient.

20° . This was interpreted as creation of unwanted magnetic field lines in directions other than $+z$ within the guide field around the shim. After this short test no further efforts were made to implement this method.

Second, a wire carrying current was considered for depolarizing the neutron beam by its stray field as is shown in Fig. 2.6.8. However, the high currents needed prevented this suggestion from being tested.

The third method that was tested was called RF-mixing method. Due to the rotating wave approximation [Sakurai 1994], there is *one* magnetic field axis that rotates within the xy plane in an RF flipper (see, for instance, [Suda 2006] or [Sponar 2009] for more detailed descriptions of RF flippers in neutron optics). A beam, polarized in $+z$ direction, passes the field of an RF coil (see Fig. 2.6.8). With the flipper adjusted to a π rotation, each neutron arriving at the coil at different instants, experiences the spin flip around an axis that lies in the xy plane. The directions of those axes are equally distributed around 2π for arriving particles. Since all polarization vector tips finally point to the same direction ($-z$) for a π rotation, the system remains in a pure state that is $|-\rangle$. If we set an amplitude to achieve a rotation angle *between* 0 and π the situation is different. In this case, all resulting polarization vector tips should be equally distributed around some circle of latitude of the Bloch sphere. Averaging over a long measurement time interval – compared to the RF frequency of some 10 kHz – should yield a mixed state. By this method, one should be able to create any desired purity ranging from a pure state to the completely mixed state only by setting RF

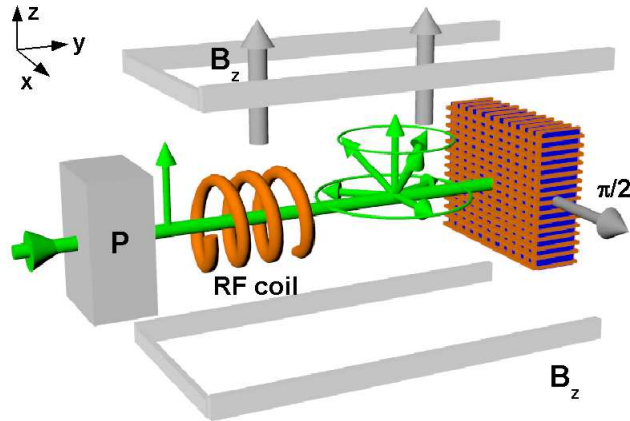


Figure 2.27: The RF-mixing method.

amplitudes corresponding to rotation angles between 0 and $\pi/2$, respectively. However, tests showed that some small components of the polarization direction other than $+z$ remain for unknown reasons. The issue could not be fully clarified. Moreover, it was found that the electronic parts of the RF circuit (resistor, capacitor, amplifier) must be chosen very carefully to achieve well matched circuits and therefore stable magnetic field amplitudes within the RF coil. As an example, the change of the flipping ratio $R = I_{off}/I_{on}$ is plotted versus time in Fig. 2.6.8. The saturation behavior in this plot, measured directly after switching on the signal generator is unfortunately not the end of the story: Drastic changes of flipping ratios in the coils were noted also after continuous operation of several hours, apparently depending also on environment temperature. As a consequence, in subsequent interferometer experiments on GHZ-states at the S18 in Grenoble using RF Flippers, PC controlled amplitude readjustment was implemented to ensure stability. Later, new amplifiers (EPS) were available, providing for very stable amplitudes. Finally, this mixing method was discarded as the two others before.

The method that finally saved the day was to use the first DC coil in the setup for generating the mixed spin state (see Fig. 2.29). In addition to the current which results in the transformation U_1 (the $\pi/2$ rotation to create the superposition state), random noise from a SONY/TEKTRONIX AFG320 signal generator was applied to the first coil, thereby changing B_x in time. The voltage signal from the noise as recorded by a digital oscilloscope is shown without and with coil and amplifier (KEPCO power supply) connected to the circuit in Fig. 2.30a and b, respectively. The noise created a small unwanted amplitude-dependent offset in addition to the DC current intended to im-

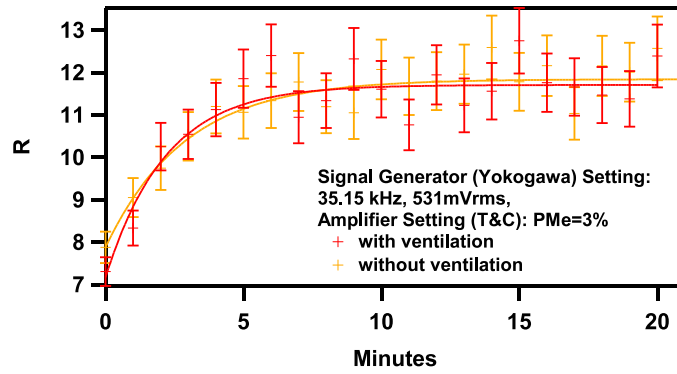


Figure 2.28: The flipping ratio R versus time measured immediately after switching on the signal generator. With two fans as used for cooling of PC housings, the effect of cooling of the circuit parts was tested. Fan cooling was found to have no effect.

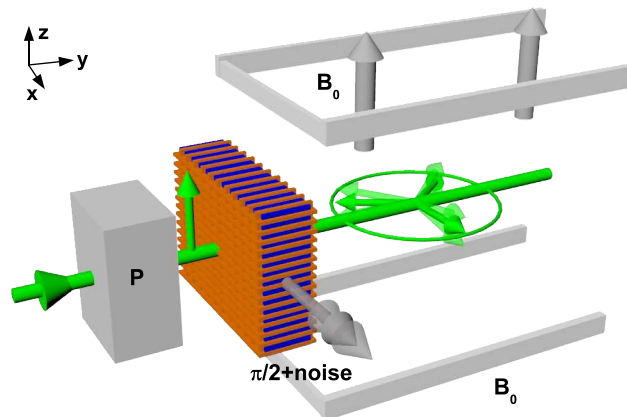


Figure 2.29: Generation of mixed states by the use of the first DC coil and a function generator.

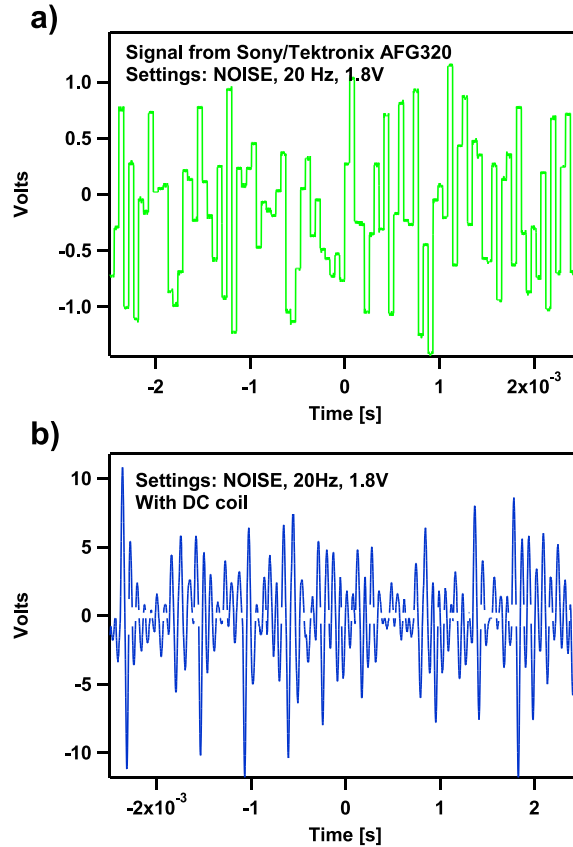


Figure 2.30: a) Voltage signal from the NOISE function of the signal generator. The changing rate of the amplitude is about 20 kHz. b) Signal measured with coil and amplifier connected to the circuit.

pose the $\pi/2$ rotation. It could be measured by a multimeter (AC current measurement) and compensated with a counter-directed offset, adjusted at the signal generator. From Fig. 2.30b, it can be seen that the resulting signal is not merely a smoothed version of the signal in Fig. 2.30a. The inductance of the coil and the characteristics of the power supply are assumed to be responsible for the signal form. The signal generator settings for the four noise levels (the pure state phase was measured with the signal output switched off) were:

1. Function: NOISE, Frequency: 20 Hz, Amplitude: 1.8 V, Offset: 10 mV
2. Function: NOISE, Frequency: 20 Hz, Amplitude: 2.4 V, Offset: 15 mV
3. Function: NOISE, Frequency: 20 Hz, Amplitude: 3.8 V, Offset: 25 mV

4. Function: NOISE, Frequency: 20 Hz, Amplitude: 6.15 V, Offset: 40 mV

Note that these values are display readings.

Neutrons, which are part of the ensemble $\rho_{in}(r'_0)$, arrive at different times at the coil and experience different magnetic field strengths. This is equivalent to applying different unitary operators $U(\pi/4+\Delta\xi'(t), 0, -\pi/2) = \tilde{U}_1(\Delta\xi'(t))$. For the whole ensemble we have to take the time integral

$$\rho = \int \tilde{U}_1(\Delta\xi'(t))|+\rangle\langle+|\tilde{U}_1^\dagger(\Delta\xi'(t))dt. \quad (2.44)$$

Although each separate transformation is unitary, due to the randomness of the signal we end up with a nonunitary evolution that yields a mixed state for the measurement time at each position of the second coil [Bertlmann *et al.* 2006]. Note that in this method the purity r'_0 of the input state is not affected before the first DC coil. In this coil \tilde{U}_1 is set to create spin superpositions distributed around $|\psi_0\rangle$ within the y, z plane. We are left with $\vec{r}_0 = (0, -r_0, 0)$ where $r_0 < 1$, as has been confirmed by analyzing the state $\tilde{U}_1\rho_{in}\tilde{U}_1^\dagger$. The x and z components of \vec{r}_0 were found to be negligible.

2.6.9 Measuring the Purity

In [Buchelt 1997], several methods are described to determine the degree of polarization (the length of the polarization vector) or purity of the spin state. Here, we will shortly explain the method used in the mixed-state phase measurement, which is referred to as "Two-Flipper Method". It requires two spin flippers that turn the polarization of the neutron beam through an angle of π , from the up state to the down state with respect to the guide field and the analyzing direction of polarizer and analyzer. By performing measurements of the four intensities

I_1intensity with both flippers turned off
 I_2intensity with flipper 1 (efficiency= e_1) turned on
 I_3intensity with flipper 2 (efficiency= e_2) turned on
 I_4intensity with both flippers turned on,

(see Fig. 2.31) one can calculate the unknown quantities e_1, e_2 and r^2 as

$$\begin{aligned} e_1 &= \frac{I_4 - I_2}{I_1 - I_3} \\ e_2 &= \frac{I_4 - I_3}{I_1 - I_2} \\ r^2 &= \frac{(I_1 - I_2) \cdot (I_1 - I_3)}{I_1 I_4 - I_2 I_3} \end{aligned} \quad (2.45)$$

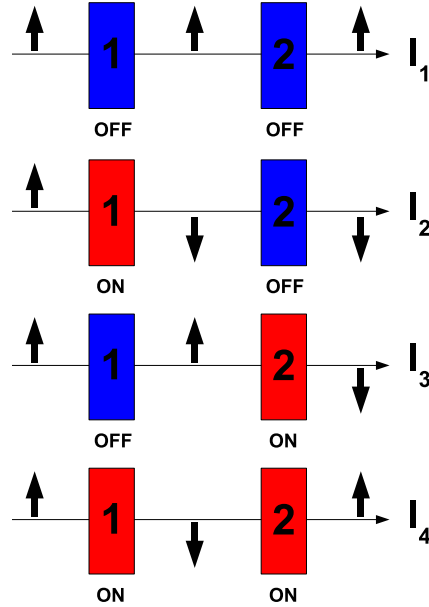


Figure 2.31: Two-Flipper Method.

In the derivation of Eq. (2.45) it was assumed that the polarizer and the analyzer have the same characteristics concerning transmission and spin filtering, so $r_P \approx r_A \equiv r$. Therefore one has r^2 in Eq. (2.45). The assumption is that the purity of the beam leaving the polarizer, r_P , is only diminished by the noise added to the DC current in the coil winding for B_x of the first coil and can be described by a depolarization factor d . One can denote r^2 from Eq. (2.45) as $r^2 = r_P \cdot d \cdot r_A$. Since one can calculate the right hand side of Eq. (2.45) from measured intensities, one can determine $r_P \cdot d$: With the noise switched off it follows that $d = 1$ and one measures $r_P \cdot r_A$ in that case. Then, $\sqrt{r_P \cdot r_A} = r_A$ since one still assumes $r_P \approx r_A$. The thereby determined value for r_A can be used to calculate $r_P \cdot d$ for all other noise amplitudes. Rough values of the purity, obtained with the chosen noise settings given in Section 2.6.8, were 99%, 75%, 61%, 33% and 11% for 0 V, 1.8 V, 2.4 V, 3.8 V and 6.15 V of signal amplitude, respectively. More accurate values are given in the data plots of Section 2.7. The purities were measured before each experimental run and differed slightly on different days for otherwise unchanged settings. The deviations were roughly up to three standard deviations.

Although Eq. (2.45) is independent of the flip-efficiency, spin flippers used for the explained method need to be well-adjusted, because a bad flipper

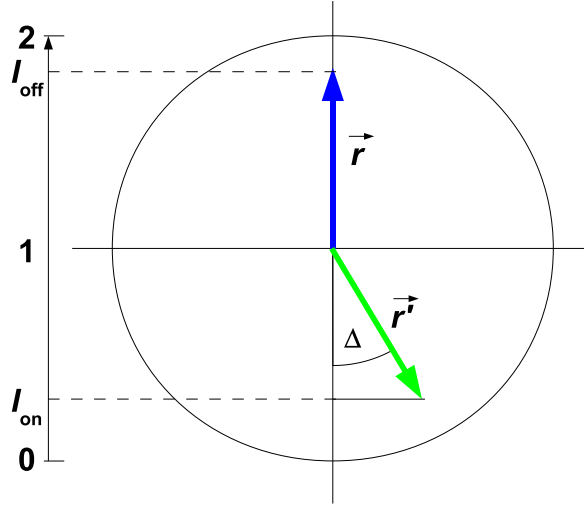


Figure 2.32: Scheme of an incomplete spin flip. \vec{r} and \vec{r}' are polarization vectors with flipper switched off and on, respectively. For simplicity, the intensity is normalized so that it ranges from 0 to 2.

(although it does not depolarize the beam) rotates the polarization through some angle $\neq \pi$ and/or around some axis not intended by the experimenter. Consider the following example: Let \vec{r} and \vec{r}' be the polarization vectors before and after an incomplete flip that is assumed not to cause any shortening of the polarization vector, i. e. $r = r'$ (no depolarization). Before the flip \vec{r} points in $+z$ direction. After the operation, the polarization vector encloses an angle Δ with the vertical axis parallel to the analyzing direction of polarizer and analyzer (see Fig. 2.32). The flipping ratio is $R = I_{off}/I_{on}$, so that we may write

$$I_{on} = \frac{I_{off}}{R} = \frac{1+r}{R}.$$

For the angle Δ we get

$$\cos \Delta = \frac{1 - I_{on}}{r'} = \frac{1 - \frac{1+r}{R}}{r'}$$

and since $r = r'$ we have

$$\Delta = \arccos \left(\frac{1}{r} - \frac{1}{R} - \frac{1}{Rr} \right). \quad (2.46)$$

Suppose we measure the flipping ratio $R = 50$, which is a reasonably good result (the maximum value measured within the scope of this experiment was

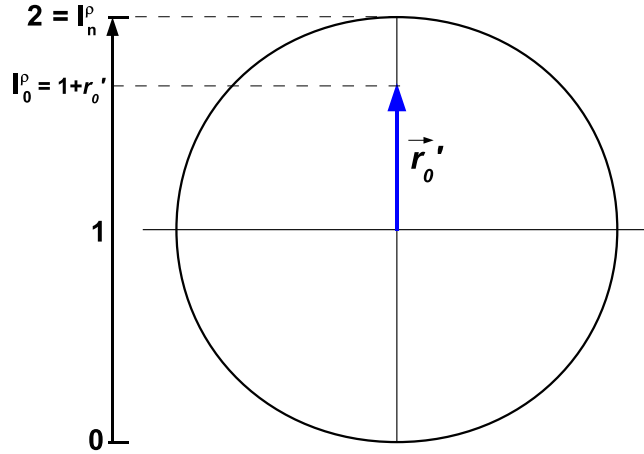


Figure 2.33: A hypothetical measurement of the intensity at input purity $r'_0 = 1$ and $U_\phi = \mathbb{1}$ would yield I_n^ρ as a result. However, we only can measure I_0^ρ and r'_0 to calculate I_n^ρ .

~ 68). It follows from Eq. (2.46) that for $r \sim 1$ we still get $\Delta \sim 16^\circ$. So even when we reach high flipping ratios, care has to be taken not to produce any oscillations in the sense of Section 2.6.4. If one uses such flippers in a purity measurement, the result for the intensity I_4 , for instance, may depend on the distance of the two coils. In the experiments described here, the distance between the second and the third coil is a measurement parameter that has to be varied. It is not the same for all measurements, so the purity could differ for the same noise settings.

2.6.10 Normalization of Intensities

To yield the mixed-state phase and visibility from a particular measured curve, the values for I_{min}^ρ and I_{max}^ρ obtained from a fit must be normalized by the intensity I_n^ρ to plug them into Eqs. (2.33) and (2.34). I_n^ρ is the intensity that *would* reach the detector after passing the empty setup ($U_\phi = \hat{\mathbb{1}}$) at an input purity of $r'_0 \equiv 1$, a situation that is not achievable in practice. I_n^ρ cannot be measured, but only calculated as

$$I_n^\rho = 2I_0^\rho / (1 + r'_0), \quad (2.47)$$

where I_0^ρ must be measured for each r'_0 . Equation 2.47 can be understood from Fig. 2.33: I_0^ρ is the intensity at $U_\phi = \hat{\mathbb{1}}$ with a specific value of input purity. Consider, for example, the two extreme cases: If $r'_0 = 1$, Eq. (2.47)

becomes $I_n^\rho = I_0^\rho$, which means that we can only obtain $I_{max}^\rho/I_n^\rho \leq 1$, as required. If $r'_0 = 0$, we get $I_0^\rho = I_n^\rho/2$, which is the correct result for a completely unpolarized beam. However, note that Eqs. (2.33) and (2.34) are undefined for $r'_0 = 0$. This issue is also discussed in [Bhandari 2002] and [Anandan *et al.* 2002].

2.7 Experimental Results

The methods described in the previous Sections were implemented to carry out the mixed-state phase measurement as explained in the following. Here, the obtained data is shown. Data analysis is explained and the results are discussed in the following.

2.7.1 Purity-Dependence of the Phase

The neutron beam incident from the pyrolytic graphite crystal monochromator with mean wavelength and spectral width as described in Section 2.6.2 was polarized up to $r'_0 \sim 99\%$ by reflection from a bent Co-Ti supermirror array. The implementation of these devices is explained in [Buchelt 1997]. The analyzing supermirror was slightly de-adjusted to higher incident angles to suppress second order intensity in the incident beam as described in Section 2.6.3. The final maximum intensity I_0 was about 150 cts/s at a beam cross-section of roughly 0.75 cm^2 (with a circle-shaped Cd diaphragm of $\sim 0.5 \text{ cm}$ radius pinned to the analyzer entrance). In order to find the coil current values for required polarization rotation angles, each coil current was adjusted as explained in Section 2.6.6. Then, with coils set to a $\pi/2$ rotation around the x axis, inter-coil distances were varied to search for intensity minima. Thereby, the desired rotation angles within the guide field were adjusted pairwise, as described in Section 2.6.7. As explained in Section 2.4.1, one can choose the parameters ξ by setting the current in the second coil to achieve a rotation angle 2ξ and the parameter δ by adding a certain flight distance within B_z to the distance $2\pi n' \hbar v / 2\mu B$ set between the second and the third coil. The corresponding rotation angle is 2δ . With the first coil and the third coil set to a $\pi/2$ and $-\pi/2$ rotation, respectively, the intensity in the detector recorded in a certain time interval (depending on the achieved intensity and the magnitude of the statistical error one can tolerate) were measured. The typical measurement time interval was 120 s. Then, the second coil was moved one step further by the positioning system described in Section 2.6.6 and the intensity measured again. Continuing this procedure and plotting the measured intensity versus the coil position one

obtained a graph like the black curves in Fig. 2.34, for instance. Then the signal generator was switched on to add the noise to the DC current as explained in Section 2.6.8. For settings No. 1, for example, one obtains the blue curves of Fig. 2.34 with a purity of the input state of about 77%. In the same manner intensity oscillations for the remaining three input purities were recorded. Additionally, the purity was measured before each run. As an approximation the intensity I_4 was associated to I_0^p (see Section 2.6.9 and Section 2.6.10). The validity of this approximation was also confirmed experimentally for one noise level.

In total, for purely geometric phases the parameter sets ($\xi = \pi/4$, δ , $\zeta = \delta - \pi/2$) with $\delta = \phi_g = \pi/8, 2\pi/8$ and $3\pi/8$ were chosen. For each set the intensity oscillations I^p – see Fig. 2.34 – were measured. The error bars in those plots are calculated taking into account the law of propagation of errors for the normalized intensity calculated by $I_{\text{detector}}/I_{\text{monitor}}$. In Fig. 2.35, the purely geometric mixed-state phase $\Phi_g(r_0)$ and the visibility $\mathcal{V}_g(r_0)$, calculated from the data in Fig. 2.34 by the use of Eqs. (2.33) and (2.34) are shown. For this purpose IGOR sine fits (see also Eq. (2.40)), represented by the solid lines in Fig. 2.34, were applied. The fitting procedure provides for the parameters of the calculated function and its uncertainties (standard deviation σ). The errors for the minima and maxima were associated with the error of the amplitude parameter A . The result of Eqs. (2.33) and (2.34) are an angle in radiant – the phase, and a dimensionless number between 0 and 1 – the visibility. In order to get to these results, one had to normalize the obtained minima and maxima of each fit function to be able to use them for the calculation of phase and visibility. This is explained in Section 2.6.10. The law of propagation of errors was applied to all error-prone quantities to calculate the vertical error bars for phases and visibilities shown in the graphs. Furthermore, only visible at two data points in Fig. 2.35, horizontal error bars were calculated. They correspond to the uncertainty in the purity at which a certain phase was measured. However, they are rather small compared to other influences like, for example, the error in reproducing the coil position, which is the main source of error in the experiment and was eliminated by implementing stepper motors in later experiments. As already stated, this error of estimated 0.5 mm was accounted for in the data analysis. The solid lines in Fig. 2.35 are theoretical curves according to Eqs. (2.35), using the measured value for Φ without noise as phase reference.

The purely dynamical phase requires that $2\xi = 0$ and therefore Eq. (2.32) reduces to

$$I^p = (1 - r'_0)/2 + r'_0 \cos^2 \delta.$$

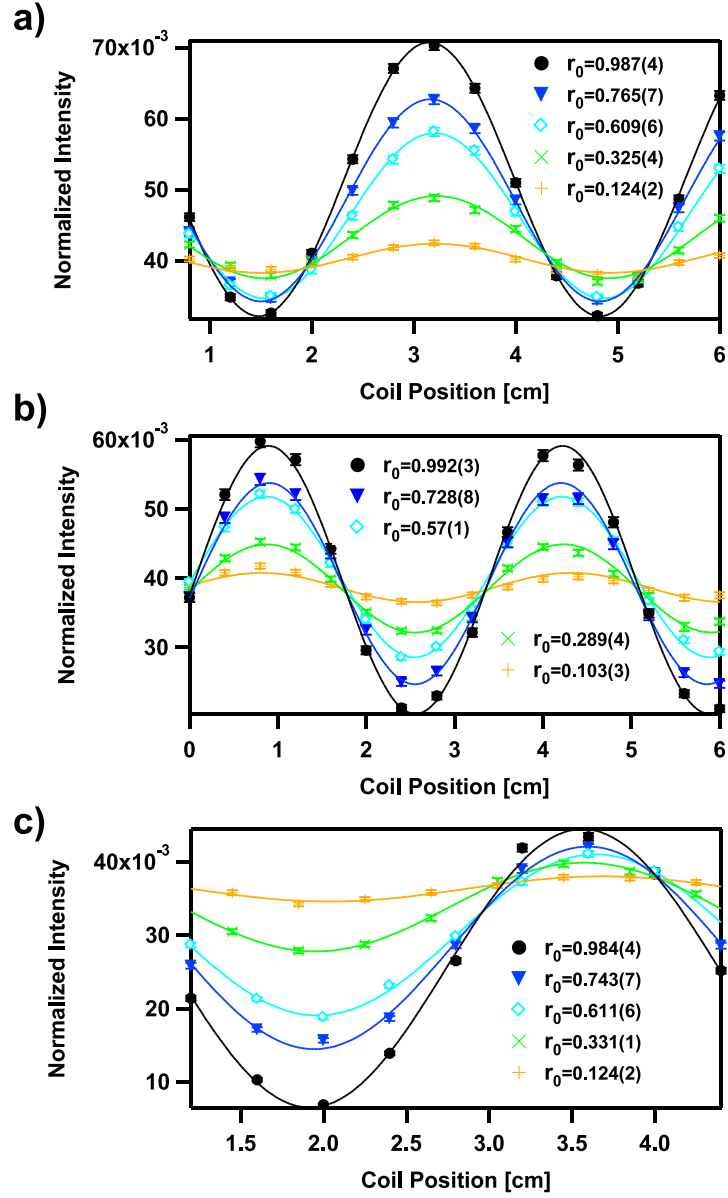


Figure 2.34: Intensity oscillations measured for varying positions of the second coil and five different input purities. The parameter settings for the purely geometric phase were $\xi = \pi/4$ and: a) $\delta = \pi/8$, b) $\delta = 2\pi/8$ and c) $\delta = 3\pi/8$.

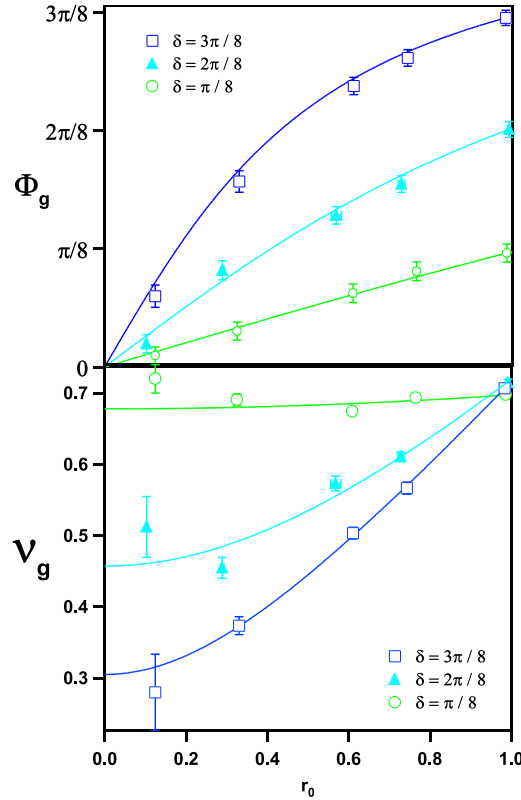


Figure 2.35: Purely geometric phases and the corresponding visibilities versus input purity for three values of δ .

As a consequence, only one intensity value is needed to compute Φ_d . With the second coil turned off, the distance between the first and the third coil was chosen such that the polarization rotation angle between them was $2\pi n'' + 2\delta$. Intensity oscillations for the parameter values $\delta = \phi_d = \pi/8, 2\pi/8, 3\pi/8$ for five values of r_0 , shown together with fits (solid lines) in Fig. 2.36, were recorded. The dynamical mixed state phases $\Phi_d(r_0)$ and the visibility $\mathcal{V}_d(r_0)$ were calculated in the same manner as their geometric counterparts, explained in the previous paragraph and are shown in Fig. 2.37.

The experimental data reproduce the r_0 -dependence predicted by Eq. (2.35). Clearly, there is no difference in the behavior of dynamical and geometric mixed-state phase visible from the data. This is no surprise, since all derivations in the first part of this chapter are done for the Pancharatnam phase, which can be either dynamical or geometric or a combination of both.

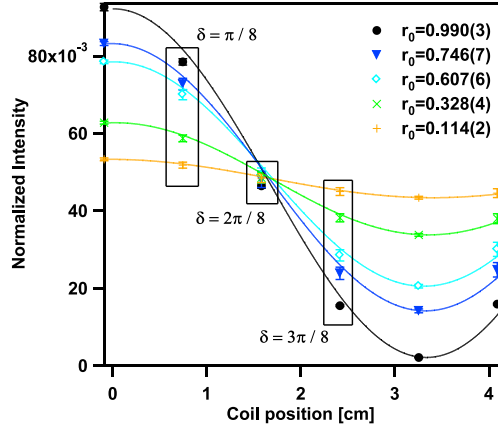


Figure 2.36: Measured oscillations for purely dynamical phases.

2.7.2 Nonadditivity

The carried out experiments include also a special property of the mixed-state phase: its nonadditivity. Since this phase is defined as a weighted average of phase factors rather than one of phases (see Eq. (2.9) or [Singh *et al.* 2003, Fu and Chen 2004a, Sjöqvist 2004, Fu and Chen 2004b] for a more elaborate discussion), it is true only for pure states that phases of separate measurements can be added up to the usual total phase. Suppose we carry out two measurements on a pure state system: The state is subjected to a transformation U_g in the first and to a different transformation U_d in the second experiment, inducing the pure state phases ϕ_g and ϕ_d , respectively. Applying Eqs. (2.28) and (2.29), we can also choose a combination of angles 2ξ and 2δ leading to a transformation U_{tot} so that we measure the total pure state phase $\phi_{tot} = \phi_g + \phi_d$. It is expected from quantum theory that phases in interference experiments behave exactly in the same manner. However, the result of the latter experiment for the system in a mixed input state is $\Phi_{tot}(r_0) = \arctan[r_0 \tan(\phi_g + \phi_d)]$. The total phase is then *not* given by $\Phi_g(r_0) + \Phi_d(r_0)$, with $\Phi_g(r_0) = \arctan(r_0 \tan \phi_g)$ and $\Phi_d(r_0) = \arctan(r_0 \tan \phi_d)$. Although this result is in complete agreement with theory – we can expect nonadditivity from Eq. (2.9) already – it is surprising and in contradiction with what is the case for pure states. It is worth noting that the three evolution paths on the Bloch sphere, induced by U_g , U_d and U_{tot} , differ from each other, i. e. in each of the three experiments the spin state traces out different paths on the Bloch sphere (see also Section 2.8). In our experiment we have chosen two examples of U_{tot} , i.e. two sets of values

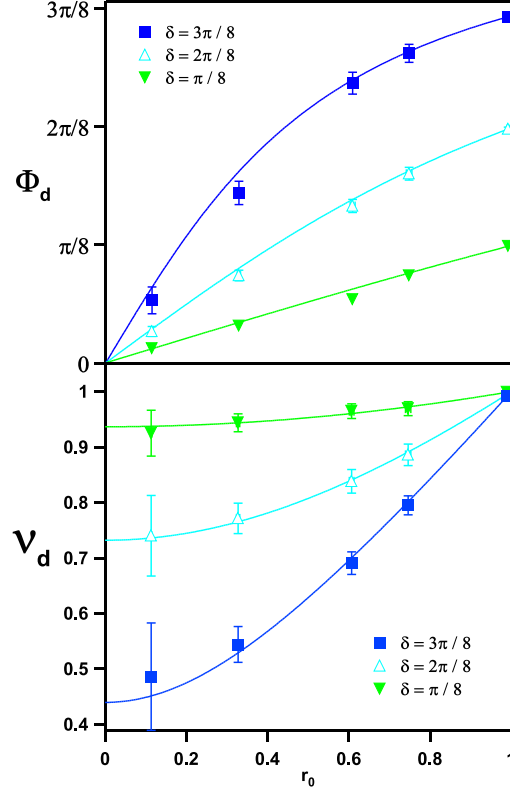


Figure 2.37: Purely dynamical phases and the corresponding visibilities versus input purity for three values of δ .

for B_x in the second coil and the distance within B_z to show that additivity does not hold for mixed-state phases: $2\xi^{(1)} = 60^\circ$, $2\delta^{(1)} = 90^\circ$ and $2\xi^{(2)} = 48^\circ$, $2\delta^{(2)} = 135^\circ$. The sets were chosen that way to be able to compare the results with the calculated sum of dynamical and geometric phases already shown in Section 2.7. According to Eqs. (2.28) and (2.29), the total pure state phases $\phi_g^{(1)} + \phi_d^{(1)}$ and $\phi_g^{(2)} + \phi_d^{(2)}$ with $\phi_g^{(1)} = \phi_g^{(2)} = \pi/8$ and $\phi_d^{(1,2)} = 2\pi/8, \pi/8$ should be obtained. The intensity oscillations, again measured by recording the intensity at various positions of the second coil, are shown for five values of input purities in Fig. 2.38a and b for set (1) and (2), respectively. In Fig. 2.39 the resulting mixed state phases $\Phi_{tot}^{(1,2)}$ and the sum $\Phi_g^{(1,2)} + \Phi_d^{(1,2)}$ are plotted. $\Phi_{tot}^{(1,2)}$ is directly obtained by plugging the normalized minima and maxima from the fit curves of Fig. 2.38 into Eq. (2.33), while the sums $\Phi_g^{(1,2)} + \Phi_d^{(1,2)}$ are calculated from the previously measured data shown in Figs. 2.35 and 2.37. The values of the terms in the sum are also indicated by the black

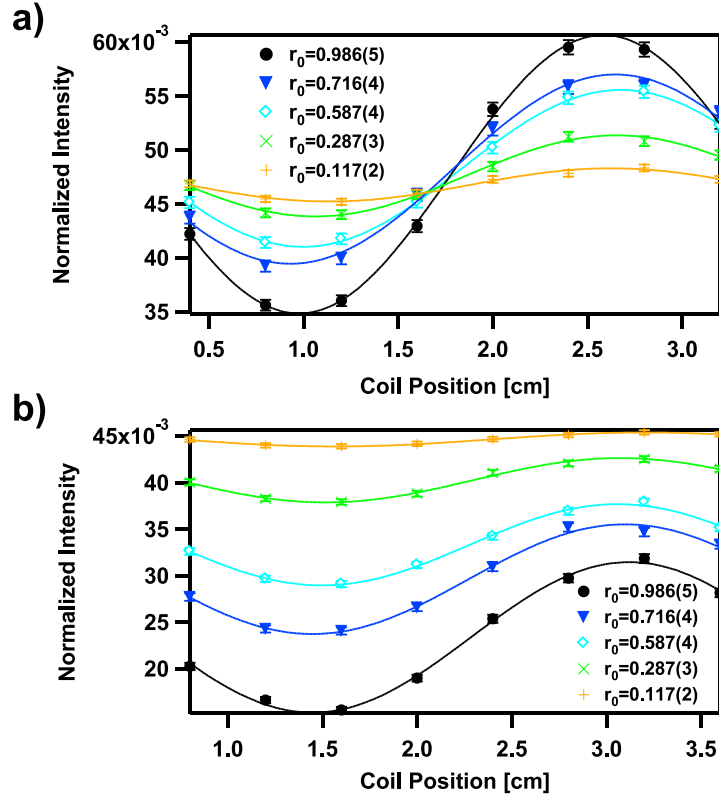


Figure 2.38: Intensity oscillation measured for the parameter sets: a) (1) that results in the pure state phase $\phi_g^{(1)} + \phi_d^{(1)} = \pi/8 + \pi/8$. b) (2) that results in the pure state phase $\phi_g^{(2)} + \phi_d^{(2)} = \pi/8 + 2\pi/8$.

and white bars in Fig. 2.39. The solid and the dotted lines are theory curves assuming nonadditivity and additivity, respectively. The experimental data is clearly in favor of nonadditivity, as expected from theory.

2.8 Discussion

Nonadditivity of the Sjöqvist mixed state phase is not expected from intuitive extrapolation of phase concepts from familiar pure state behavior. Since the purity of input states in real experiments is always smaller than 1, nonadditivity might be of great importance for possible applications of quantum phases with many-step gate operations. Our result is valid not only for a sum of geometric and dynamical phases - which is what we have shown here - but for summation of arbitrary phases and also an arbitrary number of terms.

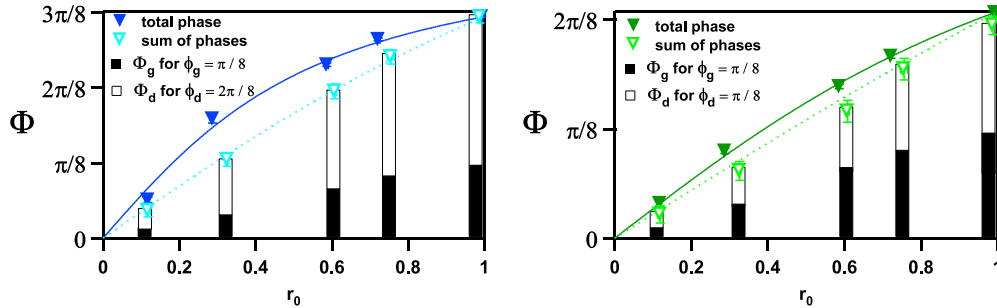


Figure 2.39: Filled triangles: Phases obtained from measuring oscillations from the parameter sets (1) (right) and (2) (left). Empty triangles: Sum calculated from previously measured purely dynamical and geometric phases as indicated by bars. The two data sets coincide only for the pure state (far right point in each plot).

This can be stated as

$$\Phi_{tot} = \arctan(r \tan \phi_{tot}) \neq \sum_n \Phi_n,$$

with $\phi_{tot} = \sum_n \phi_n$ and $\Phi_n = \arctan(r \tan \phi_n)$.

For the measurements to obtain the mixed-state phase for the combinations of geometric and dynamical transformations (Fig. 2.39), we chose two suitable sums of previously measured data of purely geometric and purely dynamical phases (Figs. 2.35 and 2.37). Using Eq. (2.28), we calculated the necessary evolution path (Γ_{tot}) to induce the corresponding total pure state phase $\phi_{tot} = \phi_g + \phi_d$ in one experimental run. Φ_{tot} is then measured for varied input purity r_0 (it is noted here that Γ_{tot} , Γ_d and Γ_g differ from each other). Assuming phase gates in some conceivable application, it means that the purity of the utilized quantum system has to be considered when inducing phases for further processing.

Note also that nonadditivity of mixed-state phases is not due to the non-linearity of the geometric phase that occurs, for instance, when the system evolves close to the orthogonal state of the reference state [Bhandari 1997]. The noncyclic geometric phase is minus half the solid angle enclosed by the path on the Bloch sphere and its shortest geodesic closure (see Section 2.2). As an example, we can consider two types of transformations and figure out what the corresponding geometric phase is: First, let the state $|+\rangle$ be rotated by an angle $\pi - \epsilon$ to transform to $a|+\rangle + b|-\rangle$. If ϵ is very small, the probability amplitude a is close to zero. The shortest geometric closure of this path

is the direct way back on the path itself and therefore the solid angle Ω and the geometric phase are zero. Second, let $|+\rangle$ be rotated by $\pi + \epsilon$. By doing the small step further than π , the shortest geodesic way back to $|+\rangle$ closes the path on the *opposite* side of the Bloch sphere. Therefore, the geometric phase suddenly jumps from zero to $-\pi$ at $\epsilon = 0$.

As already stated, the evolution paths for each ϕ_n are, in our experiments, different from each other. The question was raised, whether it is possible to demonstrate nonadditivity in an experiment where only *one* evolution path is needed, i. e. to conduct an experiment that can directly determine the portions of geometric and dynamical phases separately, implementing one and the same evolution path (in this context, note that Eq. (2.35) does not contain the parameter ξ , the portions of phases are not expressed in the phase-purity dependence). While this does not seem to be the case for the experiments in [Du *et al.* 2003, Ericsson *et al.* 2005] it might, for instance, be possible for adiabatic and cyclic evolutions, i. e. measurements of the Berry phase. In that case a spin echo approach can be used to get rid of dynamical phase contributions (e. g. [Jones *et al.* 2000, Bertlmann *et al.* 2004, Leek *et al.* 2007, Filipp *et al.* 2009]). In such a scheme for a two-level system one has to carry out an adiabatic and cyclic evolution (Γ_C) that induces a relative phase, followed by a π -flip of the two shifted eigenstates. Subsequently, Γ_C is implemented once again, but in reversed direction. While the resulting geometric phase induced by the evolution doubles, because it depends on the directed solid angle as seen from the origin of the Bloch sphere (Eq. (2.10)), all dynamical phase shifts cancel out. By skipping the π -flip and the second implementation of Γ_C , we can get the total phase. We can then calculate the amount of dynamical phase involved by subtracting the geometric phase obtained in the first experiment. Alternatively, we may skip the π -flip and reverse the second implementation of Γ_C . The geometric phase cancels, while the dynamical phase doubles. These methods are also applied in an experiment with ultra-cold neutrons, measuring the dependence of the variance of the Berry phase on the evolution time [Filipp *et al.* 2009].

One may ask if these three procedures really constitute separate measurements of geometric, dynamical and total phase arising from the same evolution path Γ_C . For instance, one could include the π -flip and the subsequent application of the inverse of Γ_C into what is considered to be the actual evolution path and call it Γ'_C . Then, applying the three procedures is equivalent to adjusting the angles 2ξ and 2δ in three different ways as in the experiment explained in this Chapter, because also here, several transformations different from Γ'_C are applied to yield the desired phases. If it is thus concluded that the answer to the above question is "no", this infers that the only phase that we can measure is the total phase. Whether it contains

solely a geometric or a dynamical component or is a combination of both, is simply a question of the evolution path involved. From this point of view, the portion of geometric and dynamical phase can not be resolved by a single experiment. Furthermore, it suggests that nonadditivity could only be shown by implementing different, mutually exclusive, evolution paths $\Gamma_1, \Gamma_2, \dots, \Gamma_n$ and Γ_{tot} .

On the other hand, if one leaves aside the π -flip and the reversed excursion on Γ_C and considers the three procedures as implementation of one and the same evolution, as it is usually done, the situation is different. We can then resolve the portions of phases and consequently also demonstrate nonadditivity implementing only one single evolution path.

Recently there has been a report on NMR experiments [Du *et al.* 2007] investigating Uhlmann's mixed state geometric phase. It is a property of a composite system undergoing a certain non-local evolution of system and ancilla [Ericsson *et al.* 2003a]. Diverse phase definitions, depending on this evolution, are possible. The phase investigated in the present work is a special case in which the ancilla does not necessarily evolve. While the preconditions for inherent fault tolerance [Jones *et al.* 2000] remain intact for the Sjöqvist phase, the question whether other phases offer advantages in terms of robustness remains an exciting issue of discussion.

Chapter 3

Nonunitary Phases

Geometric phase and the geometric mixed state phase gave rise to a theory for phases for mixed states under nonunitary evolutions. Among others (see Chapter 1), it was put forward by [Tong *et al.* 2004]. The theoretical description of the nonunitary phase is based on a kinematic approach for the mixed-state phase as developed in [Singh *et al.* 2003].

In the following Sections, the most important steps of the derivation of the nonunitary geometric phase in [Tong *et al.* 2004] are explained. Furthermore, an experiment is described, that resolves the impact of noise on the spin evolution in a neutron polarimeter. Its results are shown and discussed.

3.1 Theory

A quantum system s which is described by state vectors in the N -dimensional Hilbert space \mathcal{H}_s undergoes an evolution on the path \mathcal{P} . The density matrix depends upon a chosen parameter t :

$$\mathcal{P} : t \in [0, \tau] \rightarrow \rho(t) = \sum_{k=1}^N \omega_k(t) |\phi_k(t)\rangle \langle \phi_k(t)|. \quad (3.1)$$

$\omega_k(t) \geq 0$ are the eigenvalues of $\rho(t)$ corresponding to the k -th eigenvector $|\phi_k(t)\rangle$. All nonzero eigenvalues are assumed to be non-degenerate. The degenerate case is treated in [Tong *et al.* 2004] and will not be considered here. The density matrix $\rho(t)$ is lifted to a pure state $|\Psi(t)\rangle \in \mathcal{H} = \mathcal{H}_s \otimes \mathcal{H}_a$ of the combined system $s+a$ with the entangled ancilla system a of dimension $K = N$ (in general, $K \geq N$ can be assumed). The purified state reads as

$$|\Psi(t)\rangle = \sum_{k=1}^N \sqrt{\omega_k(t)} |\phi_k(t)\rangle \otimes |a_k\rangle \quad (3.2)$$

and

$$\begin{aligned}
\rho(t) &= \text{Tr}_a(|\Psi(t)\rangle\langle\Psi(t)|) \\
&= \text{Tr}_a\left(\sum_{k,k'=1}^N \sqrt{\omega_k(t)\omega_{k'}(t)}|\phi_k(t)\rangle\langle\phi_{k'}(t)| \otimes |a_k\rangle\langle a_{k'}|\right) \\
&= \sum_{k,k'=1}^N |\phi_k(t)\rangle\langle\phi_{k'}(t)| \text{Tr}(\sqrt{\omega_k(t)\omega_{k'}(t)}|a_k\rangle\langle a_{k'}|) \\
&= \sum_{k,k'=1}^N |\phi_k(t)\rangle\langle\phi_{k'}(t)| \sum_i \sqrt{\omega_k(t)\omega_{k'}(t)}\langle i|a_k\rangle\langle a_{k'}|i\rangle \\
&= \sum_{k=1}^N |\phi_k(t)\rangle\langle\phi_k(t)|\omega_k(t)
\end{aligned}$$

is fulfilled. $\rho(t)$ is given by the partial trace over the ancilla. The Pancharatnam relative phase between $|\Psi(0)\rangle$ (the initial state) and $|\Psi(\tau)\rangle$ (the state after the evolution), is denoted as

$$\begin{aligned}
\alpha(\tau) &= \arg\langle\Psi(0)|\Psi(\tau)\rangle \\
&= \arg\left(\sum_{k=1}^N \sqrt{\omega_k(0)\omega_k(\tau)}\langle\phi_k(0)|\phi_k(\tau)\rangle\right). \tag{3.3}
\end{aligned}$$

Both, $|\phi_k(0)\rangle$ and $|\phi_k(t)\rangle$ are orthonormal bases of the same Hilbert space \mathcal{H}_s . The number of vectors $|\phi_k(0)\rangle$ is the same as the number of vectors $|\phi_k(t)\rangle$. Consequently, there exists a unitary operator $V(t)$ that transforms each $|\phi_k(0)\rangle$ to $|\phi_k(t)\rangle$:

$$|\phi_k(t)\rangle = V(t)|\phi_k(0)\rangle,$$

with

$$V(t) = |\phi_1(t)\rangle\langle\phi_1(0)| + \dots + |\phi_N(t)\rangle\langle\phi_N(0)|. \tag{3.4}$$

Equation (3.3) can then be rewritten as:

$$\alpha(\tau) = \arg\left(\sum_{k=1}^N \sqrt{\omega_k(0)\omega_k(\tau)}\langle\phi_k(0)|V(\tau)|\phi_k(0)\rangle\right). \tag{3.5}$$

A disadvantage of Eq. (3.5) is, that it depends on the chosen purification. If the evolution $V(t)$ fulfills the parallel transport condition $\langle\Psi(t)|\dot{\Psi}(t)\rangle = 0$, the

phase $\alpha(\tau)$ becomes the geometric phase for states of the entangled systems s and a . However, this condition is stringent only for *one* of the N phases of each of the pure state components of the mixed state. Therefore, to yield the mixed-state geometric phase resulting from the path \mathcal{P} , an equivalence set of unitary operators $\tilde{V}(t)$ of the form

$$\tilde{V}(t) = V(t) \sum_{k=1}^N e^{i\theta_k(t)} |\phi_k(0)\rangle \langle \phi_k(0)| \quad (3.6)$$

is introduced in [Tong *et al.* 2004]. $V(t)$ is arbitrary and $V(0) = \mathbb{1}$. The $\theta_k(t)$ are real and time-dependent with $\theta_k(0) = 0$. From the operators $\tilde{V}(t)$, one can choose the unitary operators $V^{\parallel}(t)$, that fulfill the parallel transport conditions

$$\langle \phi_k(0) | V^{\parallel\dagger}(t) \dot{V}^{\parallel}(t) | \phi_k(0) \rangle = 0. \quad (3.7)$$

By plugging Eq. (3.6) into Eq. (3.7), a condition for the $\theta_k(t)$ that provides for the k induced phases to be of purely geometric origin, can be extracted:

$$\begin{aligned} & \langle \phi_k(0) | \tilde{V}^{\dagger}(t) \dot{\tilde{V}}(t) | \phi_k(0) \rangle \\ &= \langle \phi_k(0) | \tilde{V}^{\dagger}(t) \dot{V}(t) e^{i\theta_k(t)} + \tilde{V}^{\dagger}(t) V(t) i \dot{\theta}_k(t) e^{i\theta_k(t)} | \phi_k(0) \rangle \\ &= \langle \phi_k(0) | V^{\dagger}(t) \underbrace{\sum_k \underbrace{e^{-i\theta_k(t)} e^{i\theta_k(t)}}_1}_{\mathbb{1}} | \phi_k(0) \rangle \langle \phi_k(0) | \dot{V}(t) | \phi_k(0) \rangle + i \dot{\theta}_k(t) = 0. \end{aligned}$$

This yields

$$\theta_k(t) = i \int_0^t \langle \phi_k(0) | V^{\dagger}(t') \dot{V}(t') | \phi_k(0) \rangle dt'. \quad (3.8)$$

Using this expression, one can substitute $V(\tau)$ in Eq. (3.5) by $\tilde{V}(t) = V^{\parallel}(t)$ to yield the geometric phase arising from the path \mathcal{P} :

$$\begin{aligned} \gamma[\mathcal{P}] &= \arg \left(\sum_{k=1}^N \sqrt{\omega_k(0)\omega_k(\tau)} \langle \phi_k(0) | V^{\parallel}(\tau) | \phi_k(0) \rangle \right) \\ &= \arg \left(\sum_{k=1}^N \sqrt{\omega_k(0)\omega_k(\tau)} \langle \phi_k(0) | V(\tau) e^{-\int_0^{\tau} \langle \phi_k(0) | V^{\dagger}(t) \dot{V}(t) | \phi_k(0) \rangle dt} | \phi_k(0) \rangle \right) \\ &= \arg \left(\sum_{k=1}^N \sqrt{\omega_k(0)\omega_k(\tau)} \langle \phi_k(0) | \phi_k(\tau) \rangle e^{-\int_0^{\tau} \langle \phi_k(t) | \dot{\phi}_k(t) \rangle dt} \right), \quad (3.9) \end{aligned}$$

where Eq. (3.4) has been used. This phase is gauge invariant and depends only upon the path traced out by $\rho(t)$. Furthermore, it reduces to the results in [Sjöqvist *et al.* 2000] and [Singh *et al.* 2003] for unitary transformations, where the eigenvalues ω_k are time independent and $V(t)$ is associated the time evolution operator of the state.

3.2 An Example

In [Tong *et al.* 2004] one finds a typical example for which the derived phase can be specified. A qubit under the influence of the spin precession Hamiltonian $H = (\eta/2)\sigma_z$, is subjected to dephasing that is represented by the Lindblad operator $\Gamma = \sqrt{(\Lambda/2)}\sigma_z$ [Lindblad 1976]. With $\mu B\sigma_z = \hbar/2 \cdot \omega_L\sigma_z$ and assuming that \hbar was set to 1 in H , one can see that η corresponds to the Larmor frequency ω_L . Λ is associated to the dephasing strength. The initial state is a pure state given by the Bloch vector $\vec{r}(0) = (\sin \theta_0, 0, \cos \theta_0)^T$. One can solve the master equation [ACKN 1]

$$\underbrace{\dot{\rho} = -i[H, \rho]}_{\text{Liouville-von Neumann Eq.}} + \underbrace{\sum_k (A_k \rho A_k^\dagger - \frac{1}{2} A_k^\dagger A_k \rho - \frac{1}{2} \rho A_k^\dagger A_k)}_{\text{nonunitary term}}. \quad (3.10)$$

The second term on the right hand side is also called the "dissipator", the operators A_k are the Lindblad operators or generators. For the example above, there is only one generator, so Eq. (3.10) becomes

$$\begin{aligned} \dot{\rho} &= -i[H, \rho] + \Gamma \rho \Gamma^\dagger - \frac{1}{2}(\Gamma^\dagger \Gamma \rho + \rho \Gamma^\dagger \Gamma) \\ &= -i(H\rho - \rho H) + \Gamma \rho \Gamma - \frac{1}{2}(\Gamma^2 \rho + \rho \Gamma^2) \end{aligned} \quad (3.11)$$

and in matrix representation one further obtains

$$\begin{aligned} \begin{pmatrix} \dot{\rho}_{00} & \dot{\rho}_{01} \\ \dot{\rho}_{10} & \dot{\rho}_{11} \end{pmatrix} &= i\eta \begin{pmatrix} 0 & -\rho_{01} \\ \rho_{10} & 0 \end{pmatrix} + \Lambda \begin{pmatrix} 0 & -\rho_{01} \\ -\rho_{10} & 0 \end{pmatrix} \\ &= \begin{pmatrix} 0 & (-i\eta - \Lambda)\rho_{01} \\ (i\eta - \Lambda)\rho_{10} & 0 \end{pmatrix}. \end{aligned} \quad (3.12)$$

Four differential equations must be solved to obtain the time evolution of the state. First, one has:

$$\begin{aligned} \rho_{00}^{\dot{}} &= 0, \quad \rho_{11}^{\dot{}} = 0 \\ \Rightarrow \rho_{00}(t) &= \rho_{00}(0), \quad \rho_{11}(t) = \rho_{11}(0). \end{aligned} \quad (3.13)$$

For the remaining two equations

$$\begin{aligned} \rho_{01}^{\dot{}} &= (-i\eta - \Lambda)\rho_{01}, \\ \rho_{10}^{\dot{}} &= (i\eta - \Lambda)\rho_{10} \end{aligned}$$

one can make the *Ansatz*

$$\begin{aligned} \rho_{01}(t) &= e^{(-i\eta - \Lambda)t} \rho_{01}(0), \\ \rho_{10}(t) &= e^{(i\eta - \Lambda)t} \rho_{10}(0). \end{aligned} \quad (3.14)$$

From the initial density matrix $\rho(0)$, that is calculated from $\vec{r}(0)$, one finds

$$\rho(t) = \begin{pmatrix} \cos^2 \frac{\theta_0}{2} & \frac{1}{2} e^{(-i\eta - \Lambda)t} \sin \theta_0 \\ \frac{1}{2} e^{(i\eta - \Lambda)t} \sin \theta_0 & \sin^2 \frac{\theta_0}{2} \end{pmatrix}. \quad (3.15)$$

By the help of MATHEMATICA one obtains the eigenvalues

$$\begin{aligned} \omega_{1,2} &= \frac{1}{4} (2 \pm 2\sqrt{1 + e^{-2\Lambda t} + (1 - e^{-2\Lambda t}) \cos 2\theta_0}) \\ &= \frac{1}{2} (1 \pm \sqrt{\cos^2 \theta_0 + e^{-2\Lambda t} \sin^2 \theta_0}). \end{aligned} \quad (3.16)$$

The unnormalized eigenvectors are

$$\begin{aligned} |\tilde{\phi}_{1,2}(t)\rangle &= e^{(-i\eta + \Lambda)t} \left(\cot \theta_0 \pm \frac{\csc \theta_0}{\sqrt{2}} \sqrt{1 + e^{-2\Lambda t} + (1 - e^{-2\Lambda t}) \cos 2\theta_0} \right) |+\rangle + |-\rangle \\ &= e^{(-i\eta + \Lambda)t} \left(\frac{\cos \theta_0}{\sin \theta_0} \pm \frac{1}{\sin \theta_0} \sqrt{\cos^2 \theta_0 + e^{-2\Lambda t} \sin^2 \theta_0} \right) |+\rangle + |-\rangle \\ &= e^{(-i\frac{\eta}{2} + \Lambda)t} \cot \theta_0 \\ &\quad \cdot \left[e^{-i\frac{\eta}{2}t} \left(1 \pm \frac{1}{\cos \theta_0} \sqrt{\cos^2 \theta_0 + e^{-2\Lambda t} \sin^2 \theta_0} \right) |+\rangle + e^{(i\frac{\eta}{2} - \Lambda)t} \frac{\sin \theta_0}{\cos \theta_0} |-\rangle \right] \\ &= e^{(-i\frac{\eta}{2} + \Lambda)t} \cot \theta_0 \\ &\quad \cdot \left[e^{-i\frac{\eta}{2}t} \left(1 \pm \sqrt{1 + e^{-2\Lambda t} \tan^2 \theta_0} \right) |+\rangle + e^{i\frac{\eta}{2}t} e^{-\Lambda t} \tan \theta_0 |-\rangle \right]. \end{aligned} \quad (3.17)$$

For further simplification,

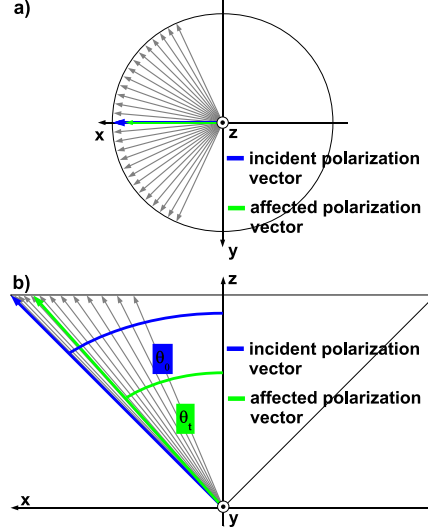


Figure 3.1: An example for the effect of noise in z direction on the polarization vector $\vec{r}(0)$: Uniformly distributed noise amplitudes create a distribution of vectors with a polar angle θ_0 . Averaging over all vectors leads to a shorter vector with polar angle $\theta_t < \theta_0$.

$$\tan \theta_t = e^{-\Lambda t} \tan \theta_0 \quad (3.18)$$

is defined. The stronger the noise, the smaller the angle θ_t , as can also be understood from Fig. 3.1. The eigenvectors become

$$|\tilde{\phi}_{1,2}(t)\rangle = e^{(-i\frac{\eta}{2} + \Lambda)t} \cot \theta_0 \cdot [e^{-i\frac{\eta}{2}t} (1 \pm \sqrt{1 + \tan^2 \theta_t}) |+\rangle + e^{i\frac{\eta}{2}t} \tan \theta_t |-\rangle] \quad (3.19)$$

and can further be rewritten as

$$|\tilde{\phi}_{1,2}(t)\rangle = e^{(-i\frac{\eta}{2} + \Lambda)t} \cot \theta_0 \cdot [e^{-i\frac{\eta}{2}t} (\cos \theta_t \pm 1) |+\rangle + e^{i\frac{\eta}{2}t} \sin \theta_t |-\rangle]. \quad (3.20)$$

One can calculate the normalized eigenvectors:

$$|\phi_1(t)\rangle = e^{-i\frac{\eta}{2}t} \cos \frac{\theta_t}{2} |+\rangle + e^{i\frac{\eta}{2}t} \sin \frac{\theta_t}{2} |-\rangle, \quad (3.21)$$

$$|\phi_2(t)\rangle = -e^{-i\frac{\eta}{2}t} \sin \frac{\theta_t}{2} |+\rangle + e^{i\frac{\eta}{2}t} \cos \frac{\theta_t}{2} |-\rangle. \quad (3.22)$$

Plugging in Eqs. (3.16), (3.18) and (3.21) into Eq. (3.9), one can calculate the geometric phase achieved in nonunitary evolution: MATHEMATICA

computes

$$\begin{aligned} \langle \phi_1(t) | \dot{\phi}_1(t) \rangle &= e^{-i\frac{\eta}{2}t} \sin \frac{\theta_t}{2} \left(i\frac{\eta}{2} e^{i\frac{\eta}{2}t} \sin \frac{\theta_t}{2} - \frac{e^{-\Lambda t} \Lambda}{2} \frac{e^{i\frac{\eta}{2}t} \cos \frac{\theta_t}{2} \tan \theta_0}{1 + e^{-2\Lambda t} \tan^2 \theta_0} \right) \\ &\quad + e^{i\frac{\eta}{2}t} \cos \frac{\theta_t}{2} \left(-i\frac{\eta}{2} e^{-i\frac{\eta}{2}t} \cos \frac{\theta_t}{2} + \frac{e^{-\Lambda t} \Lambda}{2} \frac{e^{-i\frac{\eta}{2}t} \sin \frac{\theta_t}{2} \tan \theta_0}{1 + e^{-2\Lambda t} \tan^2 \theta_0} \right). \end{aligned}$$

For $\tau = 2\pi/\eta$ (cyclic evolution), one finds that

$$\begin{aligned} \sqrt{\omega(0)_1 \omega_1(2\pi/\eta)} &= \sqrt{\frac{1}{2} (1 + \sqrt{\cos^2 \theta_0 + e^{-4\pi\Lambda/\eta} \sin^2 \theta_0})} \in \mathbb{R} \\ \langle \phi_1(0) | \phi_1(2\pi/\eta) \rangle &= (-1) \left(\cos \frac{\theta_0}{2} \cos \frac{\theta_{2\pi/\eta}}{2} + \sin \frac{\theta_0}{2} \sin \frac{\theta_{2\pi/\eta}}{2} \right) \\ &= e^{-i\pi} \underbrace{\cos \left[\frac{\theta_0}{2} - \frac{1}{2} \arctan(e^{-4\pi\Lambda/\eta} \tan \theta_0) \right]}_{\in \mathbb{R}}. \end{aligned} \quad (3.23)$$

To extract the phase, one only needs to consider the imaginary part of the exponent in Eq. (3.9), that is

$$\begin{aligned} - \int_0^{2\pi/\eta} \langle \phi_1(t) | \dot{\phi}_1(t) \rangle dt &\rightarrow -i \int_0^{2\pi/\eta} \text{Im}[\langle \phi_1(t) | \dot{\phi}_1(t) \rangle] dt = i\frac{\eta}{2} \int_0^{2\pi/\eta} \cos \theta_t dt \\ &= i\frac{\eta}{2} \int_0^{2\pi/\eta} \frac{1}{\sqrt{1 + e^{-2\Lambda t} \tan^2 \theta_0}} dt \\ &= i\frac{\eta}{4\Lambda} \ln \left(\frac{(1 - \cos \theta_0)(\sqrt{\cos^2 \theta_0 + e^{-4\pi\Lambda/\eta} \sin^2 \theta_0} + \cos \theta_0)}{(1 + \cos \theta_0)(\sqrt{\cos^2 \theta_0 + e^{-4\pi\Lambda/\eta} \sin^2 \theta_0} - \cos \theta_0)} \right), \end{aligned}$$

provided that the conditions

$$e^{4\pi\Lambda/\eta} + \tan^2 \theta_0 \geq 0 \quad (3.24)$$

$$\frac{1}{\cos^2 \theta_0} e^{-4\pi\Lambda/\eta} \cos(2\theta_0) \leq \frac{1}{\cos^2 \theta_0} (1 + e^{-4\pi\Lambda/\eta} + \cos(2\theta_0)) \quad (3.25)$$

hold. Equation (3.24) is fulfilled. Equation (3.25) can be rewritten as

$$e^{-4\pi\Lambda/\eta} \sin^2 \theta_0 + \cos^2 \theta_0 \geq 0 \quad (3.26)$$

to see that it is also fulfilled. Taking into account the factor $e^{-i\pi}$ in Eq. (3.23), one finally obtains the geometric phase

$$\gamma[\mathcal{P}] = -\pi + \frac{\eta}{4\Lambda} \ln \left(\frac{(1 - \cos \theta_0)(\sqrt{\cos^2 \theta_0 + e^{-4\pi\Lambda/\eta} \sin^2 \theta_0} + \cos \theta_0)}{(1 + \cos \theta_0)(\sqrt{\cos^2 \theta_0 + e^{-4\pi\Lambda/\eta} \sin^2 \theta_0} - \cos \theta_0)} \right), \quad (3.27)$$

which is the main result of [Tong *et al.* 2004] (see Eq. (21) of the paper). One can Taylor expand Eq. (3.27) and to first order yield

$$\gamma[\mathcal{P}] \approx -\pi(1 - \cos \theta_0) + \pi^2 \cos \theta_0 \sin^2 \theta_0 \frac{\Lambda}{\eta}. \quad (3.28)$$

The first term is the well known expression denoting the geometric phase resulting from a rotation of a state $\cos \theta_0/2|+\rangle + \sin \theta_0/2|-\rangle$ through 2π around the z axis (see, for instance, Eq. (2.6)). The second term describes the modification of the geometric phase due to the noise term $\Gamma = \sqrt{(\Gamma/2)} \sigma_z$. Note, that the eigenvectors in Eqs. (3.21) and (3.22) change only because of the right hand side of Eq. (3.18). In consequence, the mere reason why the induced geometric phase is modified in Eq. (3.28) is, that the noise in z direction diminishes the polar angle enclosed by the z axis and the polarization vector, which also results in a shortening of the latter.

In the next Section, a proposal for a neutron polarimeter experiment is given that, under certain assumptions, demonstrates experimentally the modification of the spin evolution on the path \mathcal{P} and therefore also that, in general, $\gamma[\mathcal{P}]$ depends upon dephasing.

3.3 Nonunitary Phases and Neutron Polarimetry

In the following, a neutron polarimeter experiment is explained. It directly measures the influence of noise on the polar angle of the polarization vector \vec{r}_0 and therefore detects influences of dephasing on the evolution path \mathcal{P} . The setup is sketched in Fig. 3.2.

Let the incident pure state of a neutron beam after the polarizer P be denoted as $|+\rangle$. A unitary rotation around the $+x$ axis through a polar angle θ_0 is carried out by a first DC coil (DC 1). The corresponding operator is written as

$$U_1 = \cos \frac{\theta_0}{2} |+\rangle\langle+| - i \sin \frac{\theta_0}{2} |+\rangle\langle-| - i \sin \frac{\theta_0}{2} |-\rangle\langle+| + \cos \frac{\theta_0}{2} |-\rangle\langle-|.$$

In the present treatment, spin rotation operators are used in the form of Eq. (2.21), in which the direction of the rotation axis is specified together with the rotation angle. The operator prepares the neutron beam in the state

$$U_1|+\rangle = \cos \frac{\theta_0}{2} |+\rangle - i \sin \frac{\theta_0}{2} |-\rangle.$$

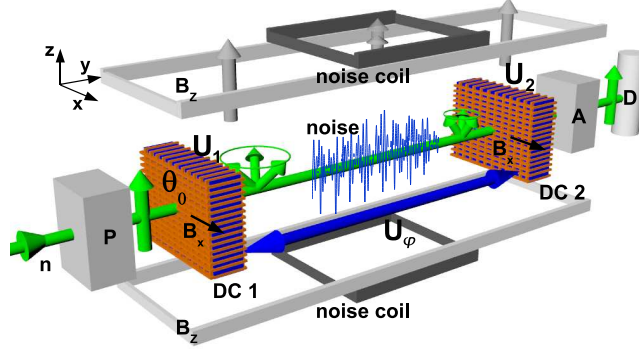


Figure 3.2: Sketch of a neutron polarimetry setup for measurements of noise influences with overall guide field B_z , polarizer P , two DC coils (DC 1 and DC 2) to implement unitary operations U_1 , U_φ , U_2 , noise coils, analyzer A and detector D . Greek letters denote polarization rotation angles. Varying the current of DC 2 results in intensity oscillations from which noise-induced modifications can be inferred.

The effect of the subsequent flight distance s within the guide field B_z , where the polarization vector precesses through the angle $\varphi = 2\mu B_z s / (\hbar v)$ around the z axis (v is the velocity of neutrons), may be written as

$$U_\varphi = e^{-i\varphi/2}|+\rangle\langle+| + e^{i\varphi/2}|-\rangle\langle-|. \quad (3.29)$$

As the relative phase shifts $\mp\varphi/2$ are induced on $|\pm\rangle$, the state evolves to

$$U_\varphi U_1|+\rangle = e^{-i\varphi/2} \cos \frac{\theta_0}{2}|+\rangle - i e^{i\varphi/2} \sin \frac{\theta_0}{2}|-\rangle. \quad (3.30)$$

The current of a subsequent DC coil (DC 2), generating a field B_x , is varied. This is described by the operator

$$U_2 = \cos \frac{\theta}{2}|+\rangle\langle+| - i \sin \frac{\theta}{2}|+\rangle\langle-| - i \sin \frac{\theta}{2}|-\rangle\langle+| + \cos \frac{\theta}{2}|-\rangle\langle-|.$$

The resulting state is:

$$\begin{aligned} U_2 U_\varphi U_1|+\rangle = & e^{-i\varphi/2} \cos \frac{\theta_0}{2} \left(\cos \frac{\theta}{2}|+\rangle - i \sin \frac{\theta}{2}|-\rangle \right) \\ & - i e^{i\varphi/2} \sin \frac{\theta_0}{2} \left(-i \sin \frac{\theta}{2}|+\rangle + \cos \frac{\theta}{2}|-\rangle \right). \end{aligned}$$

It is projected on $|+\rangle$ by the analyzer A , which yields the intensity modulation

$$I \propto |\langle + | U_2 U_\varphi U_1 | + \rangle|^2 = \cos^2 \frac{\varphi}{2} \cos^2 \left(\frac{\theta_0}{2} + \frac{\theta}{2} \right) + \sin^2 \frac{\varphi}{2} \cos^2 \left(\frac{\theta_0}{2} - \frac{\theta}{2} \right). \quad (3.31)$$

This can be written as

$$I \propto 1/2 [1 + \cos(\theta + \theta_0)] \quad (3.32)$$

for $\varphi = 2\pi n$, which means in practice that the inter-coil distance between DC 1 and DC 2 is set to a spin rotation equivalent within B_z of $2\pi n$. Implementing the noise, φ is distributed symmetrically around $2\pi n$. The oscillations are shifted compared to Eq. (3.32) and one obtains the intensity

$$I \propto 1/2 [1 + \sqrt{\cos^2 \theta_0 + e^{-4\pi\Lambda/\eta} \sin^2 \theta_0} \cos(\theta + \theta')], \quad (3.33)$$

with $\theta' = \theta_{2\pi/\eta} = \arctan(e^{-2\pi\Lambda/\eta} \tan \theta_0)$.

As it was done in the experiment described in Chapter 2, the polar and azimuthal angles can be adjusted reliably, so that the path \mathcal{P} of the spin evolution is known to high accuracy for $r_0 = 1$ and $\Lambda = 0$ (for a pure input state undergoing a unitary evolution). Following the well-known relations $\phi_g = -\pi n(1 - \cos \theta_0)$ and $\phi_d = -\pi n \cos \theta_0$ (see Eqs. (2.6) or (2.28) and (2.29)), one can set the current in DC 1 and the inter-coil distance between DC 1 and DC 2 to achieve an evolution path \mathcal{P} that yields a relative Pancharatnam phase between the states $|+\rangle$ and $U_\varphi U_1 |+\rangle$

$$\phi = \arg \langle + | U_\varphi U_1 | + \rangle = -\arctan \left(\tan \frac{\varphi}{2} \right) = -\frac{\varphi}{2},$$

with certain portions of dynamical and geometric phases, which are determined only by θ_0 for fixed $\varphi = 2\pi n$. If $\theta_0 = 0$ is set (DC 1 switched off), the amplitude to find the system in the state $|-\rangle$ vanishes and $|+\rangle$ only gathers an overall dynamical phase of $-\pi n$. No solid angle Ω is enclosed by \mathcal{P} . If $\theta_0 \in]0, \pi/2[$, the measured oscillations are shifted by θ_0 (see Eq. (3.32) above) compared to the case in which DC 1 is turned off. Ω increases with increasing θ_0 . For $\theta_0 = \pi/2$, the induced Pancharatnam phase is of purely geometric origin and consequently equal to $-\Omega/2$. The enclosed solid angle Ω and also the geometric phase $\gamma[\mathcal{P}]$ are therefore functions of the adjusted polar angle θ_0 equal to, neglecting experimental imperfections for the moment, the *measured* shift of oscillations for $\Lambda = 0$ in this experimental setup (see Fig. 3.3). As already stated, the relation between the quantities is given by

$$\gamma[\mathcal{P}] = -\Omega/2 = -\pi n(1 - \cos \theta_0). \quad (3.34)$$

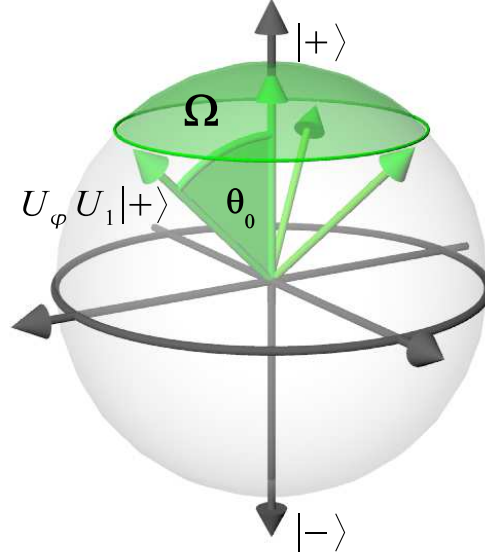


Figure 3.3: The spin evolution given by $U_\varphi U_1$ for $\varphi = 2\pi$ (see text). It accumulates a relative Pancharatnam phase between $|+\rangle$ and $U_\varphi U_1|+\rangle$ with a geometric part equal to $-\Omega/2$. It is a function of θ_0 which is also equal to the measured oscillation shifts for $\Lambda = 0$ (without noise).

For states with input purity $r_0 < 1$ undergoing unitary evolutions, the solid angle arising from the spin evolution $U_\varphi U_1$ undergone by $|+\rangle$ is *the same* as in the pure state case. The radius r_0 of the projection sphere is smaller, but also the surface area enclosed by \mathcal{P} on this sphere is decreased accordingly, so that Ω is constant. Because the mixed-state phase for unitary evolutions is defined as the argument of a weighted average of, in our case, the phase factors $\exp(i \arg\langle +|U_\varphi U_1|+\rangle)$ and $\exp(i \arg\langle -|U_\varphi U_1|-\rangle)$ (see Eq. (2.9)), its geometric part in [Sjöqvist *et al.* 2000] and [Singh *et al.* 2003] is, nevertheless, dependent on r_0 :

$$\Phi_g = -\arctan\left(r_0 \tan \frac{\Omega}{2}\right). \quad (3.35)$$

Being able to set a well-known evolution path, the geometric mixed-state phase for cyclic unitary evolutions can also be obtained employing Eq. (3.35) using the results of the experiment described here: In the present proposal as well as in the one of Chapter 2, the experimenter can set θ_0 and φ . Their adjustment can be checked by comparing the measured oscillation shifts with the expected intensity behavior (see Eq. (3.31)). Ω is known. For cyclic unitary evolutions one can extract r_0 , if a priori unknown, from the contrast

of measured intensity oscillations. Alternatively, r_0 can also be adjusted by the mixing-method introduced in Chapter 2. From these results, the geometric mixed-state phase for cyclic unitary evolutions can be calculated. What about the $\Lambda \neq 0$ case (nonunitary evolutions)? Also in this case one can assume that we know very well the path of the *average* Bloch vector \vec{r}_t in the experiment. The vector rotates through $2\pi n$ around the z axis, but additionally the length of its projection on the xy plane is reduced exponentially with time. The length of the vector itself – the time-dependent purity r_t – and the time-dependent polar angle θ_t that the vector encloses with the z axis behave as

$$r_t = \sqrt{\cos^2 \theta_0 + e^{-2\Lambda t} \sin^2 \theta_0} \quad (3.36)$$

and

$$\theta_t = \arctan(e^{-\Lambda t} \tan \theta_0) \quad (3.37)$$

during the evolution. The contrast and the shift of measured oscillations are modified in the same manner as r_t and θ_t (see Eq. (3.33)), respectively. The solid angle accumulated in a cyclic nonunitary evolution with fixed θ_0 , η and noise in z direction, as assumed in our experiment, is a function of r_t and θ_t , which are again functions of Λ . Strictly assuming that the average Bloch vector dynamics, as given above in this paragraph, correctly describes the experiment, it is clear that for $\theta_0 \rightarrow \pi/2$ the purity, Eq. (3.36), behaves as $r_t \rightarrow e^{-\Lambda t}$, while the time dependent polar angle, Eq. (3.37), approaches $\theta_t \rightarrow \pi/2$. The polar angle in this particular evolution does not change and since the solid angle is independent of a mere change of the purity, be it before or during the evolution, Ω is constant. Now, if we do not detect a noise-induced modification of the oscillation shift θ' in our experiment, we may conclude that the solid angle has not been changed by the noise. Again, this conclusion can *only* be drawn if the above mentioned concept of average Bloch vector dynamics is considered to be the correct description in our experiment.

What about the corresponding geometric phase? Equation (3.6) shows that the mixed-state phase under nonunitary evolutions ($\gamma[\mathcal{P}]$) is an extension of the mixed-state phase under unitary evolutions (Φ_g) as in [Sjöqvist *et al.* 2000] and [Singh *et al.* 2003] for time dependent eigenvalues of the evolving density matrix. For unitary evolutions (without noise) it reduces to Eq. (3.35), as is clearly stated in [Tong *et al.* 2004]. In addition, looking back at Eq. (3.35), one notices that the closer we set Ω to 2π for general r_0 , the less does the mixed-state geometric phase Φ_g depend on r_0 . This behavior is shown by theory curves in Fig. 3.4 and was demonstrated experimentally in Chapter 2 and [Klepp *et al.* 2008].

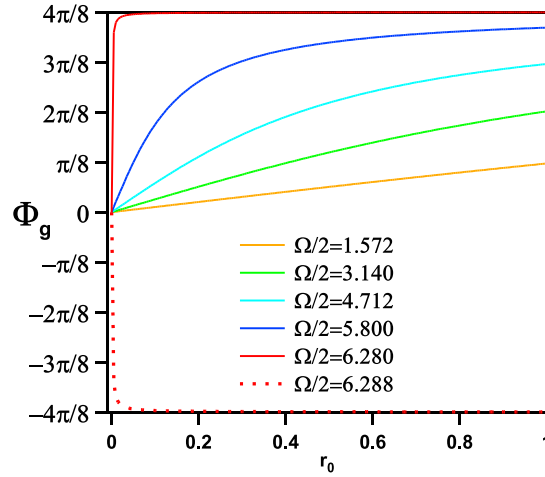


Figure 3.4: Theory curves of geometric mixed-state phase for unitary evolutions calculated from Eq. (3.35) for various Ω . The red curves are for Ω slightly below and above 2π .

So, taking into account the close relation between the mixed-state Pancharatnam phases for unitary (Φ_g) and nonunitary ($\gamma[\mathcal{P}]$) evolutions, the insensitivity of $\gamma[\mathcal{P}]$ for the set polar angle $\theta_0 = \pi/2$ can be understood in an intuitive way: Φ_g is in this case independent of the incident purity r_0 (see Fig. 3.4). Nonunitary evolutions with $\Lambda > 0$ change neither the polar angle $\theta_0 = \theta' = \pi/2$ nor the solid angle $\Omega = 2\pi$. Only r_t is modified for $\Omega = 2\pi$. Therefore, since $\gamma[\mathcal{P}]$ and Φ_g are closely related in the way explained above, also $\gamma[\mathcal{P}]$ should be insensible to our particular noise, given by the Lindblad operator $\Gamma = \sqrt{\Lambda/2}\sigma_z$. In this scenario, a noise-induced modification of the nonunitary mixed-state geometric phase, that is merely a function of the solid angle enclosed by the spin evolution for $\theta_0 = \pi/2$, could be detected by means of measuring noise-induced shifts of oscillations θ' . Also here, one has to assume that the average path is correctly given by the dynamics of the average Bloch vector, which seems reasonable since the noise merely changes the magnetic field in z direction.

However, the second term of Eq. (3.28) cannot be measured directly by means of the described experimental setup. We have no possibility to calculate the qualitative modification of the geometric phase from the result of the proposed experiment, except by the use of Eq. (3.28), the validity of which we want to test. An alternative model, only based on geometric consideration of the Bloch vector dynamics, for instance, could perhaps be established and compared to the one in [Tong *et al.* 2004].

3.4 Experiment

The experiment was done in the same way as the mixed-state phase measurement reported in Chapter 2. Therefore, most of the experimental methods have already been described in Section 2.6 and will not be treated in more detail here. We refer to the corresponding Section in Chapter 2, where a certain experimental method is explained, if necessary. The measurements were carried out at the TRIGA reactor in Vienna after the polarimeter beam-line refurbishment in spring 2008. Photographs of the setup are shown in Fig. 3.4. The measurement procedure is explained and the obtained data is shown. Data analysis is considered and the results are discussed.

3.4.1 Measurement and Results

The neutron beam incident from the pyrolytic graphite crystal monochromator with mean wavelength of $2.0(2)\text{\AA}$ and a spectral width $\Delta\lambda/\lambda \sim 2\%$ as stated in [Geppert and Both 2009] was polarized up to $r(0) \sim 99\%$ by reflection from a bent Co-Ti supermirror array. The analyzing supermirror was slightly de-adjusted to higher incident angles to suppress second order intensity in the incident beam as described in Section 2.6.3. The final maximum intensity in the ^{10}B detector was about 320 cts/s with two coils (with Cu windings for x and z directions each) in the beam that had a cross-section of roughly 2 cm^2 . The rectangular-shaped Cd diaphragms at entrance and exit of polarizer and analyzer were $\sim 1\text{ cm}$ in width and $\sim 2\text{ cm}$ height. The background was very low due to the excellent shielding of the detector.

In order to find the DC coil current values for required polarization rotation angles of DC 1 and DC 2, each coil current was adjusted as explained in Section 2.6.6. With $+\pi/2$ rotations around the x axis set for both coils, inter-coil distances were adjusted to a spin rotation angle equivalence within the guide field (roughly 13 G) of integer multiples of 2π . For this purpose, the second coil was mounted on a stepper motor which improved the reproduction of positions considerably, compared to what was stated in Section 2.6.6. One step of the motor corresponded to $0.625\ \mu\text{m}$. While tilting effects could be eliminated, the slackness of mounting devices was still an issue. However, the error was considered small enough to be neglected. The method is described in Section 2.6.7. The oscillation obtained from variation of the motor position is shown in Fig. 3.6. The inter-coil distance at the chosen position (intensity minimum) was about 30 cm, from which one can calculate that within B_z the polarization vector was rotated through an angle of $2\pi \times 5$. Furthermore, from the fit parameter $f = 0.12573 \pm 0.00017$ of the plot in Fig. 3.6 one can deduce the guide field strength: $B_z = \hbar v f \cdot 10^3 / (2\mu) = 13.4(1)\text{ G}$. This provides

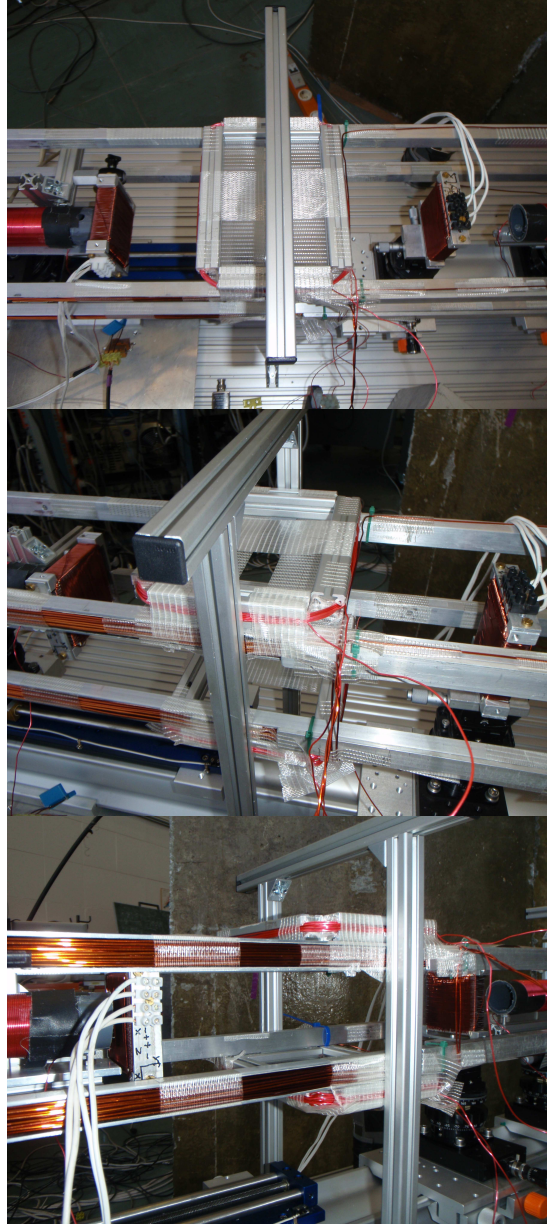


Figure 3.5: Experimental setup implemented for measuring noise influences on phases: The neutron beam is incident from the right. The visible RF flippers were not used in the measurement. The right and left DC coils (DC 1 and DC 2) correspond to the operators U_1 and U_2 of Section 3.3, respectively. The noise coil windings are directly attached to the guide field coils to assure the field directions to be parallel.

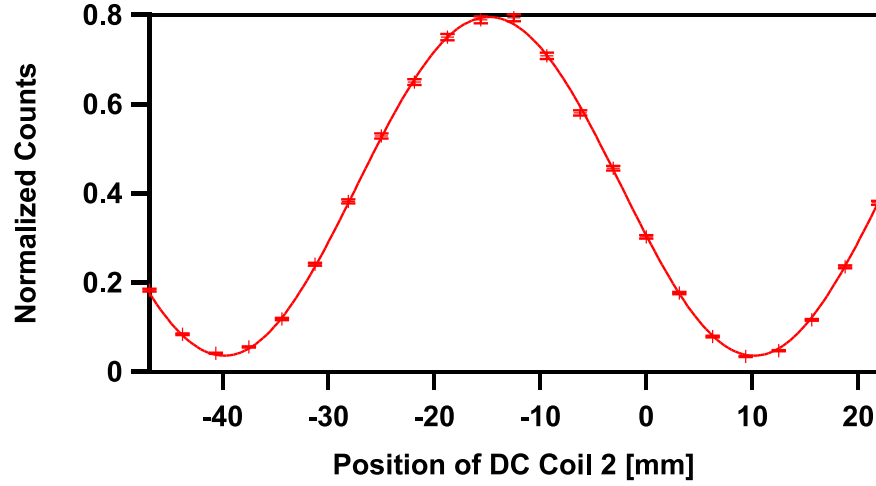


Figure 3.6: Variation of the Position of DC 2 mounted on a stepper motor.

also a value for the parameter η : $\eta = \omega_L = 2\mu B_z/\hbar = 2.45(2) \cdot 10^5$ rad/s, which is a reasonable result considering that the neutron spin rotates about $2000/0.05 = 4 \cdot 10^4$ times through 2π in one second.

DC 1 was set to give the following rotation angles θ_0 , each corresponding to $B_x^{(1)}$ currents in DC 1:

Angle [°]	$B_x^{(1)}$ current [mA]
0	0
18	106
36	211
54	317
72	422
90	528
108	634
126	739
144	845
162	950
180	1056

For each of those angles, the $B_x^{(2)}$ current of DC 2 was scanned from -1600 mA to 1600 mA in steps of 200 mA. At each current in DC 2, the intensity reaching the detector D was recorded for 60 s. Plotting the measured intensities versus the $B_x^{(2)}$ current for the second coil, one obtains the black curves in each graph of Fig. 3.7.

The output of the signal generator (SONY/TEKTRONIX AFG320 as in Chapter 2) was plugged into the input of an EPS TO/E7610 amplifier. Its output was connected to a pair of noise coils (~ 13.7 cm in length and ~ 17 cm in width) with about 15 windings each. They were placed directly onto and below the guide field coils to provide for perfect alignment with the guide field direction (see Figs. 3.2 and 3.4). For the signal generator the NOISE function was chosen with the frequency set to 20 kHz (as in Chapter 2) and seven amplitude readings: 0V (off), 0.8V, 1.6V, 2.4V, 3.2V, 4V and 5V. The measured voltage signal as created by the signal generator is shown in Fig. 2.30.

In total, for each of the θ_0 values, the intensity oscillation obtained by variation of the $B_x^{(2)}$ current in DC 2 was recorded at all seven noise levels. All acquired data is shown in Fig. 3.7. From the graph for $\theta_0 = 90^\circ$, one can see clearly that the noise has no influence on oscillation shifts for this polar angle, for which the evolution path \mathcal{P} encloses the hemisphere and the induced Pancharatnam phase ϕ is purely geometric. No modification is also shown in the graphs for $\theta_0 = 0^\circ$ and $\theta_0 = 180^\circ$, for which no geometric phase or no phase at all (for $\theta_0 = \pi$, the states $|+\rangle$ and $U_\varphi U_1|+\rangle$ are orthogonal) is accumulated, respectively. All other oscillation shifts are modified according to the noise level in the noise coils. The measurements for $\theta_0 = 0^\circ, 90^\circ, 180^\circ$ confirm the theoretical prediction of [Tong *et al.* 2004]: The geometric phase is insensible to dephasing only when the Bloch vector precesses in the equatorial plane. Note that for the measurements of 54° and 126° the normalized count rate was lower at the measurement of the black (no noise) and the light blue curve (noise level: 2.4V) in the data plots, respectively. The reason for this is a temporarily higher monitor count rate assumed to originate from electronic instabilities. Nevertheless, the phase θ' of those two curves also matches the theoretical prediction.

From the sine fits in Fig. 3.7 (solid lines), the shifts θ' of the oscillations are determined and plotted in Fig. 3.8. Also here, it can be seen that the measured shifts for $\theta_0 = \pi/2$, for which \mathcal{P} lies only on geodesics, are not influenced by the noise level. The solid lines are piecewise fits (because of the singularity of the 'tan' at $\theta_0 = \pi/2$) of the function

$$\arctan(e^{-2\pi\Lambda/\eta} \tan \theta_0)$$

to the data. For better illustration, the same behavior is shown in Fig. 3.9 (equivalent to Fig. 3.8), where the difference of oscillation shifts measured with and without noise is plotted. Here, the solid lines are piecewise fits of the function

$$\theta_0 - \arctan(e^{-2\pi\Lambda/\eta} \tan \theta_0).$$

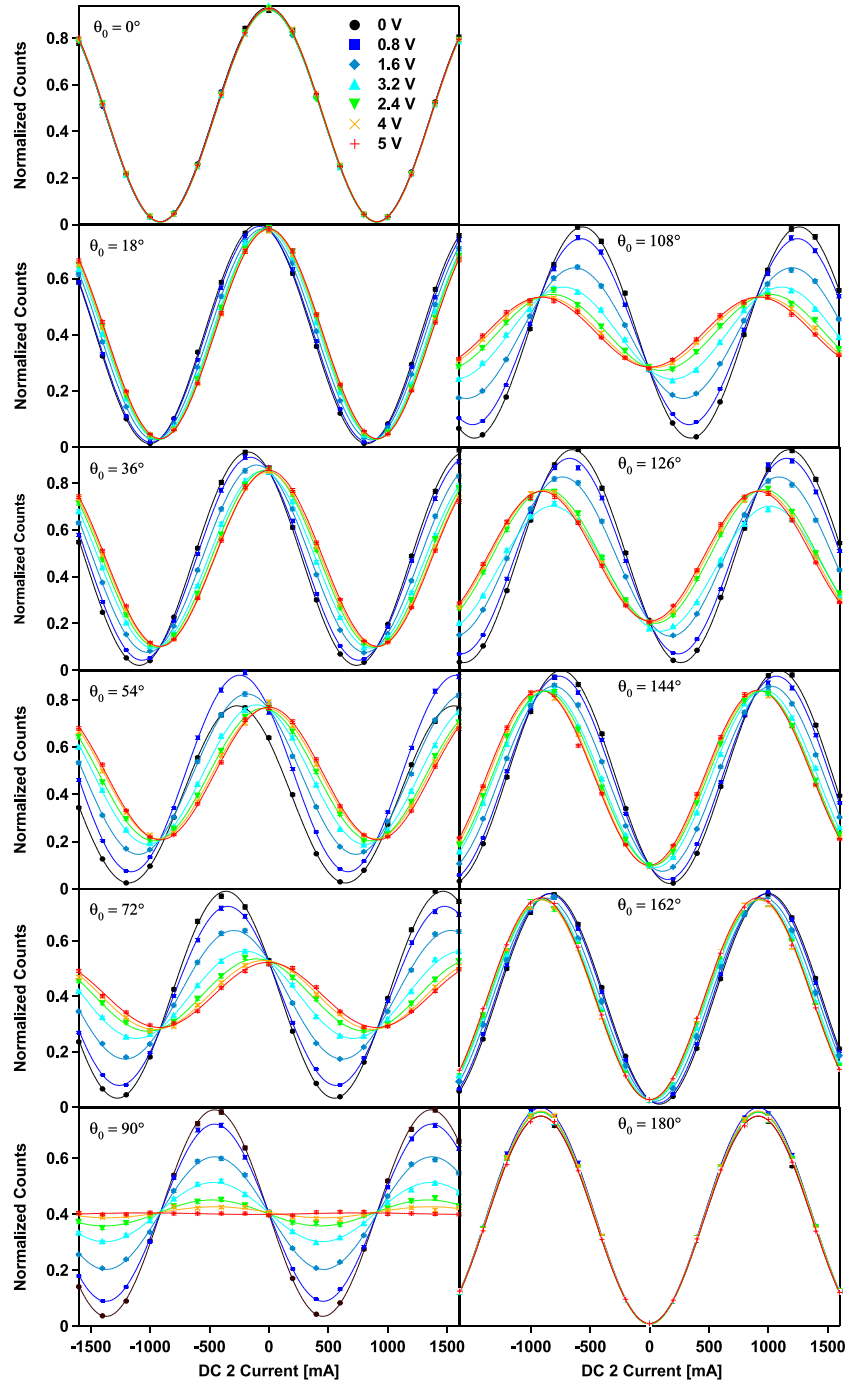


Figure 3.7: Acquired intensity oscillations for 11 settings of θ_0 (see text) for seven noise levels. The oscillations for $\theta_0 = 0^\circ, 90^\circ, 180^\circ$ are not shifted by the noise.

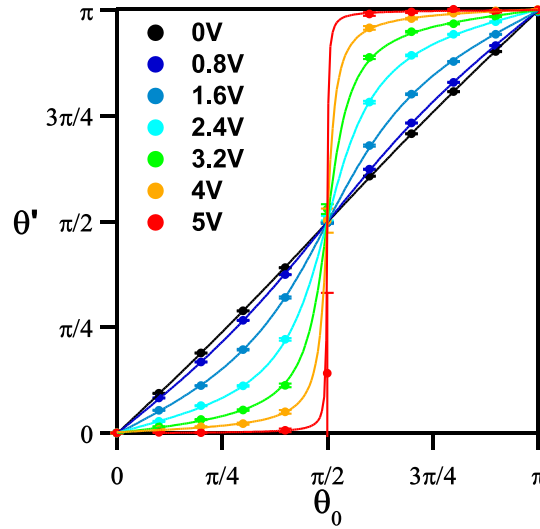


Figure 3.8: Measured shifts θ' of oscillations for all noise levels as obtained from the fits to the data in Fig. 3.7 versus θ_0 . Independent of the noise level, the result for $\theta_0 = \pi/2$ is $\theta' \sim \pi/2$.

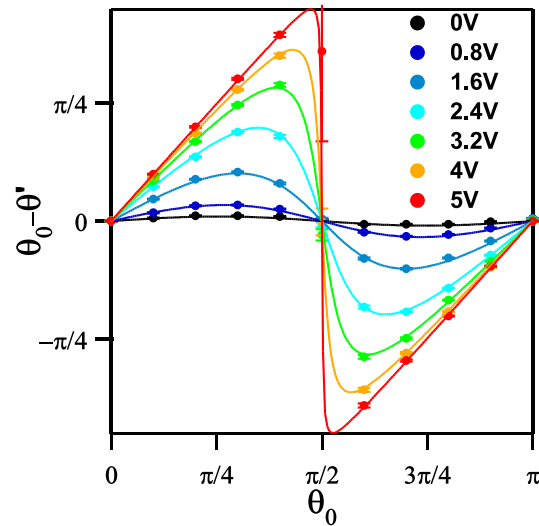


Figure 3.9: $\theta_0 - \theta'$ versus θ_0 for all noise levels. For induction of purely geometric phase, the curves for all noise levels intercept at the center point.

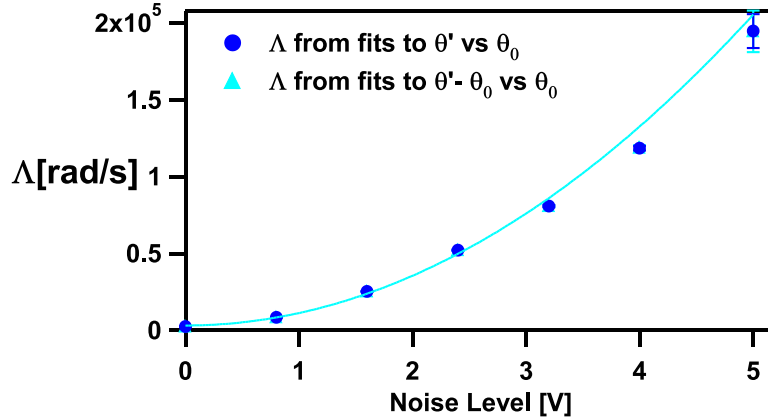


Figure 3.10: Parameter Λ versus noise level from the signal generator. The solid line is a quadratic fit to the data.

The data in both, Fig. 3.8 and 3.9, are in good agreement with the notion of the average Bloch vector dynamics, that is characterized by Eqs. (3.36) and (3.37). From the fits in Figs. 3.8 and 3.9, one can obtain the parameter Λ for each noise level. The explicit values for Λ are:

Noise Level [V]	Λ [rad/s]
0	$2.4(1) \cdot 10^3$
0.8	$8.2(1) \cdot 10^3$
1.6	$2.52(2) \cdot 10^4$
2.4	$5.20(3) \cdot 10^4$
3.2	$8.07(6) \cdot 10^4$
4	$1.18(2) \cdot 10^5$
5	$1.9(1) \cdot 10^5$

They are plotted in Fig. 3.10. Note that there are small differences between the points of the two data sets due to the different fit functions. However, discrepancies range within the standard deviations obtained from the fits.

As in Chapter 2, we use noise that consists of supposedly Gaussian distributed offsets from the magnetic guide field B_z . Each neutron undergoes a different unitary evolution and the average Bloch vector movement is, apart from the adjusted angles, determined by the distribution of the noise field. In [Bertlmann *et al.* 2006] the relation between a damping factor $e^{-\Lambda t}$ and the variance of Gaussian distributed rotation angles caused by noise is calculated. In our case, such a factor is added to the relative phase factor $e^{-i\eta t}$ induced between $|+\rangle$ and $|-\rangle$ during the precession, as can be seen in Eq. (3.17).

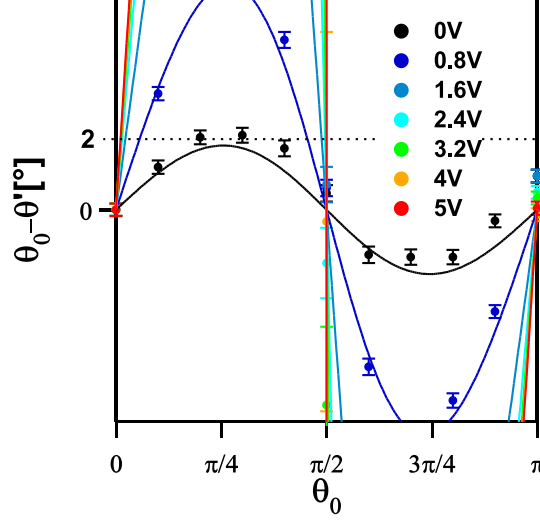


Figure 3.11: Vertical zoom of Fig. 3.9. A modulation is clearly observable.

The rotation angles φ in the matrix elements of a transformation operator $U_\varphi = \exp(-i\varphi\sigma_z/2)$, from which the precession phase factor originates (see Eq. (3.29)), are affected by the noise. Explicitly, the distribution function of rotation angles is assumed to be

$$P(\varphi) = \frac{1}{\sqrt{2\pi}\sigma} \exp\left(-\frac{\varphi^2}{2\sigma^2}\right), \quad (3.38)$$

where σ is the standard deviation. One can average over all possible phase factors by calculating the integral

$$\frac{1}{\sqrt{2\pi}\sigma} \int e^{\mp i\varphi/2} e^{-\frac{\varphi^2}{2\sigma^2}} d\varphi = \frac{1}{\sqrt{2\pi}\sigma} \int \left(\cos\frac{\varphi}{2} - i \sin\frac{\varphi}{2}\right) e^{-\frac{\varphi^2}{2\sigma^2}} d\varphi. \quad (3.39)$$

Because the integration region is symmetric and the 'sin' function is asymmetric around zero, it does not contribute to the result and one obtains

$$\frac{1}{\sqrt{2\pi}\sigma} \int \cos\frac{\varphi}{2} e^{-\frac{\varphi^2}{2\sigma^2}} d\varphi = e^{-\frac{\sigma^2}{2}}. \quad (3.40)$$

Comparing this to $e^{-2\pi\Lambda/\eta}$ (for a cyclic evolution) one can see that

$$\Lambda \frac{2\pi}{\eta} = \frac{\sigma^2}{2}. \quad (3.41)$$

The right hand side is a (dimensionless) angle squared. Therefore, one finds that Λ is related to the noise level voltage as $\Lambda \propto V^2$, since $2\mu\Delta B_z \cdot 2\pi/\eta$ corresponds to the width of the distribution of spin rotation angles induced by $\Delta B_z \propto V$, the width of the noise field distribution. The quadratic dependence in Fig. 3.10 shows this effect and thereby confirms that the noise from the signal generator is Gaussian distributed.

One can also see in Fig. 3.10 and in the corresponding Table, that even with the output of the signal generator switched off, this method determines a noise level of about 2400 (rad/s), while we expect a value close to zero. Surprisingly, enlarging Fig. 3.9, one can see that there is a clearly visible modulation of $\theta_0 - \theta'$ (see Fig. 3.11). Even though the set and measured phases θ_0 and θ' only differ by 2° at maximum (fourth black data point from the left in Fig. 3.11), the parameter Λ is very sensible for small θ' due to its dependence on the natural logarithm, as is expressed by:

$$\Lambda = -\frac{\eta}{2\pi} \ln \left(\frac{\tan \theta'}{\tan \theta_0} \right).$$

Stray fields in z direction, picked up by the noise coils, that could contribute to the noise strength, play a minor role in our experimental setup. The small phase modulation could be explained by assuming that the precession angle φ was not exactly equal to $2\pi n$, but $2\pi n + \Delta\varphi$. Geometric considerations show that θ' is then given by

$$\theta' = \arctan \left(\cos(\Delta\varphi) e^{-2\pi\Lambda/\eta} \tan \theta_0 \right). \quad (3.42)$$

By fitting $\theta_0 - \arctan \left(\cos(\Delta\varphi) e^{-2\pi\Lambda/\eta} \tan \theta_0 \right)$ to the black data points in Fig. 3.11 with Λ fixed to zero, we obtain $\Delta\phi = 0.34(1)$ rad or roughly 20° . This value is much too large considering the error of the position scan and the motor resolution, which are 0.3° and $0.625 \mu\text{m}$, respectively. On the other hand, if we fix the error for the adjustment of φ in the fit to the expected 0.3° for the worst case, we still obtain a noise level of $\sim 2350/\text{s}$. Even if the amplitude of the unexpected modulation is very small and has no (obvious) consequences for the results of the experiment, this issue remains – so far – unexplained and should be clarified in the future.

In Fig. 3.12, the dependence of measured oscillation shifts on Λ/η is shown. Again, it is clearly visible that θ' is strongly influenced by the noise except for the case of $\theta_0 = \pi/2$, where the path \mathcal{P} fulfills the parallel transport condition and leads to a purely geometric phase. The unwanted noise level obtained with the signal generator switched off has no impact on this result.

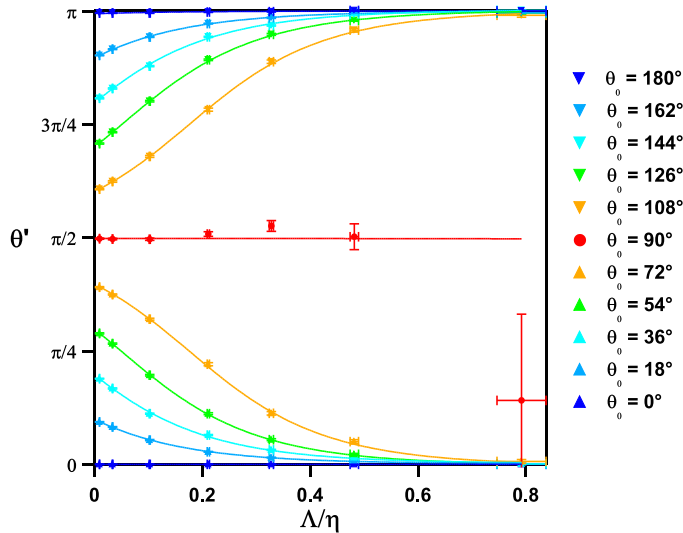


Figure 3.12: Induced oscillation shifts versus λ/η . The rightmost red data point corresponds to the curve for $\theta_0 = \pi/2$ and maximum Λ in Fig. 3.7, with almost zero contrast.

3.5 Discussion

In contrast to the claim by [Carollo *et al.* 2003], it is calculated in [Tong *et al.* 2004] that only in the case when the spin state precesses in the equatorial plane where the induced phase is of purely geometric nature, it is independent of fluctuations of the precession field. The geometric phase in [Tong *et al.* 2004] is gauge invariant, i. e. its value only depends on the path traced out in state space, which is a stringent property for a well defined phase concept. Their results reduce to the ones of [Sjöqvist *et al.* 2000] and [Singh *et al.* 2003] in the limit of unitary evolutions, which makes this phase a promising candidate for future developments.

In the described neutron polarimeter measurements, the system is driven on cyclic evolution paths \mathcal{P} by nonadiabatic rotations chosen by the experimenter. The evolutions induce a total relative Pancharatnam phase between the states $|+\rangle$ and $U_\varphi U_1|+\rangle$, the geometric part of which being equal to $-5\pi(1 - \cos \theta_0)$ for 5 full rotations around the field axis ($\varphi = 5 \times 2\pi$). Without noise, the measured shift of oscillations θ' corresponds to the polar angle θ_0 set by U_1 . $\theta' = 0$ for $\theta_0 = 0$ and increases together with the solid angle Ω , enclosed by \mathcal{P} (see Figs. 3.7, 3.9 and 3.11). Applying noise in direction parallel to the precession field axis, it is found that *only* for $\theta_0 = \pi/2$ the shift of oscillations θ' is robust against the noise.

What conclusions can be drawn from this result? We assume that an average Bloch or polarization vector \vec{r}_t , describing the spin state during the evolution, rotates through $2\pi n$ around the z axis, after being tilted by the polar angle θ_0 in the coil DC 1. In addition, its projection on the xy plane of the Bloch sphere, $\sin\theta_0$, decreases exponentially during the evolution, with the noise strength Λ as "decay constant" (see Eq. (3.37)). Since the projection of \vec{r}_t on the z axis ($r_t \cos\theta_0$) is assumed to be constant in the experiment, the purity r_t is reduced as well (see Fig. 3.1). This affects directly the contrast and the shift θ' of measured oscillations as can be seen from Eq. (3.33).

From the assumed evolution of the average Bloch vector, it is clear that for a precession in the equatorial plane, the purity r_t behaves as $e^{-\Lambda t}$ and the polar angle θ_t is constant and equal to $\pi/2$ (see Eqs. (3.36) and (3.37)). Also, the solid angle is independent of the purity and therefore Ω is constant, because θ_t is constant. In Fig. 3.7 it is clearly seen, that only for this particular evolution the measured data exhibits such a behavior, as expected. However, a drawback of the carried out experiment is, that we only set the polar angle of the average Bloch vector in the beginning and measure it at the end of the evolution. We do not know what exactly happens in between. For instance, the modification of the polar angle for $\theta_0 \in]0, \pi/2[$ could, in principle, take place in a sudden jump instead of the assumed smooth transition, for some unknown reason. The oscillation shift θ' would then be changed, even if the solid angle Ω remains constant. These jumps could occur for all set angles θ_0 except for $\theta_0 = 0, \pi/2, \pi$ to explain the data in Fig. 3.7. Even if such jump-like behavior seems very unlikely, only if we neglect such unknown and chaotic evolutions during the Larmor precession between DC 1 and DC 2, we can conclude from the obtained data, that the solid angle has not been changed by the noise for $\theta_0 = \pi/2$.

For the conclusion about the geometric phase one runs into similar trouble. Again, at first one assumes to know exactly the path of the average Bloch vector \vec{r}_t in the experiment. As was stated in Section 3.3, if $\theta_0 = \pi/2$, the geometric mixed-state phase for unitary evolutions Φ_g (for $\Lambda = 0$) can be considered independent of r_0 and, intuitively, also $\gamma[\mathcal{P}]$ (for $\Lambda > 0$) of r_t . This would mean that noise-induced modifications of the geometric phase can be measured by looking at noise-induced shifts θ' of oscillations recorded in our experiments. Also here, the main objection that could be raised deals with the assumptions that have to be made for the evolution between setting and measuring the polar angle, that remains, in principle, completely unknown in the described experiment. For the future, this objection can probably be met by measuring intensity oscillations for a several noncyclic paths in the described experiment. The obtained data can then be compared to expectations derived from the above explained Bloch vector dynamics and

verify its predictions.

Apart from this problem, the measured oscillation shift is *not identical* to the geometric phase and therefore its quantitative behavior of the modification was not measured directly in the carried-out experiment. In more detail, we can plug the oscillation shift θ_0 , measured without noise, into the first term of Eq. (3.28) – which is well-known and widely accepted – and yield the correct value for the geometric phase without the influence of noise. With the signal generator switched on, θ_0 changes to θ' , but we have no possibility to verify the magnitude of the second term on the right hand side of Eq. (3.28). It would be interesting to test also the qualitative predictions of the theory in [Tong *et al.* 2004]. Moreover, an experiment in which the shift of measured intensity oscillations is equal to the geometric phase part of a particular evolution seems much more elegant. Also the noise-induced changes would be directly observable.

The measurements explained here are a first step towards the clarification of the issue. The experiment points to the right direction and yields results that show indications, though perhaps not a clear proof, of the behavior predicted by [Tong *et al.* 2004]. As it is the case in many fields of experimental physics, further investigations are on the way to close the "loopholes" that are still open.

In order to overcome all above objections, a method is needed that is not merely sensible to some angle that could be changed by the noise during the evolutions, but it is necessary that the measured phase shift of oscillations is *equal* to the geometric phase part of the evolution. The experiment carried out in [Wagh *et al.* 1998] seems, at first glance, to be a candidate. But also there, only the total Pancharatnam phase between the states in the two interferometer paths is measured. An experiment that can set evolutions inducing arbitrary values of geometric phase *and* can get rid of the dynamical phase must probably use a spin echo approach [Bertlmann *et al.* 2004, Filipp *et al.* 2009]. With the experimental setup in [Filipp *et al.* 2009] one can, in principle, implement nonadiabatic noise (different from the adiabatic noise used for the measurement in the paper) and perhaps measure the modification of the Berry phase for adiabatic, cyclic and nonunitary evolutions.

Chapter 4

Conclusion and Outlook

In all experiments and applications, pure input states and noiseless evolutions are only approximations that can not be achieved in practice. Therefore it is important to develop more realistic models to test them in experiments and be aware of differences to the pure state case. The theoretical development of the mixed-state phases for unitary evolutions is outlined in Chapter 2. A detailed description of a dedicated neutron polarimeter experiment, proposed by [Wagh and Rakhecha 1995b] and [Larsson and Sjöqvist 2003], is given. An interpretation of the experiment in terms of spin-momentum entanglement is provided. The experimental details of the setup are described and the measurement procedures for obtaining the mixed-state Pancharatnam phase (general, dynamical and geometric), dependent on the input purity, are discussed. The results agree well with theoretical predictions. In particular, the nonadditivity of the mixed-state phase was demonstrated experimentally [Klepp *et al.* 2008]. Nonadditivity, in this context, is a consequence of the mixed-state phase definition as weighted average of the phase factors of all pure state components in the density matrix.

As a further step, in Chapter 3, the derivation of the Pancharatnam phase for nonunitary evolutions developed in [Tong *et al.* 2004], is explained. Expectations for the example of a qubit under noise in directions parallel to the precession axis of the Bloch vector are calculated. Theory predicts the acquired geometric phase to be robust against this particular noise only if the state is parallel transported, in this particular setup, if the evolution path lies in the equatorial plane of the Bloch sphere. We conclude in an intuitive way, that because the mixed-state Pancharatnam phase for unitary evolutions is shown to be independent of the purity for this particular kind of evolution in Chapter 2, the same should be correct for the nonunitary case. A neutron polarimeter experiment is described, that measures the shift of obtained

intensity oscillations as a function of noise strength in auxiliary noise coils along the beam path. The data shows that, if the Bloch vector precesses in the equatorial plane in the evolution, the shift is constant, independent of the noise level. If the dynamics of the average Bloch vector in the experiment are considered to be a correct description in the particular circumstances, we can conclude that the robustness of the geometric phase for precession in the equatorial plane is experimentally demonstrated. However, a qualitative test of the theoretical predictions can not be provided by the method. Further effort is needed in this field. For instance, an experiment with ultra-cold neutrons based on the spin-echo approach to cancel out all dynamical phase contributions acquired during the evolution, could lead to full clarification of the issue.

In so-called *quantum erasure* experiments, loss of visibility of intensity oscillations is observed [Scully and Drühl 1982, Stern et al. 1990, Kwiat *et al.* 1992]. In this concept, the gain of which-way information (*welcher Weg* information) is responsible for decreasing visibility in quantum interference experiments. Which-way information is available in the experiments, because of entanglement of the quantum system with an ancilla system (typically called an environment). Indistinguishable states of a quantum system become distinguishable, because one can carry out a measurement on the ancilla system and thereby gain knowledge about the quantum system. In a quantum eraser experiment, gained which-way information can be *erased* again to recover fringe visibility.

In [Bhandari 1992], it is argued that a Pancharatnam phase, acquired in the experiment, is responsible for the loss of contrast and, consequently, for decoherence in which-way experiments. Neutron interferometry and especially polarimetry are ideally suitable for quantum erasure-like experiments due to the very weak unwanted interactions of neutrons with the environment. Which-way measurements with polarized neutrons are currently carried out and analyzed, in which the loss of fringe visibility can be both interpreted in terms of distinguishable paths due to entanglement with an ancilla system or, alternatively, a Pancharatnam phase. The preliminary results agree well with the predictions of both concepts. This points in direction of their equivalence.

Bibliography

- [ACKN 1] By courtesy of K. Durstberger-Rennhofer.
- [Aharonov and Anandan 1987] Y. Aharonov and J.S. Anandan, Phys. Rev. Lett. **58**, 1593 (1987).
- [Alefeld *et al.* 1981] B. Alefeld, G. Badurek and H. Rauch, Phys. Lett. A **83**, 1 (1981).
- [Allman *et al.* 1997] B.E. Allman, H. Kaiser, S.A. Werner, A.G. Wagh, V.C. Rakhecha and J. Summhammer, Phys. Rev. A **56**, 4420 (1997).
- [Anandan *et al.* 1997] J. Anandan, J. Christian and K. Wanelik, Am. J. Phys. **65**, 3 (1997).
- [Anandan *et al.* 2002] J. Anandan, E. Sjöqvist, A.K. Pati, A. Ekert, M. Ericsson, D.K.L. Oi and V. Vedral, Phys. Rev. Lett **89**, 268902 (2002).
- [Badurek *et al.* 1993] G. Badurek, H. Weinfurter, R. Gähler, A. Kollmar, S. Wehinger and A. Zeilinger, Phys. Rev. Lett **71**, 307 (1993).
- [Berry 1984] M.V. Berry, Proc. R. Soc. Lond. A **392**, 45 (1984).
- [Berry 1987] M.V. Berry, J. Mod. Opt. **34**, 1401 (1987).
- [Bertlmann *et al.* 2004] R.A. Bertlmann, K. Durstberger, Y. Hasegawa and B. C. Hiesmayr, Phys. Rev. A **69**, 032112 (2004).
- [Bertlmann *et al.* 2006] R.A. Bertlmann, K. Durstberger and Y. Hasegawa, Phys. Rev. A **73**, 022111 (2006).
- [Bhandari 1992] R. Bhandari, Phys. Rev. Lett. **69**, 3720 (1992).
- [Bhandari 1997] R. Bhandari, Phys. Rep. **281**, 1 (1997).
- [Bhandari 2002] R. Bhandari, Phys. Rev. Lett. **89**, 268901 (2002).

- [Bitter and Dubbers 1987] T. Bitter and D. Dubbers, Phys. Rev. Lett. **59**, 251 (1987).
- [Buchelt 1997] R. Buchelt, Diploma Thesis, Technical University of Vienna, Vienna, Austria (1997).
- [Carollo *et al.* 2003] A. Carollo, I. Fuentes-Guridi, M. França Santos and V. Vedral, Phys. Rev. Lett. **90**, 160402 (2003).
- [De Chiara and Palma 2003] G. de Chiara and G. M. Palma, Phys. Rev. Lett. **91**, 090404 (2003).
- [Du *et al.* 2003] J. Du, P. Zou, M. Shi, L.C. Kwek, J.-W. Pan, C.H. Oh, A. Ekert, D.K.L. Oi and M. Ericsson, Phys. Rev. Lett. **91**, 100403 (2003).
- [Du *et al.* 2007] J. Du, M. Shi, J. Zhu, V. Vedral, X. Peng and D. Suter, arXiv:quant-ph/0710.5804v1.
- [Ericsson *et al.* 2003a] M. Ericsson, A.K. Pati, E. Sjöqvist, J. Brännlund and D.K.L. Oi, Phys. Rev. Lett. **91**, 090405 (2003).
- [Ericsson *et al.* 2003b] M. Ericsson, E. Sjöqvist, J. Brännlund, D. K. Oi and A. K. Pati, Phys. Rev. A. **67**, 020101(R) (2003).
- [Ericsson *et al.* 2005] M. Ericsson, D. Achilles, J.T. Barreiro, D. Branning, N.A. Peters and P.G. Kwiat, Phys. Rev. Lett. **94**, 050401 (2005).
- [Filipp *et al.* 2005] S. Filipp, Y. Hasegawa, R. Loidl and H. Rauch, Phys. Rev. A **72**, 021602(R) (2005).
- [Filipp *et al.* 2009] S. Filipp, J. Klepp, Y. Hasegawa, Ch. Plonka-Spehr, U. Schmidt, P. Geltenbort and H. Rauch, Phys. Rev. Lett. **102**, 030404 (2009).
- [Fu and Chen 2004a] Li-Bin Fu and Jing-Ling Chen, J. Phys. A: Math. Gen. **37**, 3699 (2004).
- [Fu and Chen 2004b] Li-Bin Fu and Jing-Ling Chen, J. Phys. A: Math. Gen. **37**, 7395 (2004).
- [Garrison and Wright 1988] J. C. Garrison and E. M. Wright, Phys. Lett. A **128**, 177 (1988).
- [Geppert and Both 2009] H. Geppert and M. Both, Project Thesis, Technical University of Vienna, Vienna, Austria (2009).

- [Hasegawa *et al.* 2001] Y. Hasegawa, R. Loidl, M. Baron, G. Badurek and H. Rauch, *Phys. Rev. Lett.* **87**, 070401 (2001).
- [Hasegawa *et al.* 2003] Y. Hasegawa, R. Loidl, G. Badurek, M. Baron and H. Rauch, *Nature (London)* **425**, 45 (2003).
- [Jones *et al.* 2000] J.A. Jones, V. Vedral, A. Ekert and G. Castagnoli, *Nature (London)* **403**, 869 (2000).
- [Joos *et al.* 2003] E. Joos, H.D. Zeh, C. Kiefer, D. Giulini, J. Kupsch and I.-O. Stamatescu, *Decoherence and the Appearance of a Classical World in Quantum Theory*, Springer-Verlag, Berlin Heidelberg New York (2003).
- [Klepp *et al.* 2005] J. Klepp, S. Sponar, Y. Hasegawa, E. Jericha and G. Badurek, *Phys. Lett. A* **342**, 48 (2005).
- [Klepp *et al.* 2008] J. Klepp, S. Sponar, S. Filipp, M. Lettner, G. Badurek and Y. Hasegawa, *Phys. Rev. Lett.* **101**, 150404 (2008).
- [Klepp 2004] J. Klepp, Diploma Thesis, Technical University of Vienna, Vienna, Austria (2004).
- [Kraan *et al.* 2003] W.H. Kraan, S.V. Grigoriev, M.Th. Rekveldt, H. Fredrikze, C.F. de Vroege and J. Plomp, *Nucl. Instr. and Meth. A* **510**, 334 (2003).
- [Kwiat *et al.* 1992] P. G. Kwiat, A. M. Steinberg and R. Y. Chiao, *Phys. Rev. A* **45**, 7729 (1992).
- [Larsson and Sjöqvist 2003] P. Larsson and E. Sjöqvist, *Phys. Lett. A* **315**, 12 (2003).
- [Leek *et al.* 2007] P.J. Leek, J.M. Fink, A. Blais, R. Bianchetti, M. Göppl, J.M. Gambetta, D.I. Schuster, L. Frunzio, R.J. Schoelkopf and A. Wallraff, *Science* **318**, 1889 (2007).
- [Lindblad 1976] G. Lindblad, *Comm. Math. Phys.* **48**, 119 (1976).
- [Lombardo and Villar 2006] F. C. Lombardo and P. I. Villar, *Phys. Rev. A* **74**, 042311 (2006).
- [Manini and Pistolesi 2000] N. Manini and F. Pistolesi, *Phys. Rev. Lett.* **85**, 3076 (2000).
- [Mezei 1988] F. Mezei, *Physica B* **151**, 74 (1988).

- [Nielsen and Chuang 2000] M.A. Nielsen and I.L. Chuang, *Quantum Computation and Quantum Information*, Cambridge University Press, Cambridge, England (2000).
- [Pancharatnam 1956] S. Pancharatnam, Proc. Indian Acad. Sci. A **44**, 247 (1956).
- [Peixoto de Faria *et al.* 2003] J. G. Peixoto de Faria, A. F. R. de Toledo Piza and M. C. Nemes, Europhys. Lett. **62**, 782 (2003).
- [Rauch and Werner 2000] H. Rauch and S.A. Werner, *Neutron Interferometry*, Clarendon Press, Oxford (2000).
- [Sakurai 1994] J.J. Sakurai, *Modern Quantum Mechanics*, Addison-Wesley, New York (1994).
- [Samuel and Bhandari 1988] J. Samuel and R. Bhandari, Phys. Rev. Lett. **60**, 2339 (1988).
- [Schmitzer 2009] C. Schmitzer, Diploma Thesis, Technical University of Vienna, Vienna, Austria (2009).
- [Scully and Drühl 1982] M. O. Scully and K. Drühl, Phys. Rev. A **25** 2208 (1982).
- [Shapere and Wilczek 1989] edited by Alfred Shapere and Frank Wilczek, *Geometric Phases in Physics*, Advanced Series in Mathematical Physics, Vol. 5, World Scientific (1989).
- [Singh *et al.* 2003] K. Singh, D.M. Tong, K. Basu, J.L. Chen and J.F. Du, Phys. Rev. A **67**, 032106 (2003).
- [Sjöqvist *et al.* 2000] E. Sjöqvist, A.K. Pati, A. Ekert, J.S. Anandan, M. Ericsson, D.K.L. Oi and V. Vedral, Phys. Rev. Lett. **85**, 2845 (2000).
- [Sjöqvist 2002] E. Sjöqvist, arxiv:quant-ph/0202078.
- [Sjöqvist 2004] E. Sjöqvist, J. Phys. A: Math. Gen. **37**, 7393 (2004).
- [Sponar *et al.* 2006] S. Sponar, J. Klepp, Y. Hasegawa, E. Jericha and G. Badurek, Acta Phys. Hung. A **26**, 165 (2006).
- [Sponar *et al.* 2008a] S. Sponar, J. Klepp, G. Badurek and Y. Hasegawa, Phys. Lett. A **372**, 3153 (2008).

- [Sponar *et al.* 2008b] S. Sponar, J. Klepp, R. Loidl, S. Filipp, G. Badurek, Y. Hasegawa and H. Rauch, *Phys. Rev. A* **78**, 061604(R) (2008).
- [Sponar 2009] S. Sponar, Ph. D. Thesis, Technical University of Vienna, Vienna, Austria (2009).
- [Stern *et al.* 1990] A. Stern, Y. Aharonov and Y. Imry, *Phys. Rev. A* **41**, 3436 (1990).
- [Suda 2006] M. Suda, *Quantum Interferometry in Phase Space. Theory and Applications*, Springer-Verlag, Berlin Heidelberg, Germany (2006).
- [Suter *et al.* 1988] D. Suter, K.T. Mueller and A. Pines, *Phys. Rev. Lett.* **60**, 1218 (1988).
- [Tomita and Chiao 1986] A. Tomita and R.Y. Chiao, *Phys. Rev. Lett.* **57**, 937 (1986).
- [Tong *et al.* 2004] D.M. Tong, E. Sjöqvist, L.C. Kwek and C.H. Oh, *Phys. Rev. Lett.* **93**, 080405 (2004).
- [Uhlmann 1991] A. Uhlmann, *Lett. Math. Phys.* **21**, 229 (1991).
- [Wagh and Rakhecha 1995a] A.G. Wagh and V.C. Rakhecha, *Phys. Lett. A* **197**, 107 (1995).
- [Wagh and Rakhecha 1995b] A.G. Wagh and V.C. Rakhecha, *Phys. Lett. A* **197**, 112 (1995).
- [Wagh *et al.* 1997] A.G. Wagh, V.C. Rakhecha, J. Summhammer, G. Badurek, H. Weinfurter, B. E. Allman, H. Kaiser, K. Hamacher, D. L. Jacobson and S. A. Werner, *Phys. Rev. Lett.* **78**, 755 (1997).
- [Wagh *et al.* 1998] A.G. Wagh, V.C. Rakhecha, P. Fischer, A. Ioffe, *Phys. Rev. Lett.* **81**, 10 (1998).
- [Whitney *et al.* 2005] R. S. Whitney, Y. Makhlin, A. Shnirman and Y. Gefen, *Phys. Rev. Lett.* **94**, 070407 (2005).
- [Yi *et al.* 2006] X. X. Yi, D. M. Tong, L. C. Wang, L. C. Kwek and C. H. Oh, *Phys. Rev. A* **73**, 052103 (2006).
- [Zeilinger and Shull 1979] A. Zeilinger and C.G. Shull, *Phys. Rev. B* **19**, 3957 (1979).

- [Zhu and Zanardi 2005] S.-L. Zhu and P. Zanardi, Phys. Rev. A **72**, 020301(R) (2005).
- [Zurek 2002] W.H. Zurek, *Decoherence and the Transition from Quantum to Classical - Revisited*, Los Alamos Science **27** (2002).